CHARACTERIZATION OF NANOSCALE OBJECTS AND DOMAINS WITH MASSIVE CLUSTER SIMS

A Dissertation

by

CHAO-KAI LIANG

Submitted to the Office of Graduate and Professional Studies of
Texas A&M University
in partial fulfillment of the requirements for the degree of

DOCTOR OF PHILOSOPHY

Chair of Committee,	Emile A. Schweikert
Committee Members,	David H. Russell
	Ronald D. Macfarlane
	Andreas Holzenburg
Head of Department,	David H. Russell

August 2014

Major Subject: Chemistry

ABSTRACT

Secondary ion mass spectrometry (SIMS) with a massive cluster projectile and run in the event-by-event bombardment/detection mode has been applied to perform nanoscale analysis. Massive clusters, specifically Au_{400}^{4+}, at hypervelocity feature efficient production of multiple secondary ions (SIs) desorbed from a nanometric volume per impact. The SIs from each projectile impact are collected and recorded as an individual event. Investigation of individual nano-objects with SIMS can thus be achieved by probing the objects one-at-a-time, avoiding issues due to ensemble averaging and neighboring effects.

Presented here are experiments where individual nano-objects of two categories were examined with 520 keV Au_{400}^{4+} in the event-by-event mode. Biological nano-objects, Qβ and M13 bacteriophages were dispersed by drop-casting onto a nanostructured substrate. By compiling the events containing an ion characteristic of the object, mass spectra specific to the phages can be extracted. A further refinement is the exclusion of the events containing a substrate-specific ion to minimize interference from the substrate. For metallic nano-objects, a series of gold nanoparticles (AuNPs) ranging from 2-50 nm was investigated. The AuNPs were dispersed and immobilized on silicon wafers. The results are the first experimental documentation of NP-size dependent SI yields. They can be significantly enhanced over those from bulk samples when projectile and NP characteristics are matched for efficient energy transfer. These observations

point out the necessity of accurate data interpretation when dealing with nano-scaled objects.

The capability of nano-domain analysis was demonstrated with fuel cell cathode materials consisting of pyrolized catalyst/carbon black mixtures. The coincidence methodology allowed to reveal variations in the chemical environment of the catalytically active sites at a nano-scale as a function of pyrolysis temperature. Additionally we could quantify the dispersion of the active sites on the carbon black, a measure providing a direction for future device optimization.

A new SIMS approach was developed for characterizing nanoparticles of $\leqq$10 nm. SIs emitted in the transmission direction from Au_{400}^{4+} impacts on nanoparticles were collected. The feasibility of the approach was tested with 5 nm dodecanethiol-capped AuNPs supported on free-standing graphene sheets. Our results reveal a new mode of energy partitioning, specific to 2D material, causing prolific sputtering and enhanced ionization. The AuNPs yielded analyte-specific peaks including from the dodecanethiol in comparison to emission in the conventional reflection mode. The coincidence methodology allowed also to determine the surface coverage of the 5 nm AuNPs.

TABLE OF CONTENTS

Page

ABSTRACT ii

TABLE OF CONTENTS iv

LIST OF FIGURES vi

LIST OF TABLES ix

CHAPTER

I INTRODUCTION 1

- Static SIMS 2
- Cluster Primary Ions 2
- Multiplicity and Coincidence Measurement in SIMS 5
- Current SIMS Analysis Results on Individual Nano-Objects 6
- Present Study 7

II INSTRUMENTATION AND METHODOLOGY 10

- Au Liquid Metal Ion Source SIMS 10
- C_{60} Effusion Source SIMS 16
- Wien Filter 16
- Detector 19
- Time-of-Flight Mass Analyzer 19
- Event-by-Event Bombardment/Detection Mode 22
- Coincidence Analysis 23
- Fractional Coverage and Effective Yield 27
- Sample Preparation 28

III CHARACTERIZATION OF BIOLOGICAL NANO-OBJECTS WITH NANOPROJECTILE-SIMS 29

- Introduction 29
- Experimental 30
- Results and Discussion 31
- Conclusion 39

CHAPTER Page

IV SIZE-DEPENDENT EMISSION OF NEGATIVE IONS FROM GOLD NANOPARTICLES BOMBARDED WITH C_{60} AND Au_{400} 40

Introduction 40
Experimental 41
Results and Discussion 42
Conclusion 57

V SIMS METHODOLOGY FOR PROBING THE FATE AND DISPERSION OF CATALYTICALLY ACTIVE MOLECULES 58

Introduction 58
Experimental 59
Results and Discussion 60
Conclusion 76

VI NEW SIMS APPROACH FOR SMALL NANOPARTICLE CHARACTERIZATION 77

Introduction 77
Experimental 79
Results and Discussion 85
Conclusion 114

VII CONCLUSIONS 115

Analysis of Individual Nano-Objects 115
Nano-Domain Analysis. 116
SIMS for Ultra Small Nanoparticle Characterization 116
Future Work 117

REFERENCES 120

LIST OF FIGURES

FIGURE		Page
II-1	Schematic overview of the custom Au-LMIS ToF-SIMS instrument.....	11
II-2	Schematic diagram of the custom C_{60} ToF-SIMS instrument.....	17
II-3	Total ion multiplicity distribution and molecular ion selected multiplicity distribution	24
II-4	Schematic illustration of coincidence mass spectrum	25
II-5	Schematic illustration of the double coincidence and coincidence/ anticoincidence methodologies applied in nano-object analysis	26
III-1	SEM Images of bacteriophages deposited onto the NALDI^{TM} plates	32
III-2	Negative ion mass spectrum of the Qβ phages on the NALDI^{TM} plate....	34
III-3	Negative ion mass spectrum of the M13 phages on the NALDI^{TM} plate .	35
III-4	Total, coincidence, coincidence/anticoincidence spectra of Qβ phage	36
III-5	Total, coincidence, coincidence/anticoincidence spectra of M13 phage..	38
IV-1	SEM images of AuNPs on PDDA-modified Si wafers	43
IV-2	Negative secondary ion mass spectra of 20 nm AuNPs on PDDA-modified Si wafer and PDDA-modified Si wafer impacted with 520 keV Au_{400}^{4+} projectiles.....	44
IV-3	Effective yields of Au_2^- and Au_3^- from AuNPs of different sizes and Au wafer impacted with 520 keV Au_{400}^{4+} projectiles.....	49
IV-4	Effective yields of Au_2^- and Au_3^- from AuNPs of different sizes and Au wafer impacted with 50 keV C_{60}^{2+} projectiles	53
IV-5	Sketch of 520 keV Au_{400}^{4+} impacts on “large” 50 nm NPs and “small” 2nm NPs.....	56

V-1 Negative SI mass spectra of pristine vitamin B12 and py-B12-700 impacted with 520 keV Au_{400}^{4+} projectiles 61

V-2 Structure of vitamin B12 and Co-corrole 64

V-3 Negative SI mass spectra of py-B12/C-500, py-B12/C-700 and py-B12/C-900 impacted with 520 keV Au_{400}^{4+} projectiles 65

V-4 Secondary ion yields of CN^-, $Au(CN)_2^-$ and cobalt-related ions for samples pyrolized at 500, 700, and 900°C 67

V-5 Schematic illustration of the proposed evolution of the active site's formation as a function of pyrolysis temperature 69

V-6 Coincidental mass spectra of co-emitted ions with $Co(CN)_2^-$ (m/z 111) for samples pyrolized at 500, 700, and 900°C 74

V-7 Coincidental mass spectra of co-emitted ions with PO_3^- (m/z 79) for samples pyrolized at 500, 700, and 900°C 75

VI-1 Schematic overview of the 2nd analysis chamber coupled to the custom Au-LMIS ToF-SIMS instrument 82

VI-2 Photograph of the experimental setup inside the 2nd analysis chamber 83

VI-3 Pictorial depiction of the synchronized electron start for registering simultaneously bi-directional ejecta 84

VI-4 SEM micrographs of 1L-graphene prior to Au_{400}-SIMS investigation 87

VI-5 SEM micrographs of 1L-graphene bombarded by 520 keV Au_{400}^{4+} impacts 88

VI-6 TEM micrographs of 1L-graphene bombarded by 520 keV Au_{400}^{4+} impacts 89

VI-7 TEM micrographs of the 1L-graphene bombarded by 520 keV Au_{400}^{4+} impacts 90

VI-8 Size distribution of Au_{400}^{4+} impact-resulting holes with TEM 92

VI-9 Transmission mass spectrum of 1L-graphene investigated with 520 keV Au_{400}-SIMS in negative ion mode 96

VI-10 Secondary ion yields of C_n^- obtained from the transmission mass spectra of graphene, carbon foil, and lacey carbon samples 97

VI-11 Secondary ion yields of C_nH^- and $C_nH_2^-$ obtained from the transmission mass spectra of graphene, and carbon foil samples 100

VI-12 Transmission mass spectra of 10 nm and 5 nm carbon foil investigated with 440 keV Au_{400}-SIMS in positive ion mode 101

VI-13 Transmission mass spectra of 1L-graphene investigated with 440 keV Au_{400}-SIMS in positive ion mode 102

VI-14 Secondary ion yields of C_n^+ obtained from the transmission mass spectra of the graphene samples 105

VI-15 Negative ion transmission mass spectra of 1L-graphene investigated by 130 qkeV Au-LIMS SIMS with Au_{400}^{4+}, Au_9^+, and Au_3^+ as the projectiles 106

VI-16 Secondary ion yields of C_n^- obtained from the transmission mass spectra of 1L-graphene examined with 520 keV Au_{400}^{4+}, 130 keV Au_9^+, and 130 keV Au_3^+ projectiles 107

VI-17 TEM micrographs of 5 nm dodecanethiol-coated AuNPs on 1-6L-graphene support 110

VI-18 Negative ion transmission mass spectra of 5 nm dodecanethiol-coated AuNPs on 1-6L-graphene and 1-6L graphene 111

VI-19 Negative ion reflection mass spectrum of 5 nm dodecanethiol-coated AuNPs on 1-6L-graphene 112

VI-20 Total and coincidence mass spectra of 5 nm dodecanethiol-coated AuNPs 113

LIST OF TABLES

TABLE		Page
IV-1	Effective yields of Au_4^- and Au_5^-	51
IV-2	Ratios, $Y_{eff,Au_n}(Au_{400})/Y_{eff,Au_n}(C_{60})$, for nanoparticle and bulk samples	51
IV-3	Effective yields of Au_2^-	51
V-1	Ratios of SI yield of PO_3^- to SI yield of PO_2^-	62
V-2	Calculated degree of dispersion of the active sites	62
VI-1	Extent of correlation in percentage between transmission and reflection electrons	95
VI-2	Fractional coverage of 5 nm dodecanethiol-coated AuNPs deposited on graphene	95

CHAPTER I

INTRODUCTION

The uniqueness of nano-objects due to functionalities not present in bulk-size is well documented.[1] A limiting step in the study of nano-objects is the lack of methods for molecular characterization at the nano-scale.[2,3] Typically, chemical vision with sub-μm spatial resolution relies on electron spectroscopies specifically for elemental analysis. Molecular information with the given spatial resolution can be achieved by secondary ion mass spectrometry, SIMS, but is restricted to the detection of small molecular fragments.[4,5] The motivation for this study is to advance molecular metrology into nano-domains with a novel mode of SIMS for nano-object analysis.

In principle, SIMS works by impacting target surface with energetic primary ions. Ejecta including electrons, photons, neutrals, and ions are emitted from the interrogated spots. The secondary ions are extracted and then mass-analyzed to reveal the compositional information on the surface.

The molecular characterization of nano-objects is based on an innovative concept of SIMS, where the nano-objects dispersed on a substrate are probed one by one. This approach avoids problems due to ensemble averaging, which can limit insight into the relationships between size, composition and chemical reactivity of nanoparticles (NPs).[6] This is especially the case for very small NPs where minor changes in size, shape, composition can significantly affect chemical reactivity.[7]

Before proceeding with a more detailed description of the objectives of the present works, the features of SIMS are summarized below with emphasis on the characteristics related to the goals of this study.

Static SIMS

Atomic projectiles are known for their creation of damage when impinging on organic/molecular surfaces in the form of molecular bond breaking and/or cross-linking.[8] In order to minimize the damage created, the primary ion dose is kept low such that the probability of a projectile hitting the same spot twice is minimal. That is, the low dose statistically guarantees that every projectile hits a virgin sample surface not damaged by a preceding impact. SIMS operating in the condition where the ion dose below 10^{12} ions/cm^2 is termed "Static SIMS" by Benninghoven et al.[9] However, limiting the primary ion dose in such a manner decreases the sensitivity of the method due to the inefficiency of atomic projectiles to produce significant secondary ion signals. A major innovation in improving the efficiency of secondary ion production is the utilization of cluster projectiles.

Cluster Primary Ions

The development and application of polyatomic ions as primary projectiles in SIMS have been pursued in recent years due to the nonlinear increase in secondary ion yield they produce.[10] The observation of "cluster effect" dates back as early as 1960, when the sputter yield by a diatomic or triaomic projectile on metallic surfaces was observed greater than the sum of that obtained from bombardment of equal-velocity individual

atomic constituent.[11,12] However, the benefits of cluster bombardment for SIMS application were not realized until the late 1980s.

The measure of the performance of a cluster projectile in producing secondary ions is the enhancement factor,[13] k_n, which is defined as

$$k_n = \frac{Y_{A_n}(E)}{nY_A(E/n)}$$

where $Y_{A_n}(E)$ is the yield of ions under cluster (A_n) projectile bombardment with kinetic energy of E, and $Y_A(E/n)$ is the yield of ions under atomic projectile (A) bombardment with kinetic energy of E/n. The cluster projectiles which enhancement factor greater than unity are deemed having nonlinear enhancement effect.

In 1989 Applhans et al. reported that enhancement factors of 10-25 in molecular ion yields were observed when SF_6^0 and SF_6^- projectiles were utilized to bombard organic surfaces as compared to isoenergetic Cs^+ projectiles of almost equal mass.[14] Concurrently in the same year, Blain et al. reported the first systematic study of the dependence of cluster effects on the nuclearity, involving the bombardment of a variety of surfaces with complex projectiles ($(CsI)_nCs^+$, n=1,2) of 5-28 keV. The authors found that the secondary ion yields increase in a supra-linear fashion with increasing nuclearity and are proportional to the square of the projectile momentum.[15]

The advent of liquid metal ion source (LMIS) and its implementation as a SIMS ion source enabled Benguerba et al. to extend the enhancement studies using gold cluster projectiles Au_n^{q+} (n=1-5, q=1,2) in 1991.[16] Again it was found that molecular ion yields from a phenylalanine target strongly increase with the increasing nuclearity. Following

experiments showed that the enhancement refrains from supra-linear to linear for projectiles with greater than ~9 constituents.[17]

In 1996 Van Stipdonk et al. reported the use of C_{60}^{+} as projectile, produced by passage of fission fragments from a ^{252}Cf source through a mylar foil covered by a layer of C_{60} film.[18] The study showed an approximately 20-fold enhanced molecular ion yield from a phenylalanine target as compared to isoenergetic Cs^{+} projectiles. The C_{60} ion source was not adapted in routine application in SIMS until the development and commercialization of the C_{60} effusion source by the Vickerman group in 2003.[19,20] The ionized C_{60}^{q+} (q=1,2) is created by electron impact ionization of gaseous C_{60} via sublimation of buckminsterfullerene powder. In addition to regular surface analysis, C_{60} source is successful at molecular depth profiling by providing steady state molecular ion signals since the damage created during a single ion impact is largely removed by subsequent impacts.[21,22,23] By integrating the capability of depth profiling with a raster C_{60} beam, Fletcher et al. in 2007 showed the first example of three-dimensional (3D) analysis on a biological single cell system.[24]

The application of massive Au_{400}^{4+} clusters as a SIMS ion source was introduced by Tempez et al. in 2004, where they found a ~1000 enhancement in molecular ion yield for Gramicidin S as compared to Au^{+} projectile of the same energy per charge (E/q) and remarkably low damage cross-section associated with the Au_{400}^{4+} impacts.[25] The Au-LMIS utilized can generate a suite of gold cluster projectiles ranging from Au_1^{+} to Au_{120q}^{q+} (q=1-9). The most intense massive projectile has an n/q ~100 with a most probable charge state of 4.[26] The same source has been actively utilized in the

Schweikert group at Texas A&M University and installed on a Pegase high voltage platform, permitting to accelerate the gold cluster projectiles with impact energies of up to 120 qkeV.[27] DeBord et al. showed that the Au_{400}^{4+} projectile impacts in the hypervelocity regime (~35 km/s) feature high signal enhancement in deprotonated molecular ions and also multiplicity, i.e. the number of ions created per projectile impact, from a series of peptide targets.[28] Additionally, an in-depth study was conducted by the same authors regarding the investigation of the internal energies of species emitted from the hypervelocity Au_{400}^{4+} impacts. The results suggest that Au_{400}^{4+} SIMS is suited for the analysis of labile molecules due to the low average internal energy per atom observed from the ejected molecular ions, which is comparable to that obtained with "soft" ionization techniques.[29]

Multiplicity and Coincidence Measurement in SIMS

Emission of multiple secondary ions as a result of a single projectile bombardment is desirable in that more analytically significant signals can be obtained from a given probing event. The number of emitted ions per impact event, the so-called multiplicity, can be determined by separating the impacts in time and counting all the emitted ions associated with each impact using time-of-flight (ToF) mass spectrometers. The term "event-by-event bombardment/detection mode" is used in this dissertation to refer to this particular data acquisition condition. Rickman et al.[30] and DeBord et al.[28] both showed that the massive cluster Au_{400}^{4+} projectile is more efficient in multiple ion emission from organic surfaces in the energy regimes of 134.6 and 520 keV as compared to small Au clusters such as 28.6 keV Au_9^+ and 130 keV Au_3^+ respectively. The average number of

detected ions per projectile impact is ~10 for Au_{400}^{4+} whereas ~1 for small clusters in the given energy regimes. Della-Negra et al. even reported the feasibility of generating a mass spectrum using one single Au_{100q}^{q+} impact of 200 qkeV on a biomolecule surface.[27]

In the event-by-event bombardment/detection mode, the projectile impacts are resolved not only in time but also in space. The nature of the co-emitted ions represents the chemical composition of species co-located within a nano-domain of ~10^3 nm^3 at the given probed site. The Schweikert group has utilized the coincidence concept in examining compositional homogeneity of mixed surfaces.[31,32,33] In addition to secondary ions, electrons and photons emitted in coincidence with one another as a result of cluster impacts can also be investigated.[34,35] As such, Eller et al. have developed an innovative methodology to map chemical distribution of species by correlating signature secondary ions with simultaneously emitted electrons which were collected by an electron emission microscope (EEM).[36,37]

Current SIMS Analysis Results on Individual Nano-Objects

Based on studies accomplished in the Schweikert group, size-dependent SI emission was observed when several aluminum oxide-based objects of different dimensions were investigated with Au_{400}^{4+} impacts operated in the event-by-event bombardment/detection mode.[38] A shift of SI mass distribution toward low-mass region was observed when the size of the object (nanowhiskers, ~2 nm in diameter, ~200 nm in length) is below the size of the desorption volume of the projectile (~10^3 nm^3). The effect of object size on electron emission was also reported in a comparison to a bulk size aluminum oxide sample.[39] The probability of electron emission decreases for

smaller objects. Both observations point out the necessity of accurate data interpretation when dealing with nano-scaled objects.

In addition to SI and electron emission, the effect of object size on sputtering has been studied by molecular dynamics simulations. Zimmermann *et al.* reported that a 16 keV Au projectile impacting on a 20 nm gold nanoparticle (AuNP) leads to a higher sputtering yield compared to a planar surface by a factor of 2.5.[40] Simulations by Järvi *et al.* have shown size-dependent sputtering yields from AuNPs of 1-15 nm with 25 keV Ga projectiles.[41] The result indicates the yield from 8 nm AuNPs is enhanced roughly three-fold as compared to bulk. Recently, Gilmore *et al*. presented the experimental study on the sputtering of dispersed AuNPs using a C_{60}^{2+} beam.[42] An increase in sputtering yields for nanoparticles was measured as compared with bulk, again in agreement with predictions from simulation.

From a perspective of application, SIMS operating in the event-by-event mode enables one to extract mass spectra specific to dispersed nano-objects of interest from a binary mixture of nano-objects (polystyrene nanoparticles and alumina nanowhiskers)[43] and to quantify the density of 5 nm AuNPs dispersed on cell membranes[44]. For nano-objects with volumes larger than the projectile's sampling volume, the degree of coating of modifiers on the surface of the nano-objects can be evaluated.[45]

Present Study

In this dissertation, three main topics are investigated and discussed: 1) the application of massive cluster SIMS operating in the event-by-event bombardment/detection mode for investigation of individual nano-objects, 2) the

molecular characterization of cathode materials used for fuel cell with ToF-SIMS, and 3) the development of dual ToF-SIMS instrument and its application in examination of objects <10 nm.

The first topic was investigated using free-standing nano-objects. The goals of the studies were two-fold: a) to extract molecular information specific to the biological nano-objects without interference from their substrates; b) to understand how the emission of SIs relates to the size of nano-objects and their relationship to bulk materials of the same composition. M13 and Qβ bacteriophages were chosen as the model of the biological nano-objects and drop-casted onto NALDI^{TM} plates for the SIMS analyses with Au_{400}^{4+}. AuNPs of a series of sizes (2-50 nm) dispersed on silicon wafers and a bulk Au wafer were investigated using Au_{400}^{4+} and C_{60}^{2+}.

The second topic was performed with the Au_{400}^{4+} ToF-SIMS analyses on samples prepared in a collaborative endeavor by the Chen group at Academia Sinica, Taiwan, which are pyrolized mixtures comprising vitamin B12 and carbon black as a cathode material for fuel cell. The goal was to understand the effect of temperature on the chemical environment in a nano-scale of the catalytically active sites formed on the carbon supports during pyrolysis.

The third topic was conducted by assembling an analysis chamber comprising two ToF mass spectrometers at the two sides aligned with the normal of the target surface. The goal of the studies was to provide a platform for small object analysis with object-relevant information collected as much as possible and minimized interference from substrate. Studies were carried out using free-standing graphene sheets of few layers and

5 nm dodecanethiol-capped AuNPs loaded on the graphene substrate. Samples were investigated in the event-by-event bombardment/detection mode with Au_{400}^{4+}. SIs emitted simultaneously from both sides were collected and analyzed.

CHAPTER II

INSTRUMENTATION AND METHODOLOGY

This chapter describes the two custom-built time-of-flight (ToF) secondary ion mass spectrometers which were utilized in this dissertation. Also, the methodologies derived from the event-by-event bombardment/detection mode to extract mass spectra specific to nano-objects of interest and to study effective yields are outlined in detail below.

Au Liquid Metal Ion Source SIMS

The experimental results discussed in Chapters III, IV, and V were obtained using the Au Liquid Metal Ion Source (Au-LMIS) SIMS. A detailed description of the instrument is available elsewhere.[46]

A schematic of the instrument is presented in Figure II-1. The source is installed on the Pegase high voltage platform, which was designed and built by collaborators at the Institute for Nuclear Physics in Orsay (IPNO), France.[27] The platform allows one to float the primary ion chamber up to 100 kV. The source is composed of a reservoir of tightly wound coils and a needle placed in the middle of the reservoir. Both the reservoir and needle are made from tungsten wires (Ø 200 μm, Alfa Aesar). The reservoir is filled with Au/Si eutectic (97 % Au, 3 % Si, Academy Precision Metals) by dipping into the melted eutectic. The source operates in the primary ion chamber, which is maintained at $<1x10^{-6}$ torr with a 400 L/s turbo pump (Adixen ATP400, Alcatel Vacuum Technology) and backed by a dry roots pump (Adixen ACP28, Alcatel Vacuum Technology). The

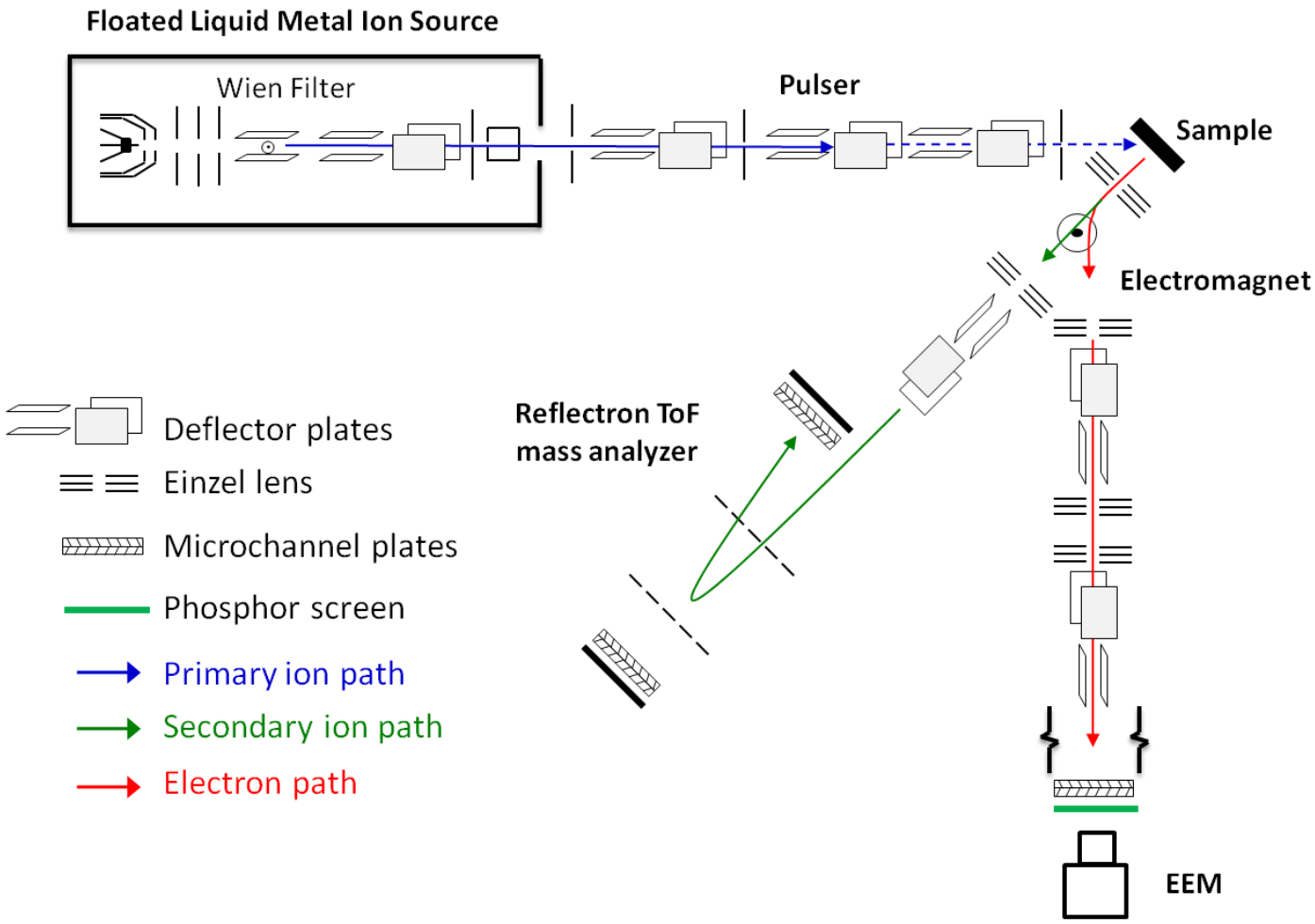

Figure II–1. Schematic overview of the custom Au-LMIS ToF-SIMS instrument.

source is initiated by passing current through the reservoir to heat the eutectic to melt (363˚C). An extraction potential (6-10 kV relative to the source) is applied on the extraction electrode in front of the tip of the needle with a distance of ~0.5 mm. The potential facilitates the formation of a Taylor cone, creating gas phase droplets from the metallic liquid.[47] The source is floated to 20 kV relative to the platform, providing the projectiles with a total kinetic energy of 120 qkeV at the exit of the platform.

The source creates a wide range of projectiles from Au_1^+ to Au_{120q}^{q+} (q=1-9). The formation of massive gold clusters is favored by increasing the current limitation applied to the extraction power supply. For example, the distribution of the massive clusters centers at m/q 8,000 for an extraction current of 20 μA, whereas for 50 μA, m/q 20,000 which corresponds to the Au_{100q}^{q+} projectiles. The massive clusters emitted under this condition have been found to contain an average of 400 gold atoms and a charge state of +4.[26] The Au beam is focused with a high voltage Einzel lens (~14 kV) and then introduced to a Wien filter after emission through an aperture (Ø 1.5 mm) on the extraction electrode. The Wien filter is used to mass select the desired projectiles of a given mass-to-charge ratio (m/q).

After mass filtering, the beam of the selected projectile enters a set of vertical and horizontal electrostatic deflectors and then a collimator comprising apertures of four different diameters (3 mm, 1 mm, 500 μm, and 200μm). Collimation reduces the fluence and beam diameter. The 500 μm aperture was used for all the experiments performed in this dissertation. The beam intensity is monitored using a removable Faraday cup behind

the collimator. As a reference, the Au_{400}^{4+} beam is typically 190-200 or 550-600 pA when the extraction current limit is set at 20 or 50 μA respectively.

An insulating vacuum break is set in the beamline and used to maintain the potential drop between the high voltage platform and the grounded analysis chamber. A trumpet-shaped lens is mounted within the vacuum break, allowing the beam to accelerate to high energy (up to 120 qkeV). This region is pumped by a 220 L/s turbo pump (Edwards EXT 225H) to a pressure of ~$1x10^{-6}$ torr. The beam exiting the platform is then directed to the target surface in the analysis chamber with three sets of deflectors in series. A collimator having two slits (0.5 mm and 1 mm in width) is located between the first and the second deflector set to eliminate stray projectile trajectories. The second deflector set also functions as a pulsation system to reduce the beam flux. Time-varying high voltage logic pulses are applied to the plate of the vertical deflection below the beam line using a high voltage switch (Behlke HTS 151-03-GSM) which is driven by a pulse generator (HP 8005B). The pulsing voltage is varied from +1 kV to -1 kV at a repetition rate of 3 kHz. Prior to bombarding the target surface, projectiles enter an aperture of a given size (Ø 250 μm, 500 μm, and 5 mm) on another collimator, which confines the size of the probing area. The 500 μm aperture was used for all the experiments performed in the first analysis chamber. The collimation and the pulsation system together reduce the beam current down to a sequence of individual projectiles at an impacting rate of ~1,000 Hz, as a prerequisite for the event-by-event bombardment/detection mode.

The projectiles impact a -10 kV biased target at an incident angle of 45˚ in the first analysis chamber, hence carrying a total energy of 130 qkeV. The resulting secondary ions and electrons are accelerated from the target surface with a kinetic energy of 10 keV and focused by an Einzel-styled extraction lens to a point within a magnetic prism. A weak magnetic field (~30 Gauss) is applied to deflect the electrons, but too weak to perturb the trajectories of the secondary ions. The detoured electrons are directed by a series of lenses and deflectors and detected by an electron emission microscope (EEM). The EEM consists of two microchannel plates (MCPs, Photonics) in chevron assembly followed by an aluminized P43 phosphor screen. The phosphor screen enables visualization of electron impacts on the detector. For the experiments performed in this dissertation, the EEM was utilized to register the ejected electrons where the lens and deflectors were adjusted to optimize the detection of electrons. The electron signal is used to initiate the ToF measurements. Although the electron mapping capability of the EEM was not utilized, its working principle and the associated electronics setup are detailed in refs [36,37,48].

The secondary ions unperturbed by the magnetic field are further focused by another Einzel lens into a custom-built dual stage reflectron mass spectrometer.[49] After entering the reflectron, the ions are reflected by the ion mirror at an angle (~2.8˚) above their entrance trajectory and then detected by a SI detector, which is mounted above the flight tube axis. The SI detector consists of a pair of MCPs in chevron assembly and a pie-shaped eight-anode detector, allowing one to detect up to 8 isobaric ions per projectile impact. A set of deflectors is installed prior to the entrance of the reflectron in

order to optimize the detection efficiency by distributing the ions detected evenly among the eight anodes.

The signal of a charged particle arriving at the detector is amplified via the two MCPs to a gain of ~10^6 electrons, causing a negative voltage spike on the anode. The transient spike signals received on the eight anodes are then transmitted to an eight-port constant fraction discriminator (CFD, Ortec CF8000). The CFD has two functions: a) to eliminate ringing signals by setting a threshold for the input pulse amplitude, and b) to convert the input signal to a NIM (Nuclear Instrumentation Module) logic pulse as a stop signal for ToF measurements. Similarly, for the start detector (EEM), the voltage spikes received at the aluminum layer coated on the phosphor screen are processed with a quad CFD (Canberra QUAD454). The start and stop signals are transferred to a time-to-digit converter (TDC, Orsay Physics CTNM4). The TDC possesses a single port for the input of a start signal and an octo-port for the inputs of eight stop signals. Upon receiving the start signal, the stop signals are time-registered as digital signals relative to the start signal with a time resolution of 400 ps. The digital signals from each projectile impact are recorded as a single event and stored on personal computer with accumulation of several million events collected during data acquisition in a Total Matrix of Events (TME) format.[50,51] The TME files can be processed by a custom-written analysis software, SAMPI (Surface Analysis and Mapping of Projectile Impacts).[48]

Instrumentation associated with the second analysis chamber and the operation in positive mode are discussed in Chapter VI.

C_{60} Effusion Source SIMS

A portion of the experimental results described in Chapters IV were obtained using a custom-built C_{60} effusion source SIMS coupled with a linear ToF mass analyzer. The schematic is presented in Figure II-2.

The C_{60} primary ions are generated by heating buckminsterfullerene powder (Sigma Aldrich) housed in a copper reservoir to sublimation (~450˚C). The gaseous C_{60} effuses out of the reservoir through an orifice to an ionization region where the C_{60} is ionized by electron impact to C_{60}^{q+} (q=1-3) using 150 eV electrons emitted from a tantalum electrode disc. The ionized species are accelerated toward an extraction plate up to 15 qkeV and focused by an Einzel lens. The beam is then directed to a Wien filter using a set of deflectors such that the ionized C_{60} of a given charge state is selected. C_{60}^{2+} was used to perform the experiments addressed in this dissertation. After mass selection, the beam is further directed and focused to a -10 kV biased target surface in the analysis chamber with an incident angle of 45˚, carrying a total kinetic energy of 25 qkeV. The currents respectively applied to heat the copper reservoir and to generate the electron emission via the Ta electrode are adjusted so that the flux of projectiles falls within the regime of <1,000 impacts per second without the need of pulsation system, meeting the prerequisite of the event-by-event bombardment/detection mode. The detection of secondary ions and electrons is similar as described in previous session.

Wien Filter

The Wien filter is technically a velocity filter, consisting of a permanent magnet which magnetic field is perpendicular to a variable electric field generated by a pair of

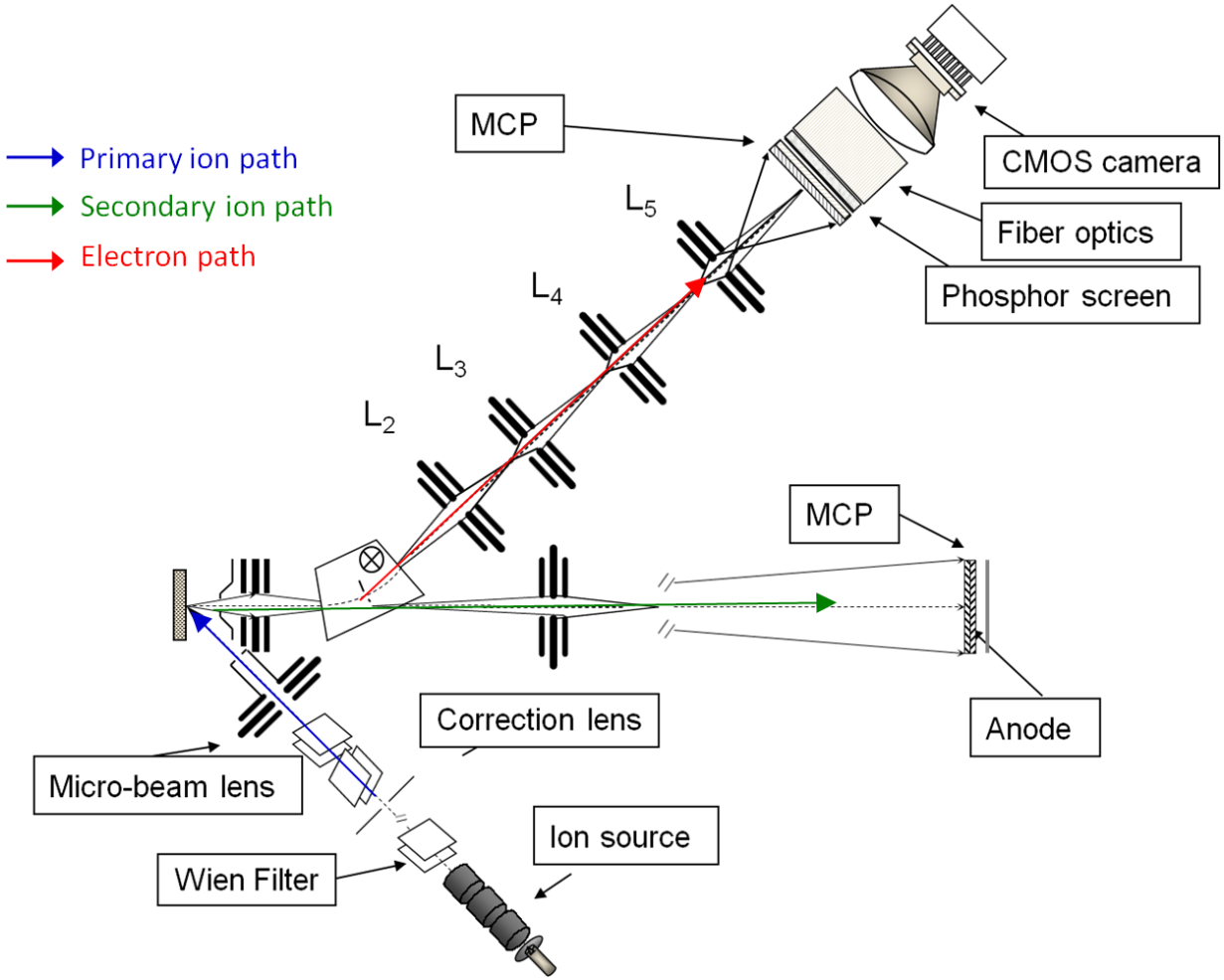

Figure II–2. Schematic diagram of the custom C_{60} ToF-SIMS instrument.

electrodes. The trajectory of a charged particle proceeding within the Wien filter is affected by the net effect of the Coulomb and Lorentz forces:

$$F_{net} = F_{Coulomb} + F_{Lorentz} = (qE) + (qv \times B) \text{ Eq. II-1}$$

where E and B are the electric and magnetic field (Telsa) strengths respectively and v is the velocity (m/s) of the charged particle. By varying the electric field, a charged particle of a given velocity will experience zero net force and thus have a linear trajectory through the filter.

$$qE = qvB \text{ Eq. II-2}$$

$$v = \frac{E}{B} = \frac{V/d}{B} = \frac{V}{dB} \text{ Eq.II-3}$$

where V is the potential (volt) applied to the electrodes and d (meter) is the distance between the electrodes.

The velocity of a charged particle for a given mass (m, kg) is determined by its kinetic energy (E_K, joule) with the relationship below:

$$v = \sqrt{\frac{2E_K}{m}} \text{ Eq. II-4}$$

Therefore, the projectile of a certain mass can be selected out by adjusting the potential to the proper value based on the following equation by substituting Eq II-3 for the velocity:

$$V = Bd\sqrt{\frac{2E_K}{m}} \text{ Eq. II-5}$$

Detector

Although the MCPs in both start and stop detectors are assembled in the chevron configuration, the voltage applied is different for each case. For the start detector used in the Au-LIMS SIMS, a positive potential of ~1.6 kV is applied onto the backside of the second plate of the MCP assembly whereas the front side of the first plate is grounded, creating a potential gradient to guide the electrons generated in the amplification cascade to the back. The electron spike is then received by the aluminum film coated on the phosphor screen, which is biased at ~+3.5 kV. For the stop detector, a negative potential of ~2.4 kV is applied on the front site of the first MCP whereas the anodes are grounded. A decreasing negative potential through the MCPs is thus established by a network of resistors to guide the cascade electrons. The negative bias on the front site of the first MCP, however, can decelerate the secondary ions when operating in negative ion mode. Therefore, the effect of the deceleration must be considered when dealing with the calculation of the flight time of secondary ions. For the C_{60}-SIMS, ~+2.0, ~+2.6, and ~-2.3 kV were applied onto the MCPs, phosphor screen of the start detector and the MCPs of the stop detector respectively.

Time-of-Flight Mass Analyzer

The flight time a secondary ion spends from the target surface to the detector is characteristic of its mass-to-charge ratio (m/z). For the linear ToF mass analyzer used in the C_{60}-SIMS, the total flight time for a give ion is a summation of the times spent in the acceleration, field-free drift, and deceleration regions as illustrated in Eq. II-6. The acceleration region is where the emitted ions are accelerated to the extraction lens. The

field-free drift region is of zero electric potential gradient, defined by the grounded front electrode of the extraction lens and a grounded nickel grid (90% transmission, Precision E-forming) placed in front of the MCP detector. The deceleration region is where the ions experience retarded after passing the grid by the negatively potential applied on the front side of the MCP assembly.

$$t_{total} = t_{ac} + t_{dr} + t_{de} \quad \text{Eq. II-6}$$

The time spent in each region is given below which derivation has been detailed elsewhere.[52]

$$t_{ac} = \sqrt{\frac{2md_{ac}^2}{qV_{ac}}} \quad \text{Eq. II-7}$$

$$t_{dr} = \sqrt{\frac{md_{dr}^2}{2qV_{ac}}} \quad \text{Eq. II-8}$$

$$t_{de} = \frac{\sqrt{2md_{de}^2} \cdot (-\sqrt{V_{ac}} \pm \sqrt{V_{ac} + V_{de}})}{\sqrt{q} \cdot V_{de}} \quad \text{Eq. II-9}$$

Therefore,

$$t_{total} = \sqrt{\frac{2md_{ac}^2}{qV_{ac}}} + \sqrt{\frac{md_{dr}^2}{2qV_{ac}}} + \frac{\sqrt{2md_{de}^2} \cdot (-\sqrt{V_{ac}} \pm \sqrt{V_{ac} + V_{de}})}{\sqrt{q} \cdot V_{de}} \quad \text{Eq. II-10}$$

where t_{ac}, t_{dr} and t_{de} are the times spent in the acceleration, field free drift, and deceleration regions respectively; m and q are the mass and charge state of the secondary ion; V_a is the voltage applied on the target; V_d is the voltage applied on the front side of the MCP assembly; d_{ac}, d_{dr} and d_{de} are the lengths of the acceleration, field-free drift, and deceleration regions respectively.

For a reflectron ToF arrangement, in addition to the acceleration, two field free drift, and deceleration regions, the time spent in the ion mirror region must be taken into consideration. The ion mirror comprises a stack of electrodes connected in series by resistors. A potential (V_{ref}) higher than the acceleration potential (V_{ac}) is applied onto the last electrode, creating an electric field where an ion is retarded and then reflects. The time spent in this region depends on the depth to which the ion penetrates (d_{ref}). This depth is derived as follows:

$$qV_{ac} = q\frac{V_{ref}}{L}\cdot d_{ref} \quad \text{Eq. II-11}$$

$$d_{ref} = \frac{V_{ac}L}{V_{ref}} \quad \text{Eq. II-12}$$

where L is the length of the reflectron. The time required to reach this depth is:

$$t_{ref/2} = \frac{d_{ref}}{v/2} \quad \text{Eq. II-13}$$

where v is the velocity of the ion at the exit of the acceleration region. The total time spent in the reflectron is:

$$t_{ref} = 2\cdot t_{ref/2} = \frac{4d_{ref}}{v} = \frac{4d_{ref}}{\sqrt{\frac{2qV_{ac}}{m}}} = \sqrt{\frac{8md_{ref}^2}{qV_{ac}}} \quad \text{Eq. II-14}$$

Therefore, the total time the ion requires to travel from its creation to detection in a reflectron ToF mass spectrometer is:

$$t_{total} = t_{ac} + t_{dr1} + t_{ref} + t_{dr2} + t_{de}$$

$$= \sqrt{\frac{2md_{ac}^2}{qV_{ac}}} + \sqrt{\frac{md_{dr1}^2}{2qV_{ac}}} + \sqrt{\frac{8md_{ref}^2}{qV_{ac}}} + \sqrt{\frac{md_{dr2}^2}{2qV_{ac}}} + \frac{\sqrt{2md_{de}^2}\cdot(-\sqrt{V_{ac}} \pm \sqrt{V_{ac}+V_{de}})}{\sqrt{q}\cdot V_{de}} \quad \text{Eq. II-15}$$

where t_{dr1} and t_{dr2} are the times spent in the field free drift regions before and after the reflectron respectively with their associated lengths d_{dr1} and d_{dr2}.

Equations II-10 and II-15 show the flight time of a give ion is proportional to the square root of its mass for both linear and reflectron ToF mass analyzers. The mass of any peak in a time-of-flight spectrum can be determined using a mass calibration to convert the ToF spectrum to a mass spectrum. The calibration is achieved by fitting Equation II-16 to two or more known ToF/mass data points,

$$t_{total} = a\sqrt{m} + b \quad \text{Eq. II-16}$$

where a is the slope and b is the intercept of the fitting trendline.

Event-by-Event Bombardment/Detection Mode

As noted above, the primary beam is reduced to a sequence of individual projectiles which are ~1 ms apart. The SIMS investigation under the condition where the projectiles are sent one-by-one to probe the target surface permits studies in the "super static regime" (dose $\leqq 10^6$ projectiles/cm^2).[53] This unique SIMS approach is termed "event-by-event bombardment/detection mode". The super static regime ensures the projectiles bombard the target surface in a stochastic manner without sampling the same spot twice. Therefore, the molecular information is retained on the surface before probed. The secondary ions resulting from each projectile impact are stored as a single event. A conventional mass spectrum can be obtained by summing cumulative events of few millions. A measure concerning the projectile's efficiency in producing an ion of interest from a given target is the secondary ion yield (Y), which can be derived as follows:

$$Y_A = \sum_{x_A} \frac{x_A N(x_A)}{N_{total}} = \sum_{x_A} x_A P(x_A) = \frac{I_A}{N_{total}} \quad \text{Eq. II-17}$$

where x_A is the number of detected ions A in a single event ($0 \leqq x_A \leqq 8$), $N(x_A)$ is the number of events when x_A ions of A are detected, N_{total} is the total number of events collected, $P(x_A)$ is the probability distribution of detected ions A per single projectile impact, I_A is the number of the detected ion A in the conventional mass spectrum.

For cluster projectiles which can produce multiple ions per projectile impact, the event-by-event bombardment/detection mode allows one to measure the number of ions emitted per impact, i.e. multiplicity. With the SAMPI software, one can extract not only the total number of ions emitted from an impact (total ion multiplicity), but also the number of a selected type of ion emitted per event (ion selected multiplicity) (Figure II-3).

Coincidence Analysis

In addition to conventional mass spectrum, one can also construct a spectrum by compiling a subset of alike events, e.g. events which contain a selected ion of interest, referred to as coincidence mass spectrum (Figure II-4). The coincidence mass spectrum is a display of all ions which are co-emitted with the selected ion from the same desorption volume. The desorption volume for massive clusters, e.g. Au_{400} and C_{60}, is a nanometric crater of ~10^3 nm^3.[54,55] This is also the basis of the studies discussed in this dissertation for the SIMS investigation in nano-domain. Thus, one can determine species co-localized with a given analyte within a nanovolume by identifying the ions co-emitted with an ion characteristic of the anlayte. The coincidence analysis can be

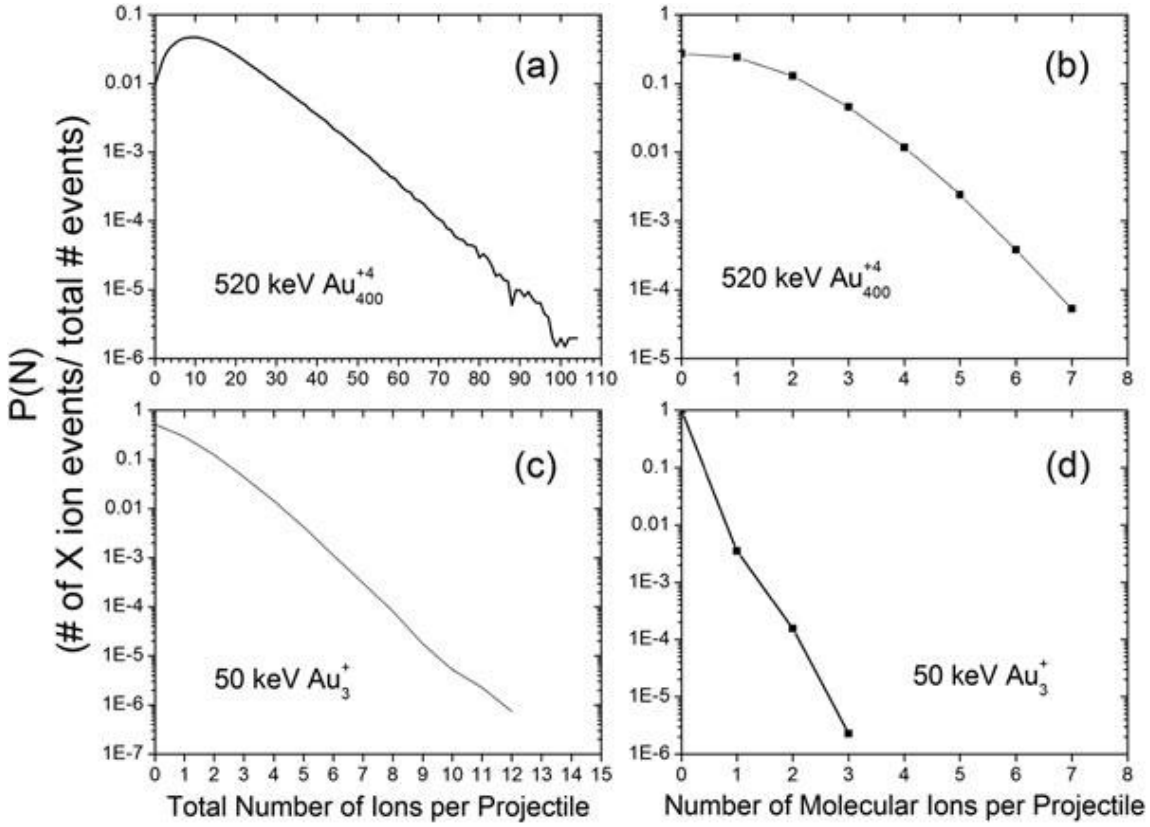

Figure II–3. Total ion multiplicity distribution and molecular ion selected multiplicity distribution. (a) (b) 520 keV Au_{400}^{4+} and (c) (d) 50 keV Au_3^+ projectile impacts on leu-enkephalin surface. Results are obtained in negative mode. (The figure is reprinted with permission from Ref [28] "Characteristics of positive and negative secondary ions emitted from Au_3^+ and Au_{400}^{+4} impacts" by DeBord, J.D., Fernandez-Lima, F.A., Verkhoturov, S.V., Schweikert, E.A., Della-Negra, S. *Surf. Interface Anal.* **2013**. Copyright 2012 John Wiley and Sons).

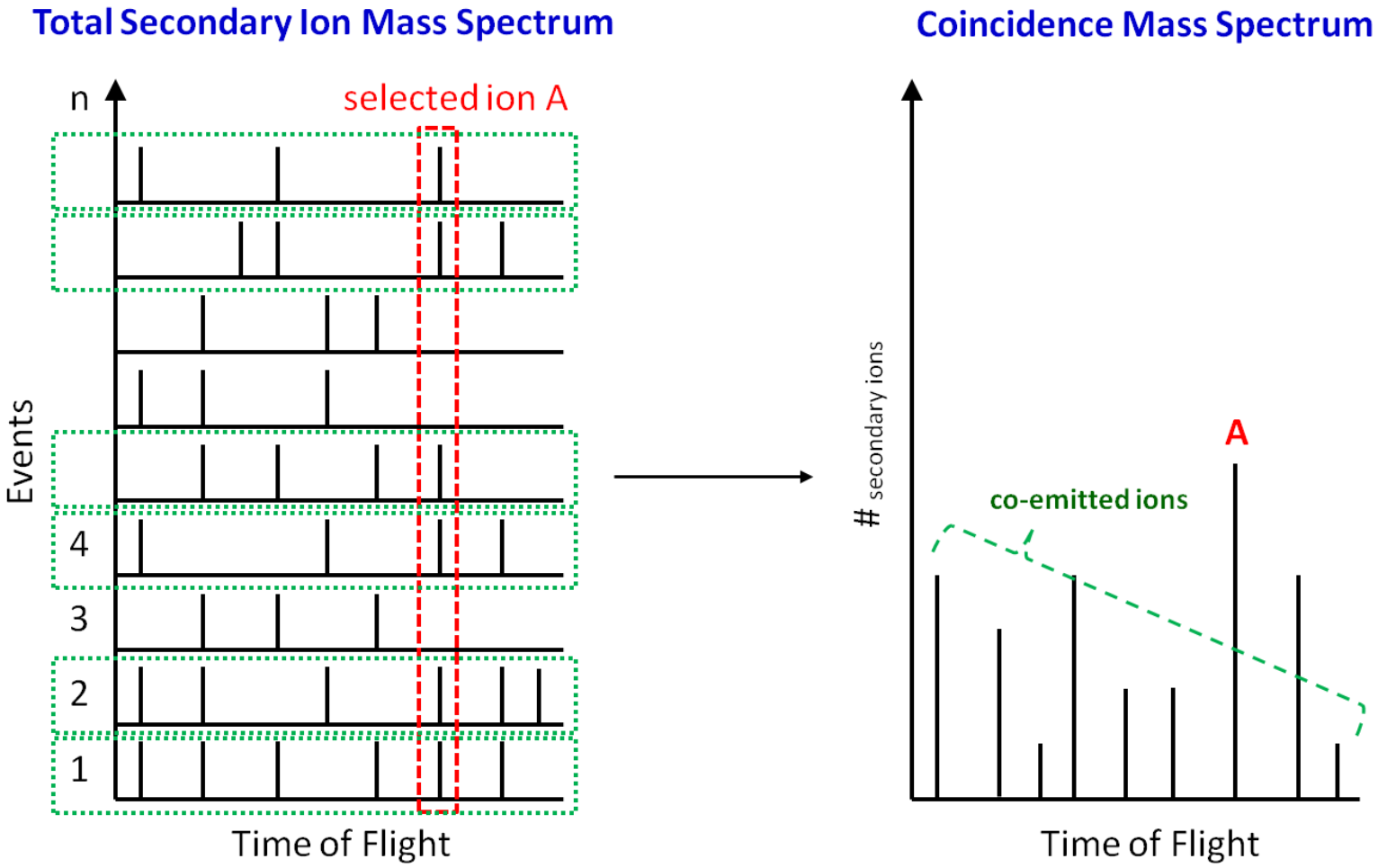

Figure II–4. Schematic illustration of coincidence mass spectrum.

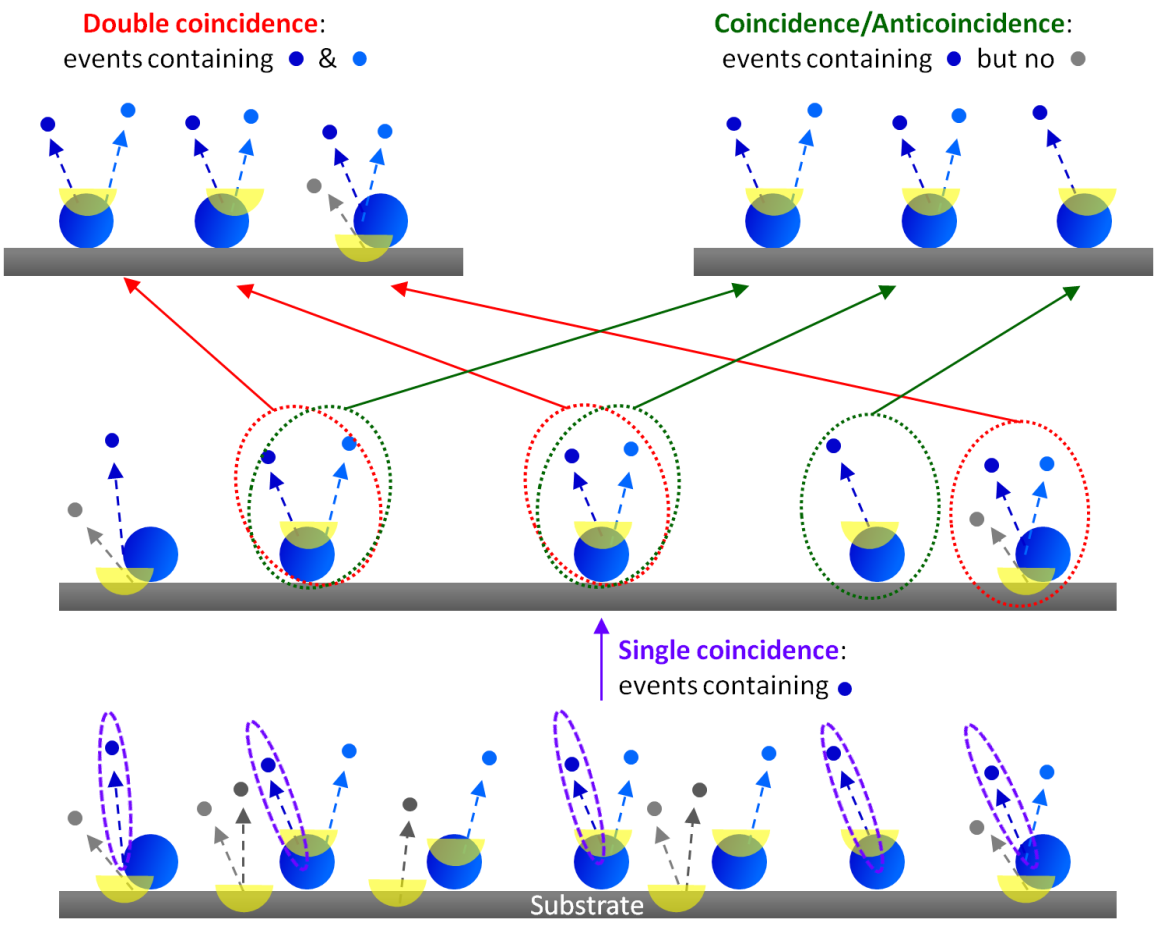

Figure II–5. Schematic illustration of the double coincidence and coincidence/anticoincidence methodologies applied in nano-object analysis.

further applied in two versatile ways as illustrated in Figure II-5. One is investigation of double coincidence mass spectrum, where the spectrum is composed of events containing two selected ions of interest. This selection can enhance the accuracy of identifying co-localized species from a complex surface, e.g. avidin-biotin assembly on modified glass substrates.[33] Another is investigation of coincidence/anticoincidence mass spectrum, where the spectrum is composed of events containing an ion characteristic of analyte but without an ion characteristic of substrate. The concept of coincidence/anticoincidence mass spectrum is applied in this dissertation (Chapter III) to obtain spectra specific to the nano-objects without the interference from the supporting substrates.

Fractional Coverage and Effective Yield

SIMS operating in the event-by-event bombardment/detection mode not only provides compositional information on the target surface, a methodology derived from this approach also allows one to quantify the fractional coverage of analyte distributed within the probing area. The quantification of fractional coverage of analyte on the sample surface lies in the knowledge of the number of impacts actually bombarding the analyte, or number of effective impacts (N_e), during the investigation. Therefore, the ratio of the number of effective impacts to the number of total impacts reveals the fractional coverage of the analyte within the probing area.

The calculation of the number of effective impacts necessitates two ions, e.g. A and B, characteristic of the analyte given that the two ions are co-emitted independently whenever the analyte is impacted. This relationship can be expressed by[56]:

$$Y_{A,B} = Y_A \cdot Y_B \quad \text{Eq. II-18}$$

where $Y_{A,B}$ is the coincidental SI yield of simultaneously detected ions A and B. Y_A and Y_B are the secondary ion yields of detected ions A and B respectively.

Eq. II-18 can be rewritten as follows:

$$\frac{I_{A,B}}{N_{eff}} = \frac{I_A}{N_{eff}} \cdot \frac{I_B}{N_{eff}} \quad \text{Eq. II-19}$$

where $I_{A,B}$ is the detected number of co-emitted A and B in the coincidence mass spectrum, I_A is the number of A in the conventional mass spectrum while I_B is the number of B. N_{eff} is the number of effective impacts for emissions of A and B.

The fractional coverage (K) of the specimen can thus be obtained by rearranging Eq. II-19:

$$K = \frac{N_{eff}}{N_{total}} = \frac{I_A \cdot I_B}{I_{A,B} \cdot N_{total}} \quad \text{Eq. II-20}$$

The number of detected secondary ions A can be normalized to the number of effective impacts. Such ratio represents the effective yield (Y_A^{eff}), which can be derived from Eq. II-19:

$$Y_A^{eff} = \frac{I_A}{N_{eff}} = \frac{I_{A,B}}{I_B} \quad \text{Eq. II-21}$$

The concept of effective yield is applied in Chapter IV to investigate the size effect of free-standing nanoparticles on secondary ion emission.

Sample Preparation

The sample preparation procedures used to disperse different nano-objects on substrates are described in detail in the next chapters.

CHAPTER III

CHARACTERIZATION OF BIOLOGICAL NANO-OBJECTS WITH NANOPROJECTILE-SIMS*

Introduction

The characterization of individual nano-objects presents new challenges for SIMS. As their size decreases vs. the volume required for full projectile energy dissipation, one reaches confined sample volumes, which can lead to a shift in secondary ion emission.[38] The latter can be further affected by the nature of the substrate supporting the nano-objects. We present here the case of SIMS applied to the characterization of biological nano-objects of "subcritical assay dimensions", specifically two types of nanometric bacteriophages. Our approach uses event-by-event bombardment/detection, involving bombardments with individual 520 keV Au_{400}^{4+} and identification of the ejecta from each individual impact. Provided individual nano-objects are spatially isolated on the surface, the secondary ions from an impacted object can be collected and resolved from those of other objects or the substrate. Thus compositional information specific to the objects can be obtained using the coincidence method.[31]

A critical issue in the study of individual nano-objects is to maintain their physical and chemical integrity during examination. Unanticipated chemical reactivity can occur with nano-sized objects. For instance, a mix of individual polystyrene nanospheres and

* This chapter is reprinted with permission from "Characterization of Biological Nano-Objects with Nanoprojectile-SIMS" by Liang, C.-K., Verkhoturov, S.V., Bisrat, Y., DeBord, J.D., Fernandez-Lima, F.A., Schweikert, E.A., Della-Negra, S. *Surf. Interface Anal.* **2013**. Copyright 2012 John Wiley and Sons.

boehmite alumina whiskers can lead to the formation of nanocomposite flakes due to the electrostatic nature of the whiskers.[43] For the present study, we deposited the bacteriophages on a NALDI™ plate, which features a surface made of silicon nanowires of 20 nm in diameter and 100-500 nm in length.[57] The silicon nanowires on the plate provide a suitable platform to deposit individual nano-objects. Moreover, the surface of the nanowires is functionalized with (pentafluorophenyl)propyldimethylsilane,[58] which makes the substrate inert to bio-objects and hence preserves their integrity.

The bacteriophages investigated here are Qβ and M13 phages as models of complex nano-objects. The first phage is spherical, 25 nm in diameter, and encapsulates a single-stranded RNA within the protein shell assembly.[59] The second is filamentous, 900 nm in length, 7-9 nm in width, and encapsulates a circular single-stranded DNA.[60] In both cases, secondary ions from both the protein shell and the encapsulated ribonucleotides were identified in the conventional (total) mass spectra and resolved from those of the underlying nanowires in the coincidence mass spectra.

Experimental

Sample Preparation

M13 phage was purchased from New England Biolabs Inc. (Ipswich, MA). Qβ phage was provided by R. Young (Texas A&M University). NALDI™ plates were provided by Bruker Daltonics Inc. (Billerica, MA). Desalting columns were purchased from Bio-Rad (Hercules, CA). The original buffer in the desalting columns was exchanged by deionized water (18.2 MΩcm, Millipore, Billerica, MA) four times based on the buffer exchange protocol provided by the manufacturer. Each phage sample was

diluted by mixing 1 μL of stock phage solution with 49 μL of deionized water. The diluted phage solution was eluted through the desalting column to remove most of the salt and glycerol used to preserve phages. The eluate was collected and drop-casted onto a 1x1 cm^2 NALDI^{TM} plate.

SEM Examination

A Jeol-7500 Cold Field Emission scanning electron microscope was used to examine the integrity of the phages on the NALDI^{TM} plates. These plates have a stainless steel backing, thus they are not affected by charging. They were attached to the specimen holders with carbon tape. Electron beam conditions are noted in Figure III-1.

Results and Discussion

The SEM images of the Qβ and M13 phages on the NALDI^{TM} plates (Figure III-1) show that the phages are spatially dispersed with their integrity preserved. We note negligible agglomeration after deposition onto the nanowire-modified surface. The examination of the Qβ phages with SEM could only be accomplished in the electron backscattering mode. In this mode we obtained a weak electron signal from the Qβ phages; however, the underlying Si nanowires were invisible. The SEM images were also affected by salt deposit. We base our claim of isolated Qβ phages on the NALDI^{TM} plate on: a) the fact that we deposited the phages from a very diluted solution (concentration similar to the M13 phage solution); b) on the SEM image showing (weak) backscattered electron signal from isolated phages. The mass spectral data are from a 500 μm area bombarded stochastically with 1 to 5 million Au_{400}^{4+} projectiles. A small amount of impacts (84k and 18k for the Qβ and M13 phage respectively) occurred on an

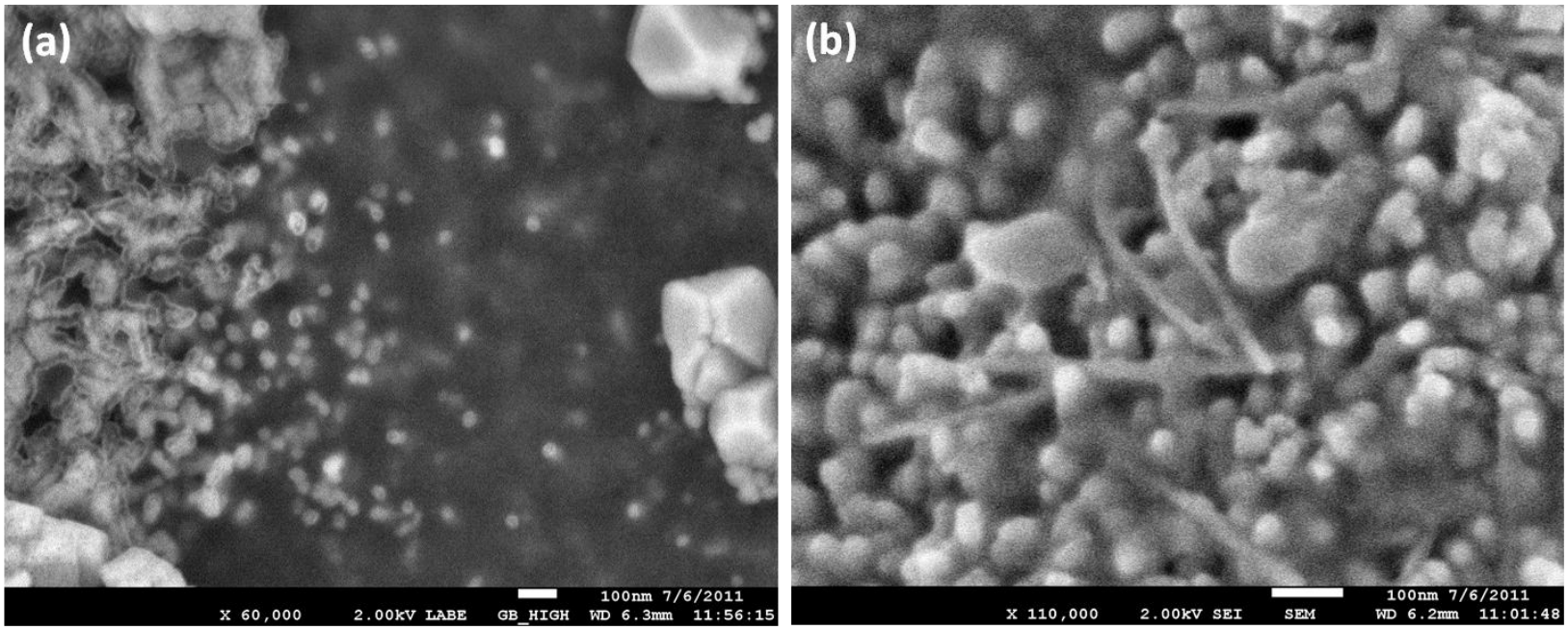

Figure III–1. SEM Images of bacteriophages deposited onto the NALDI^{TM} plates. (a) spherical Qβ and (b) filamentous M13 phages (scale bar = 100 nm).

individual bacteriophage. We refer here to impacts where the ion emission met the coincidence/anticoincidence conditions. Data from these selected events were summed for statistics.

The total mass spectrum of the Qβ phage on the NALDI^{TM} plate is presented in Figure III-2. The spectrum of M13 phage shares similar features (Figure III-3). Substrate signals can be identified at m/z 267 as the intact molecular ion of the surface modifier ((pentafluorophenyl)propyldimethylsilane), and m/z 19, 101, 217 as fragments from the modifier. The presence of salt causes an isobaric interference at m/z 267 ($(NaCl)_4Cl^-$). Signals relevant to the phage mainly reside in the mass range from m/z 100 to 200, including amino acid residues from the protein shell assembly and nucleobases of the encapsulated ribonucleotides. The formation of Au adducts, e.g. $Au(CN)H^-$ and $Au(CN)_2^-$, results from the process where Au atoms are ablated from the massive Au projectile and then recombine with CN^- fragments from the objects.[61]

To resolve compositional information of the nano-objects from that of the substrate, coincidence mass spectra can be obtained using the co-emitted secondary ions from those events containing ion emission specific to the objects. The intensity of ions in the coincidence mass spectrum is normalized with the number of the selected events. The coincidence mass spectrum displayed in Figure III-4b shows ions co-emitted with $[Adenine\text{-}H]^-$ from the Qβ phage. Peaks specific to the phage are enhanced in the coincidence mass spectrum; however, peaks corresponding to the substrate at m/z 19 and

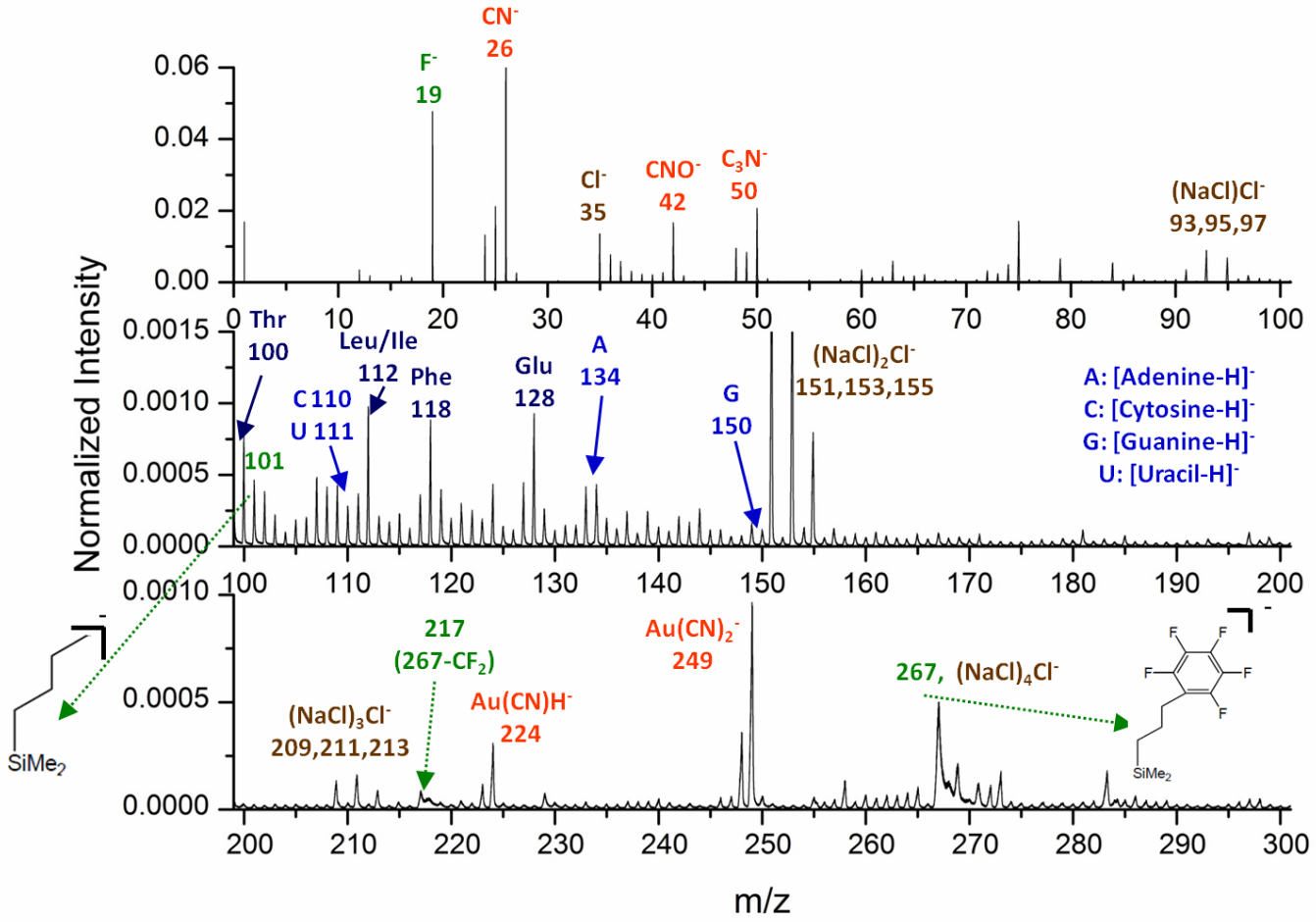

Figure III–2. Negative ion mass spectrum of the Qβ phages on the NALDI^{TM} plate. Intensities are normalized to the total number of projectile impacts.

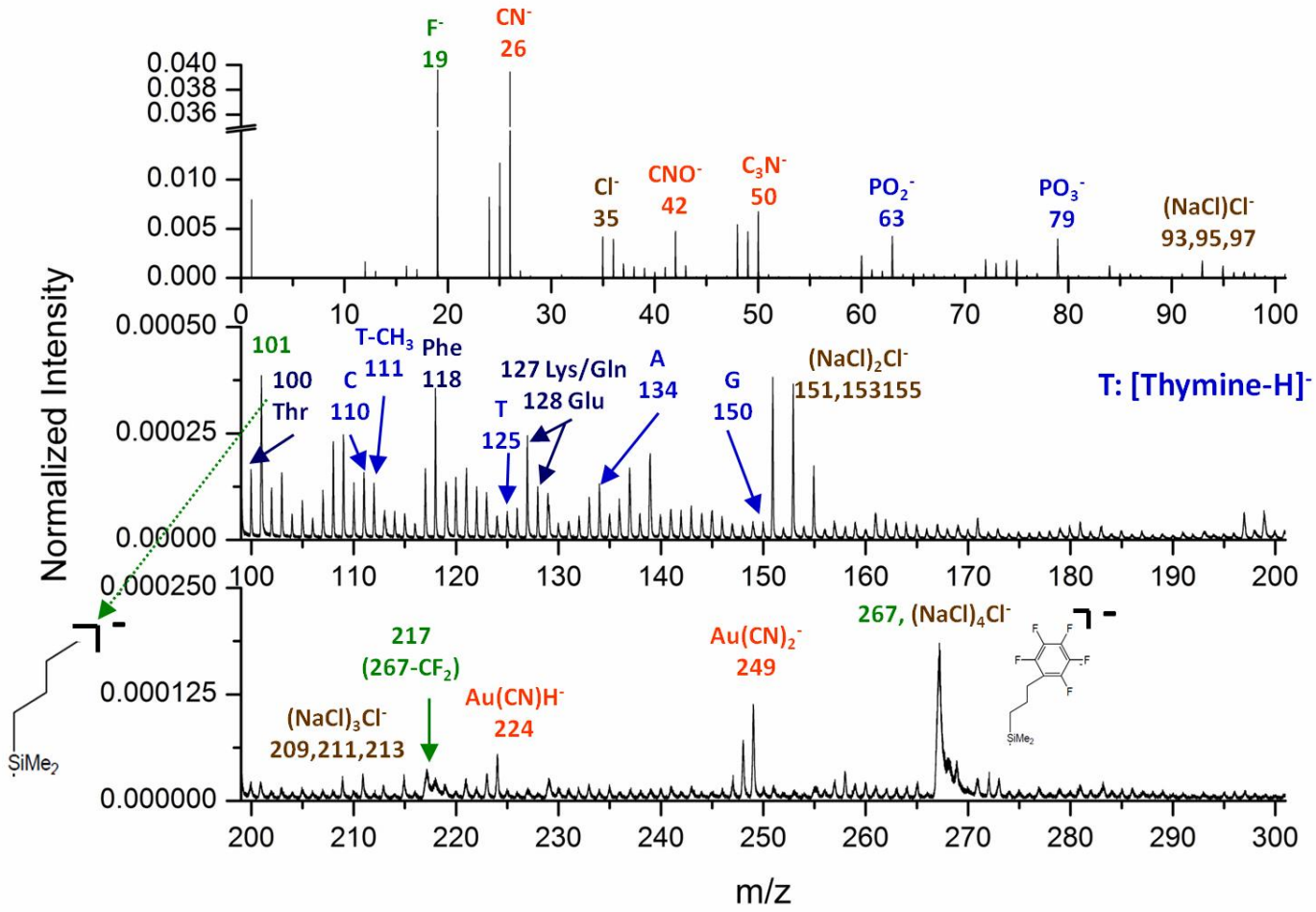

Figure III–3. Negative ion mass spectrum of the M13 phages on the NALDI^{TM} plate. Intensities are normalized to the total number of projectile impacts.

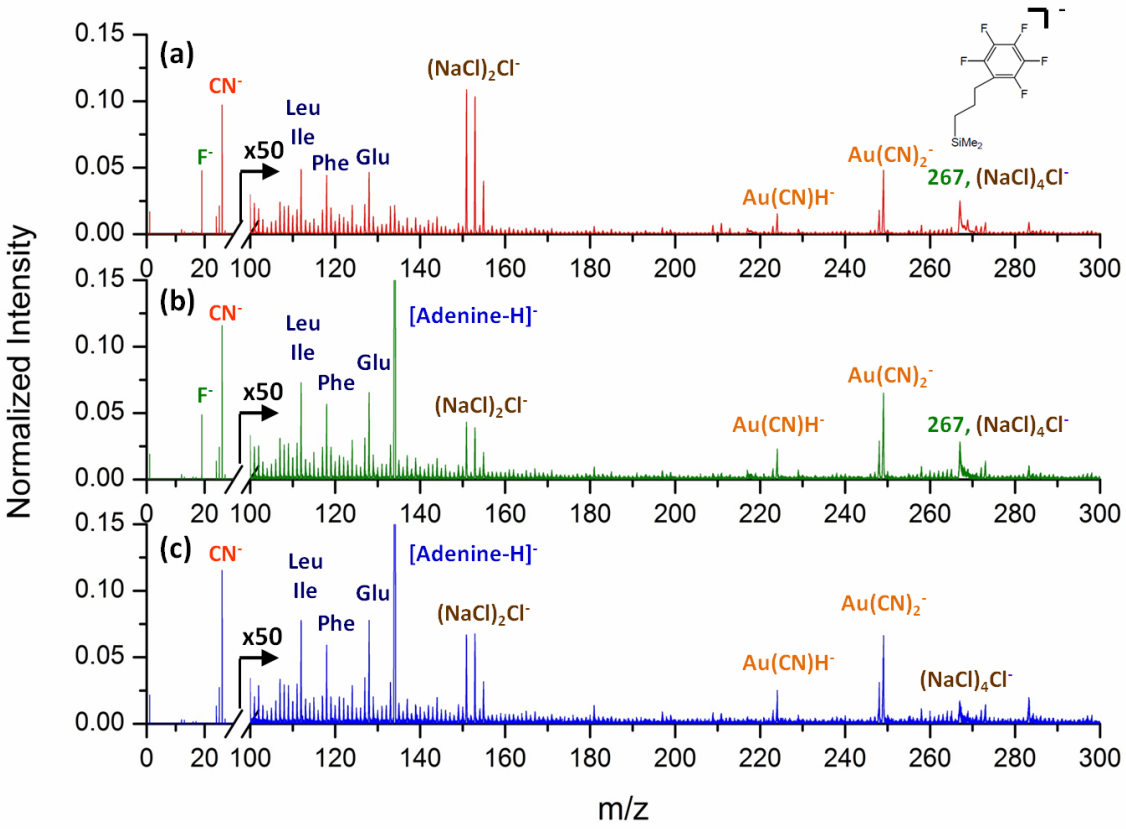

Figure III–4. Total, coincidence, coincidence/anticoincidence spectra of Qβ phage. (a) Total mass spectrum of the Qβ phages on the NALDI^{TM} plate. (b) Coincidence spectrum composed of ions co-emitted with $[Adenine\text{-}H]^-$. (c) Coincidence/anticoincidence spectrum composed of events containing $[Adenine\text{-}H]^-$ but without F^-. Intensities in spectra (b) and (c) are normalized to the corresponding number of selected events.

267 are still present. The remaining substrate signals can be attributed to impacts on the regions where phages and nanowires are in physical contact, *i.e.* grazing impacts.

Compared to the grazing impacts, direct or "bulls-eye" impacts on the Qβ phage are expected to yield specific information to the phage because the resulting ejecta originate only from the inside or the top of the nano-objects. Based on the difference in ejecta from these two types of impacts, a mass spectrum derived only from bulls-eye impacts on the Qβ phage can be extracted from the parent coincidence mass spectrum by removing the events containing substrate specific ions. This additional selection is based on an anticoincidence with the substrate specific ions. The new coincidence/anticoincidence mass spectrum presented in Figure III-4c is constituted by events containing $[\text{Adenine-H}]^-$ but without F^-. The peak at m/z 19 is therefore absent from the spectrum, and the peak at m/z 267 is largely decreased but not totally eliminated. The remaining signal is attributed to the isobaric ion $(NaCl)_4Cl^-$ and to the events in which F^- was not detected.

The total spectrum of the M13 phage was processed with the same methodology and the resulting coincidence and coincidence/anticoincidence mass spectra are presented in Figures III-5b and III-5c. It is noteworthy that the decrease of peak at m/z 267 is more prominent in the coincidence mass spectrum compared to that for Qβ phage. This is due to not only the fact that there is a lower salt content which causes isobaric interference but also to the fact that the long M13 phages provide many more sites for bulls-eye impacts per phage. The ratio of the number of events in the coincidence/anticoincidence mass spectrum to the number of events in the coincidence

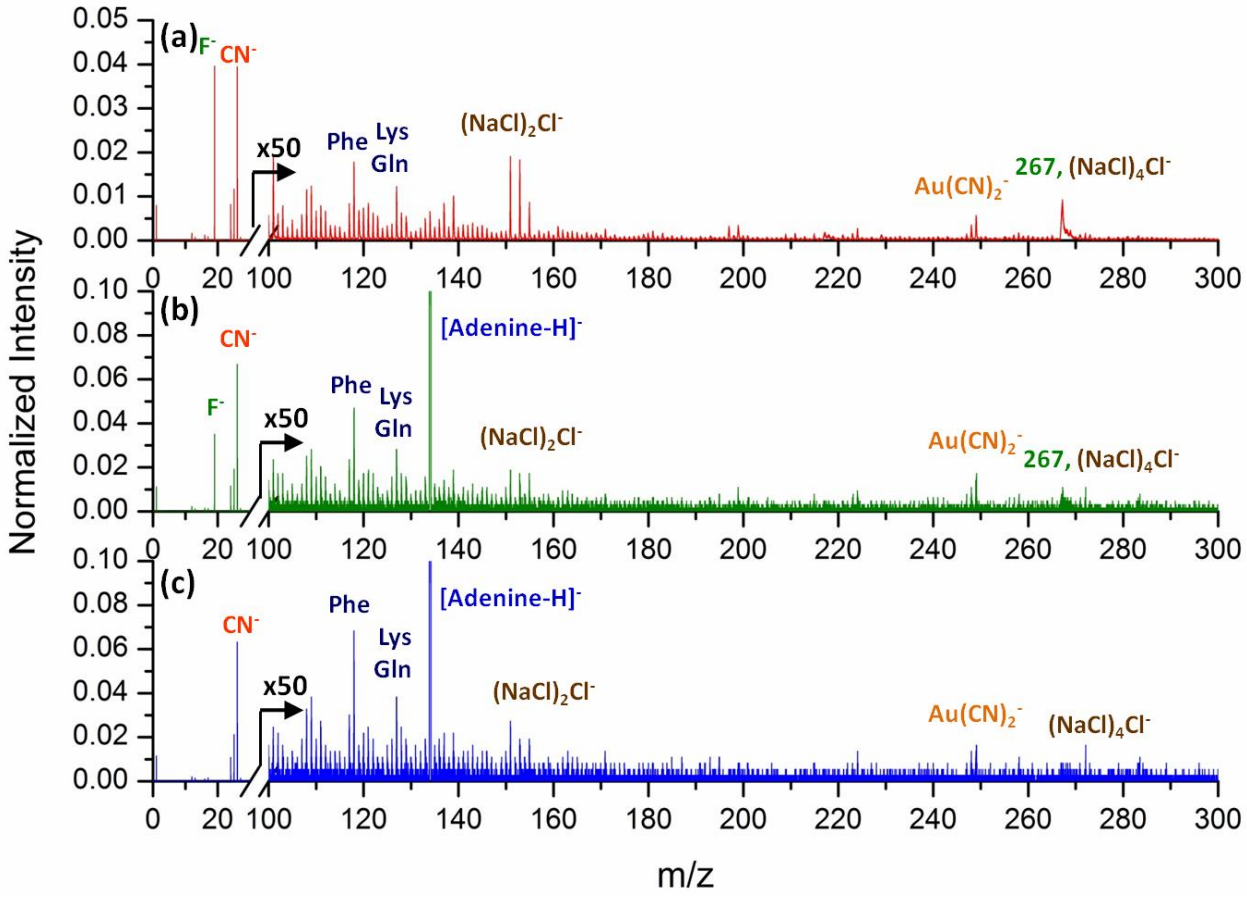

Figure III–5. Total, coincidence, coincidence/anticoincidence spectra of M13 phage. (a) Total mass spectrum of the M13 phages on the NALDI^{TM} plate. (b) Coincidence spectrum composed of ions co-emitted with [Adenine-H]$^-$. (c) Coincidence/anticoincidence spectrum composed of events containing [Adenine-H]$^-$ but without F$^-$.

mass spectrum is larger for M13 phage than Qβ phage (57% v.s 44%). This ratio represents the proportion of bulls-eye impacts among bulls-eye and grazing impacts. In addition, the presence of phage-related ions in the coincidence/anticoincidence mass spectrum also implies that the depth of emission of the projectile might be close to the width of the M13 phage, which is ~7-9 nm. If the depth of emission is larger than the width, ejecta from bulls-eye impacts would most likely include ions from both the phage and the underlying substrate. Thus we could not obtain a mass spectrum of the phage shell or core alone.

Conclusion

We present a characterization of individual bacteriophages isolated on a nanostructured substrate. This approach preserves the integrity of the bio-objects studied. The event-by-event bombardment/detection mode allows one to extract chemical information from individually dispersed nano-objects. The coincidence methodology provides primary selection of object-specific information out of the total mass spectrum. The combination of coincidence with anticoincidence demonstrates further resolution between two types of impacts on nano-objects. The effectiveness of the approach depends on both the size and shape of the nano-objects, which affect the proportion of bulls-eye impacts and grazing impacts. Further resolution may be achieved incorporating additional coincidence or anticoincidence. The scope of coincidence/anticoincidence signal selection in ion co-emission analysis is limited only by the data required for statistical validation.

CHAPTER IV

SIZE-DEPENDENT EMISSION OF NEGATIVE IONS FROM GOLD NANOPARTICLES BOMBARDED WITH C_{60} AND Au_{400}*

Introduction

The uniqueness of nanoparticles, NPs, due to their functionalities not present in bulk size is well documented.[1] A nuanced understanding of their functionalities depends on their accurate characterization. A recent review summarizes the application of pertinent physical and chemical analysis techniques including scanning tunneling microscopy (STM), atomic force microscopy (AFM), scanning electron microscopy (SEM), scanning-probe microscopy (SPM), X-ray photoelectron spectroscopy (XPS), low-energy ion scattering (LEIS) and time-of-flight secondary ion mass spectrometry (ToF-SIMS).[7] The latter is inherently well suited for the isotopic to molecular characterization of NPs. However, for objects of nano-scaled dimensions, the volume sampled in a SIMS measurement becomes an issue. The bombarding ions used for generating secondary ion, SI, emission penetrate solids to depths of up to tens of nanometers depending on their nature, kinetic energy and mode of penetration.[62] If the NPs are smaller than the projectile's range, there will be in incomplete energy deposition. Moreover, the energy deposited in an individual NP cannot be dissipated as in a semi-infinite solid.[40] The consequences for sputter and ion yields from a confined volume

* This chapter is reprinted with permission from "Size-Dependent Emission of Negative Ions from Gold Nanoparticles Bombarded with C_{60} and Au_{400}" by Liang, C.-K., Verkhoturov, S.V., Chen, L.-J., Schweikert, E.A. *Int. J. Mass Spectrom*. **2013**.

sample have been evaluated in molecular dynamic simulations and measured experimentally. Briefly, enhanced sputter yields have been predicted[40,41] and observed[42]. Regarding the emission of SIs, shifts in mass distribution and abundance have been reported.[38] They suggest that size-dependent SI emission occurs from NPs measuring somewhere below 50 nm. We present here a study examining SI emission from NPs of 2 to 50 nm in diameter. We consider the case of NPs dispersed on a solid substrate to eliminate interaction effects among close neighbors. A practical issue is to maximize SI emission from the minute amount of material in NPs. Massive projectiles, in practice C_{60} and Au_{400}, are most effective for producing SIs. They deposit their kinetic energy in nano-scaled volumes. We examine with these projectiles the size-dependent SI emission at the level where one bombarding ion impacts one NP.

Experimental

Preparation of Dispersed AuNPs

P-doped Si (100) wafers and gold-coated wafers (Silicon Valley Microelectronics, Santa Clara, CA) were cut into ~1x1 cm^2 pieces and cleaned by sonication in dH_2O, absolute ethanol, and O_2 plasma cleaner. The treated Si wafer pieces were dipped into poly(diallyldimethylammonium chloride) (PDDA, Aldrich, Milwaukee, WI) solution (5 mg/mL in 0.5 M $NaCl_{(aq)}$) for 15 min, rinsed with dH_2O for 5 sec, and dried under a gentle N_2 stream. The PDDA-modified Si wafers were immersed in 1 mL AuNPs solution (2, 5, 10, 15, 20, 50 nm, BBInternational, Cardiff, UK). The immersion time differs depending on sample size: 15, 20 nm: 1 hr, 50 nm: 3 hr, 2, 5, 10 nm: 4 hr. The

resulting AuNPs/PDDA/Si wafers were rinsed with dH_2O to remove excess AuNPs and dried under a gentle N_2 stream.

SEM Examination

A scanning electron microscope (SEM; Jeol-7500 Cold Field Emission) was used to confirm the formation of a submonolayer of discrete AuNPs on the substrate for each sample. SEM operated in secondary electron mode was used to image the presence of AuNPs larger than 2 nm but backscattering mode for the 2 nm AuNPs.

Results and Discussion

Examination of Individually Dispersed AuNPs

As indicated earlier, an assessment of the SI emission from the bombardment of individual NPs requires that the AuNPs be spatially dispersed. The substrate modified with the positively charged PDDA immobilized the anion-coated AuNPs *via* electrostatic interaction. The repulsion from the anionic coating prevented the AuNPs from agglomeration on the substrate. The SEM images (Figure IV-1) verify the formation of a submonolayer of discrete AuNPs on the substrate. It must be noted that the 2 nm AuNPs were at the limit of the spatial resolution of the SEM. The image of the 2 nm AuNPs was taken in the backscattering mode.

SIMS Investigation of Individual AuNPs - 520 keV Au_{400}^{4+}

Given that both the projectile and the NPs are of the same element, it is critical to validate the signals used for analysis as being characteristic of the AuNPs, i.e. not originating from the projectiles but the AuNPs. Figure IV-2 shows the comparison of negative ion mass spectra between a 20 nm AuNPs/PDDA/Si wafer (top) and a

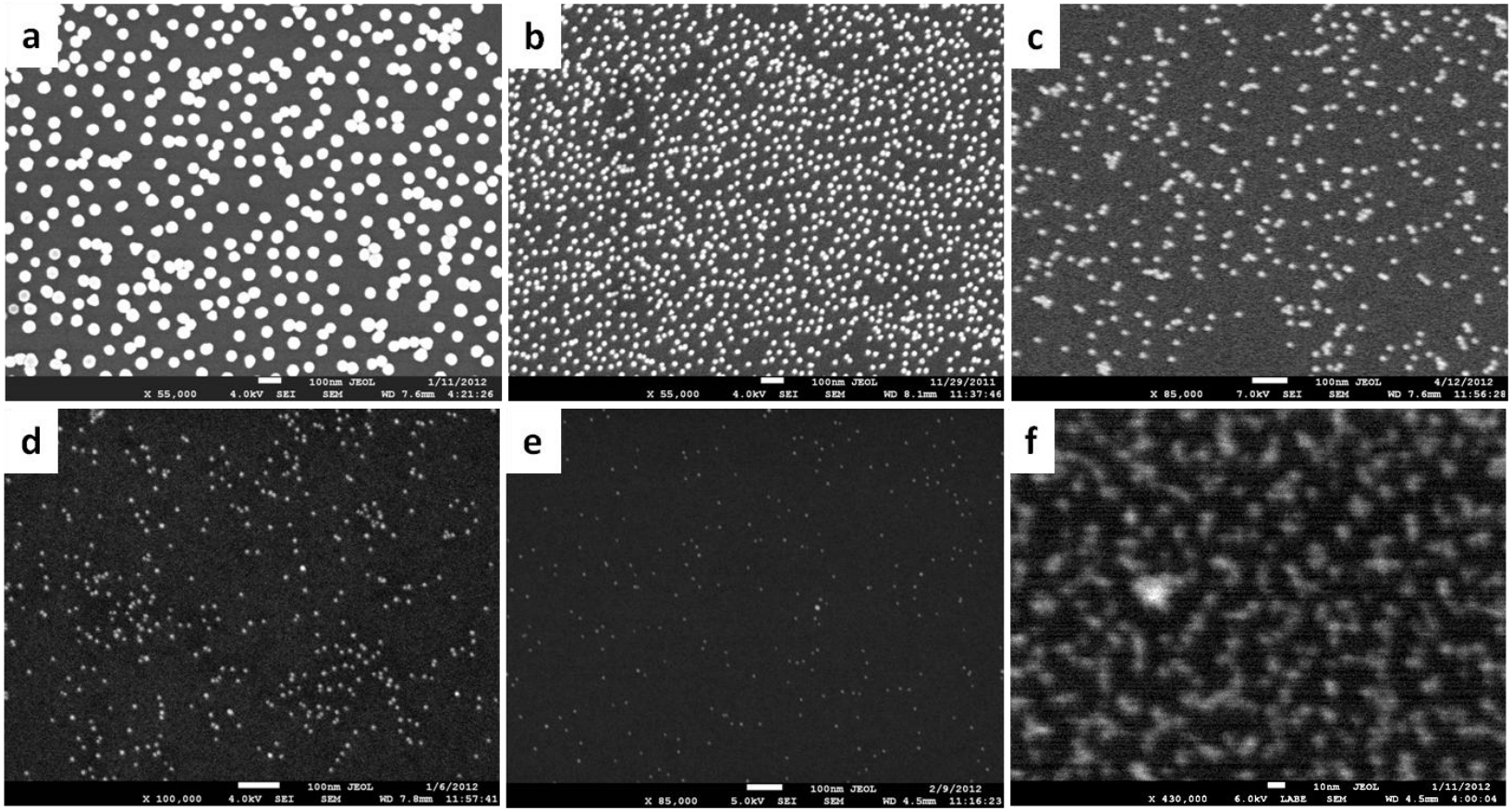

Figure IV–1. SEM images of AuNPs on PDDA-modified Si wafers. (a) 50 nm, (b) 20 nm, (c) 15 nm, (d) 10 nm, (e) 5 nm and (f) 2 nm AuNPs. Scale bar: 100 nm (a-e), 10 nm (f).

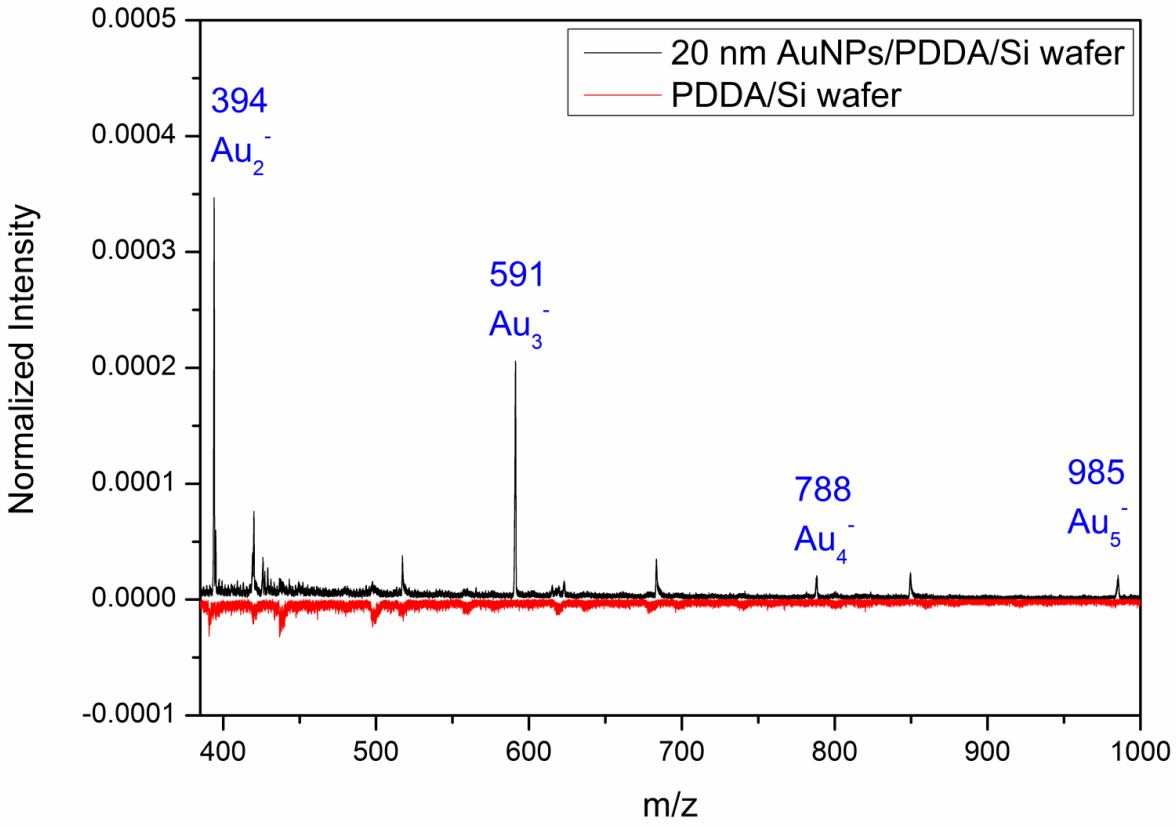

Figure IV–2. Negative secondary ion mass spectra of 20 nm AuNPs on PDDA-modified Si wafer (top) and PDDA-modified Si wafer (bottom) impacted with 520 keV Au_{400}^{4+} projectiles.

PDDA/Si wafer (bottom). The Au cluster ions (Au_n^-, $n \geqq 2$) are only present in the top mass spectrum, indicating the Au clusters only result from the AuNPs. The wafer deposited with a layer of gold is included for comparison as an example of bulk gold. The gold layer is thick enough that no Si-relevant signal from the underlying substrate was detected.

The maximum size of ejected clusters is dependent on the size of the AuNPs. Clusters up to Au_9^- were observed for NPs of 15 and 20 nm, up to Au_6^- for NP of 10 nm, whereas only Au_2^- and Au_3^- were observed for NPs of 2, 5 and 50 nm. In the case of bulk sample, the largest cluster observed was Au_5^-. The difference in ejecta sizes between 50 nm and the flat sample is discussed below. Further, the SI yields of Au_n^- also depend on the number of constituents: the yields for clusters with odd numbers of atoms are higher than the neighboring even-numbered clusters except for Au_3^-. The trend can be explained by the electron pairing effect.[63] The odd-sized clusters have an odd total number of valence electrons and the highest occupied molecular orbital (HOMO) is singly occupied. Therefore, the formation of anionic odd-sized clusters is favored. The trend does not hold for Au_2^-, which is emitted with a higher yield than Au_3^-. We attribute the discrepancy to the high energy density impact which leads to extensive fragmentation. For the projectile-target characteristics considered here, the abundant production of Au_2 outweighs the effect of its relatively lower electron affinity.

Quantitative Analysis of Size Effect on SI Emissions – Effective Yield

Au_2^- and Au_3^- were chosen to compare the Au cluster emission among different particle sizes. Conventionally, the SI emission is quantified by the SI yield, which is defined as the intensity of ion of interest normalized to the total number of impacts. However, the SI yield will be underestimated for samples with a submonolayer of analyte, in that only a portion of impacts account for the bombardments on the NPs. Thus the ion intensity must be normalized to the number of impacts effective for emission, i.e. number of effective impacts (N_e). The resultant effective yield (Y^{eff}) of a specified Au_n^- is independent of coverage of AuNPs and can be compared among samples of different particle sizes.

Additionally, the impacts on NPs have different impact parameters.[40] One can consider three types: direct impacts, grazing impacts on the edge of particles, and in the case of NPs smaller than 5nm, impacts resulting in interfacial emission, i.e. concurrent emission of Au clusters and species from the substrate. These may be the result of a projectile traversing the NP (range larger than the NP diameter) or an impact on a substrate site close enough to a NP for it to be included in the volume of excitation-emission. We describe below how the single impact acquisition technique can separate different types of impacts and measure the corresponding effective yields.

The effective yield is obtained experimentally based on the co-emission events. We consider here the events where the random number of cluster ions emitted/detected from one impact is $k^-_{Au_2}$ and $k^-_{Au_3}$ for Au_2^- and Au_3^- respectively.

One should mention here that we detect multi-emission events using an eight-anode detector. The procedure of computing the ion distribution from measured multi-emission events is described in ref [30]. The probability distributions $P(k^-_{Au_2})$ and $P(k^-_{Au_3})$ of the detected clusters per impact are related to the probability distribution of detected co-emission clusters $P\left(k^-_{Au_2}, k^-_{Au_3}\right)$ by:

$$P\left(k^-_{Au_2}, k^-_{Au_3}\right) = P\left(k^-_{Au_2}\right) \cdot P\left(k^-_{Au_3}\right) \quad \text{Eq. IV-1}$$

The distribution $P\left(k^-_{Au_2}, k^-_{Au_3}\right)$ is factorized given the independent emission of cluster ions from the nanovolumes containing thousands of atoms.[64] Normally, we calculate the mean values of these distributions (i.e. yields of detected clusters), which are:

$$Y^{eff}_{Au_2} = \sum_{k^-_{Au_2}} k^-_{Au_2} P\left(k^-_{Au_2}\right), \; Y^{eff}_{Au_3} = \sum_{k^-_{Au_3}} k^-_{Au_3} P\left(k^-_{Au_3}\right), \text{ and}$$

$$Y^{eff}_{Au_2,Au_3} = \sum_{k^-_{Au_2}} \sum_{k^-_{Au_3}} k^-_{Au_2} k^-_{Au_3} P\left(k^-_{Au_2}, k^-_{Au_3}\right).$$

The mean values of distributions (yields) are factorized as well:[65]

$$Y^{eff}_{Au_2,Au_3} = Y^{eff}_{Au_2} \cdot Y^{eff}_{Au_3} \quad \text{Eq. IV-2}$$

Eq IV-2 can be rewritten as follows:

$$\frac{I_{Au_2,Au_3}}{N_e} = \frac{I_{Au_2}}{N_e} \cdot \frac{I_{Au_3}}{N_e} \quad \text{Eq. IV-3}$$

where I_{Au_2,Au_3} is the detected number of co-emitted Au_2^- and Au_3^- in the coincidence mass spectrum, I_{Au_2} is the number of Au_2^- in the original mass spectrum while I_{Au_3} is

the number of Au_3^-. The effective number of impacts on AuNPs, N_e, is a statistical ensemble of the detected events of co-emission of Au_2^- and Au_3^-.

Thus the effective yield of Au_3^-, for example, can be deduced by rearranging Eq IV-3:

$$Y_{Au_3}^{eff} = \frac{I_{Au_3}}{N_e} = \frac{I_{Au_2,Au_3}}{I_{Au_2}} \quad \text{Eq. IV-4}$$

From the same point of view, the conventional yields of Au_n^- obtained from the gold wafer are deemed equivalent to their corresponding effective yields since every projectile impact is expected on gold.

Figure IV-3 presents the effective yields of Au_2^- and Au_3^- as a function of particle size with standard deviations of replicate measurements shown as error bars. The effective yields for both clusters increase as the particle size increases, reaching a maximum at 20 nm, and dropping at 50 nm to a level comparable to the bulk gold wafer. For particles ranging from 2 to 10 nm, the increase in yield is attributed to the increasing amount of gold atoms per particle and decreasing extent of fragmentation/atomization. No species with n>3 were detected from NPs below 10 nm, suggesting that the 2 and 5 nm NPs are too small to accommodate the full energy dissipation from the projectiles. High energy density prevails in these volumes, leading to extensive NP fragmentation/atomization. Intermediate size AuNPs (15, 20 nm) show higher yields. At these sizes we observe optimum conversion of the projectile momentum imparted into a free-standing NP into SI emission. The ejecta include clusters up to Au_9^-, indicating that

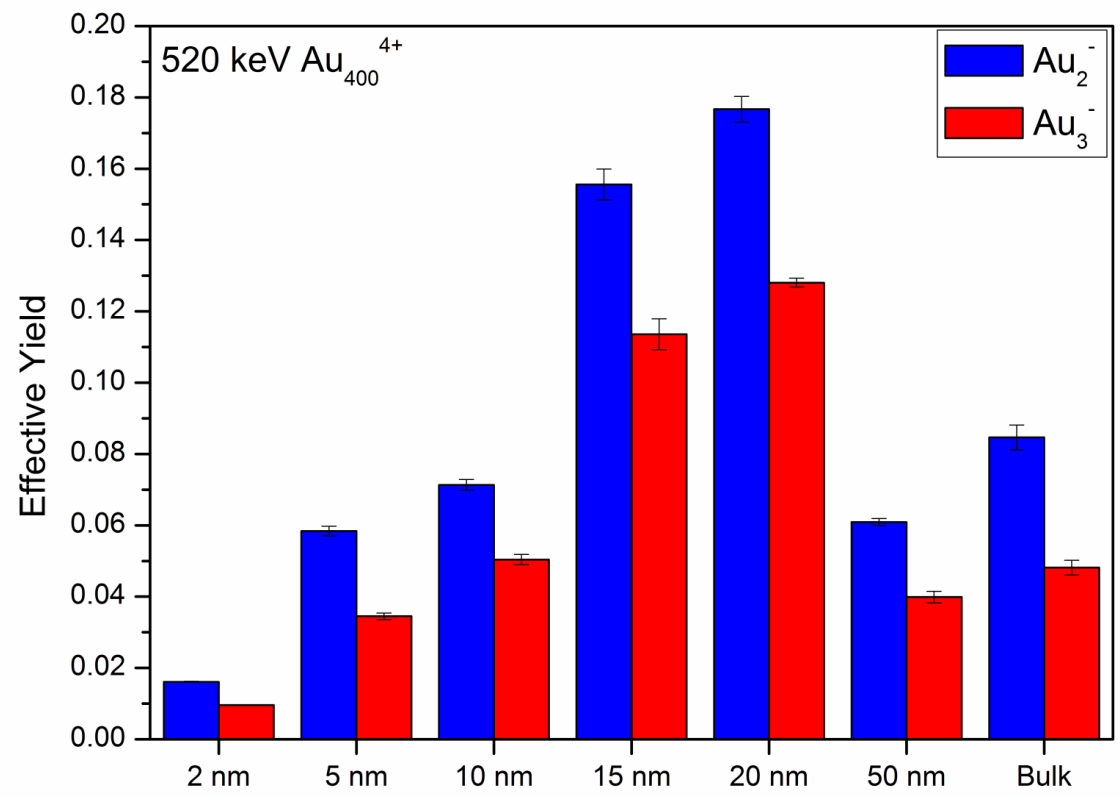

Figure IV–3. Effective yields of Au_2^- and Au_3^- from AuNPs of different sizes and Au wafer impacted with 520 keV Au_{400}^{4+} projectiles.

for 15-20 nm NPs the projectile energy is more efficiently partitioned into fragmentation rather than atomization. Compared to the bulk case, the projectile impacts on the 20 nm AuNPs yield Au_2^- and Au_3^- emissions that are ~2.1 and 2.7 fold higher respectively. When the particle size exceeds the interaction volume of the projectile, as for the 50 nm AuNPs, the SI emission is similar to that from the bulk. However, the yield of Au_2^- is 30% less than that from the gold wafer and for Au_3^- the yield is lower by 20%. The lower yields and the fact that larger clusters were not detected are attributed to particle-target geometry. The projectile angle of incidence on spherical particles runs from 0 to 90˚ vs. the 45˚ angle on a flat surface. The signals from the 50 nm AuNPs likely include impacts with partial energy transfer where the deposited energy is insufficient for gold cluster emission comparable to that from a flat semi-infinite surface.

As noted earlier, the enhanced emission of larger gold clusters is also observed for 10, 15 and 20 nm AuNPs compared to the gold wafer. The effective yields of Au_4^- and Au_5^- were obtained from the co-emission events containing Au_2^- and Au_4^-/Au_5^- using the aforementioned method. As shown in Table IV-1, all gold cluster emissions are enhanced in 2 to 3 fold in the cases of 15 and 20 nm AuNPs. For 10 nm AuNPs, the effective yields of Au_4^- and Au_5^- are 1.3 times higher. No enhancement was observed in the emission of Au_2^- and Au_3^-.

Projectile- and Size-Dependent SI Emissions – 50 keV C_{60}^{2+}

The same samples were examined with C_{60} projectiles. With the latter there is no ambiguity about the origin of the Au clusters. However, the ion at m/z 197 was not

Table IV-1. Effective yields of Au_4^- and Au_5^-. Yields were calculated in coincidence with Au_2^- for nanoparticle and bulk samples examined by 520 keV Au_{400}^{4+} projectiles.

	2 nm	5 nm	10 nm	15 nm	20 nm	50 nm	wafer
Au_4^-	ND	ND	0.0059	0.0105	0.0121	ND	0.0044
Au_5^-	ND	ND	0.0065	0.0123	0.0146	ND	0.0049

ND: not detected

Table IV-2. Ratios, $Y_{eff,Au_n}(Au_{400})/Y_{eff,Au_n}(C_{60})$, for nanoparticle and bulk samples.

n	2 nm	10 nm	20 nm	50 nm	wafer
2	1.8	5.5	25.1	8.9	11.1
3	1.2	3.2	14.6	5.1	5.2

Table IV-3. Effective yields of Au_2^-. Yields were calculated in coincidence with Au_2CN^-, Au_3^-, and $Si_3O_7H^-$ for nanoparticle samples examined by 520 keV Au_{400}^{4+} projectiles.

	2 nm	5 nm	10 nm	15 nm	20 nm	50 nm
$Au_2(CN)^-$	0.013	0.023	0.060	0.140	0.141	0.033
Au_3^-	0.014	0.052	0.074	0.159	0.185	0.058
SiO_3H^-	0.007	0.001				

considered as a characteristic of the AuNPs due to an isobaric interference from the Si wafer ($Si_3O_7H^-$). Larger gold clusters were observed in comparison with those observed in the case of Au_{400} impacts except for 20 nm AuNPs. Clusters up to Au_7^- can be observed for 2, 10, 20 nm AuNPs; Au_5^- and Au_{10}^- for 50 nm and gold wafer respectively. The SI yields of Au_n^- also follow the trend of odd-even oscillation except for Au_2^- in the case of the 2 nm AuNPs.

With C_{60} there is again NP size-dependent SI emission. The yields for Au_2^- and Au_3^- are presented in Figure IV-4. The highest yields of Au_2^- and Au_3^- were recorded from the 10 nm AuNPs. The emission of both clusters is higher than that of gold wafer by a factor of 1.7. The effective yields of other size AuNPs are similar to those from the flat gold surface. Moreover, the C_{60} impacts favor the formation of Au_3^- except for the 2 nm AuNPs, whereas the formation of Au_2^- is dominant in the cases of Au_{400} impacts.

The different features observed for the two types of projectiles can be attributed to their modes of interaction and the respective energy densities deposited in the AuNPs. In the case of Au_{400} impacts, we have inherently the condition for the most efficient energy transfer in the NPs. The cohesive energies of NPs vary as a function of the number of atoms in a given particle[66] and were calculated according to ref [67]. The energy density deposited from the 520 keV Au_{400}^{4+} is sufficient for breaking all bonds in AuNPs up to ~15 nm. For 20 nm AuNPs, the energy density is smaller (2.11 eV/atom) than the corresponding cohesive energy (3.76 eV/atom) with a concomitant increase in emission of clusters. A different mechanism of energy transfer operates in the case of C_{60} impacts.

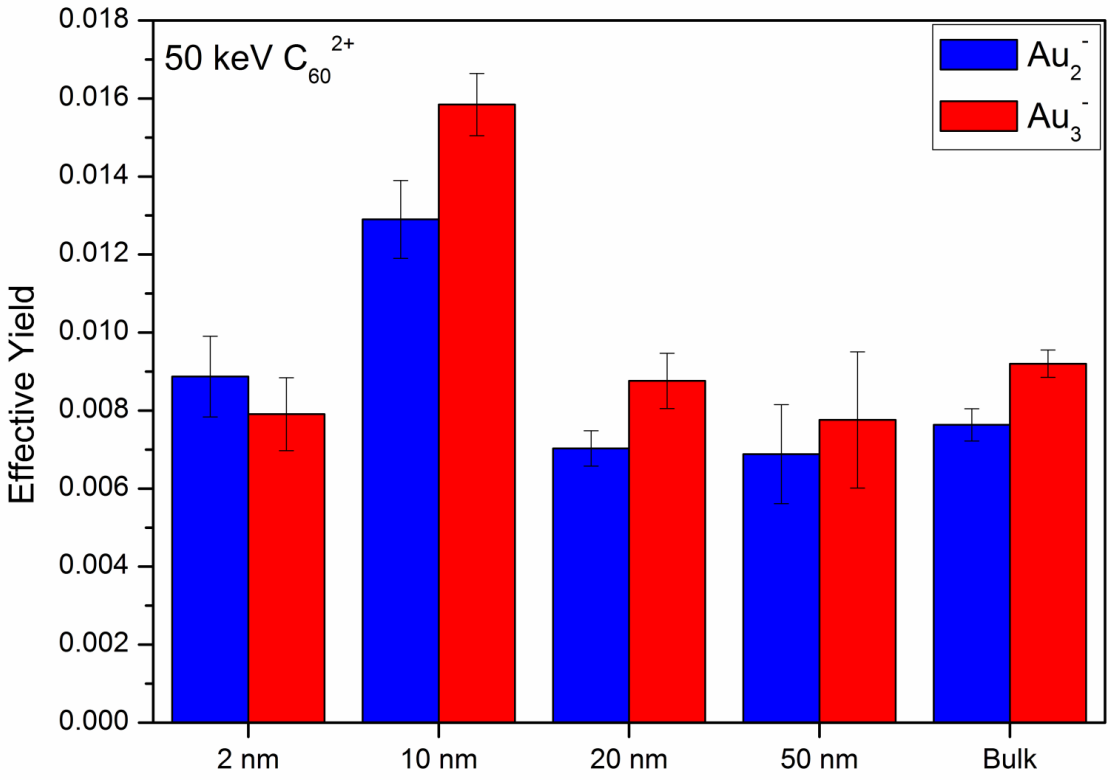

Figure IV–4. Effective yields of Au_2^- and Au_3^- from AuNPs of different sizes and Au wafer impacted with 50 keV C_{60}^{2+} projectiles.

The C_{60} projectile has a comparable energy per constituent atom (0.8 keV vs. 1.3 keV (Au_{400})) but much lower projectile/target atomic mass ratio. The hollow C_{60} particles shatter on collision with the AuNPs, and a fraction of projectile energy is lost with the backscattered carbon atoms.[68] The projectile energy is partially transferred to the outer shell of the particles. Surface curvature becomes important, as evidenced in the enhanced emission from the 10 nm AuNPs. Additionally, the lower energy density imparted by C_{60} mitigates extensive fragmentation/atomization, as indicated by the presence of larger gold clusters observed from all samples except for 20 nm AuNPs and by the higher abundance of Au_3^- than Au_2^- for particles larger than 2 nm.

Overall, the 520 keV Au_{400} impact is more efficient than 50 keV C_{60} in terms of yielding SI emission. The lower SI yields and multiplicity, i.e. the number of co-emitted SIs per event, afforded by C_{60} impacts make calculation of effective yields more difficult for larger gold clusters. Table IV-2 shows the ratios generated by comparing $Y^{eff}_{Au_2}$ and Y^{eff}_{Au3} obtained from Au_{400} impacts to those from C_{60} impacts. The effectiveness of the Au_{400} impacts on 20 nm AuNPs is most pronounced. However, both projectiles perform comparably in the case of 2 nm AuNPs. Both provide sufficient energy for emissions of Au_2^- and Au_3^- in spite of different energy densities.

Influence of the Impact Parameters of Au_{400} Projectile on the Effective Yield

A further question is how different types of impacts affect the SI emission. We have explained above that direct impacts can be identified *via* the co-emission of Au_2^- and Au_3^-. Grazing and interfacial impacts may be revealed with the co-emission of Au_2^- and

Au_2CN^-. The latter requires the interaction of Au_2^- with CN^- from the substrate and occurs at the level of single impacts. The mechanism(s) of assembly and emission may be a convolution of atomization-recombination[61] and "pick-up and lift".[69]

The effective yields of Au_2^- co-emitted with Au_2CN^- are shown in Table IV-3. They are lower than the effective yields of Au_2^- co-emitted with Au_3^- for all sizes of NPs except 2 nm. Clearly, direct impacts on NPs of sufficient size to accommodate the energy transient do not produce adducts.

The 2 nm NP is of special note. Let's consider the effective yields pertaining to Au_2CN^- and Au_3^-. Any one of the direct, grazing or interfacial impacts causes emission from an area larger than the 2 nm size of the NP. Figure IV-5 illustrates schematically the differences between impacts on a "large" 50 nm NP and a "small" 2 nm one. In the case of the latter, we observe co-emission of SiO_3H^- with Au_2^-. The data in Table IV-3 show that such interfacial impacts can also occur with 5 nm NPs but were not detected with larger NPs. Thus, the statistics of effective impacts for emission of Au clusters is different for 2 nm particles. Here the distinction between direct, grazing and interfacial impacts is blurred.

Size Effect on AuNP Ionization Probability

The yield dependence on the size of the NP suggests a variation of ionization probability. The mechanism for negative ion emission initiated by large cluster and NP impacts remains to date unclear, due to a lack of data on ionization probability. In atomic ion impact, ionization proceeds mainly by electron exchange between sputtered neutrals

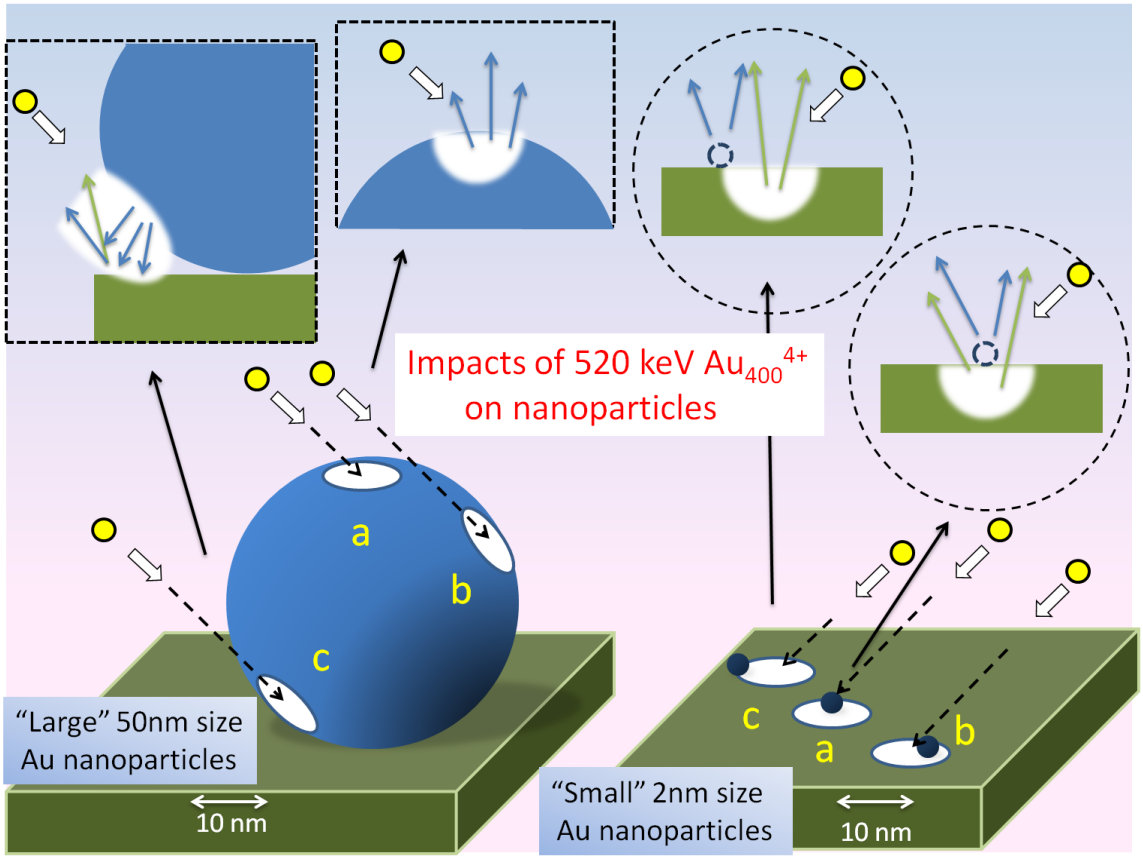

Figure IV–5. Sketch of 520 keV Au_{400}^{4+} impacts on "large" 50 nm NPs (left) and "small" 2nm NPs (right). In the case of 50 nm NP, we consider 3 types of impacts: (a) direct, (b) grazing, (c) interfacial. The statistics of impacts on 2 nm NP are different. This nanoparticle is smaller than the emission area (~10nm), thus the distinction between the three types of impacts is blurred.

and the surface.[70] In the present case, the sputtered species are emitted from an expanding nano-scaled volume caused by the impacting clusters. The ejecta are electronically and vibrationally excited[28] and likely undergo charge exchange processes within the expanding emission volume.[71] The evolution of the latter should be different for different impact parameters. Thus one may expect that the impact parameters affect the ionization probability of NPs. For instance, the mechanism(s) of ionization for direct NP impacts on large (e.g. $\geqq$ 50 nm) size NPs should resemble that on a flat neat surface. In contrast, the emission from a small NP (e.g. $\leqq$ 5 nm) includes ejecta from the substrate which will participate in the charge exchange process. Here the ionization probability will depend on the NP characteristics and the nature of the substrate.

Conclusion

This study is the first experimental documentation of SI yield enhancement from massive projectile impacts on NPs. The optimum sizes for SI emission of ~10 nm and ~20 nm for C_{60} and Au_{400} respectively reflect the more efficient energy transfer inherent in Au_{400}. A detailed description of the ionization process(es) awaits experiments with post-ionization of the emitted neutrals. Our study demonstrates the importance of matching projectile characteristics with target characteristics for maximum SI emission. It emphasizes also that accurate data interpretation from nano-scaled objects requires calibration with "reference" samples of similar size, shape and chemical composition.

CHAPTER V

SIMS METHODOLOGY FOR PROBING THE FATE AND DISPERSION OF CATALYTICALLY ACTIVE MOLECULES*

Introduction

The use of non-precious metal catalysts in fuel cells as a replacement of platinum-based catalysts is of growing interest due to the shortage and cost of platinum.[72,73] Cobalt-based macrocylic molecules loaded on carbon supports have been one of the widely studied materials used for the cell cathode. The catalysts are applied in order to facilitate the oxygen reduction reaction (ORR) at the cathode. In addition to common cobalt-N_4 macrocyclic complexes, cyanocobalamin, i.e. vitamin B12, has been reported as an alternative catalyst for polymer electrolyte fuel cell (PEFC).[74] The catalysts loaded on carbon supports are heat-treated in an inert atmosphere. The heat treatment (pyrolysis) is considered critical to the formation of the catalytically active sites on the carbon supports, where the ORR and electron transfer take place.[75] Thus the performance of the cathode material depends on the nature of the active site, specifically the immediate environment of the central metal determines the pathway and thus the efficiency of the ORR.[73] In this study, we investigated a series of cathode materials consisting of vitamin B12 loaded on carbon black and pyrolized at three different temperatures (500, 700, 900˚C) with time-of-flight secondary ion mass spectrometry (ToF-SIMS). A previous

* This chapter is reprinted with permission from "SIMS Methodology for Probing the Fate and Dispersion of Catalytically Active Molecules" by Liang, C.-K., Chang, S.-T., Verkhoturov, S.V., Chen, L.-C., Chen, K.-H., Schweikert, E.A. *Int. J. Mass Spectrom*. **2014**.

study using X-ray absorption spectroscopy (XAS) has shown that the cobalt in the pyrolized vitamin B12 has a coordination number of 4. Further, the material pyrolized at 700˚C was found to possess the optimal ORR activity.[74] Herein, we apply a unique SIMS methodology to elucidate the local molecular environment of the active site in the presence of carbon black.

The SIMS investigation was conducted using 520 keV Au_{400}^{4+} as projectiles. Massive projectiles at impact velocities of a few tens of km/s feature a high ion multiplicity.[28] The high probability of a projectile impact to cause emission of multiple ions makes it feasible to operate SIMS in the event-by-event-bombardment/detection mode.[31] This approach allows one to selectively compile mass spectra originating from projectile impacts on the active sites despite their dispersion among the carbon black, providing insight into the chemical environment specific to the active sites within an area of diameter ~10 nm.[76] Moreover, the dispersion of the active sites can also be quantified using a methodology developed from this approach.[33] The effect of pyrolysis temperature on the catalysts of the cathode materials will be elucidated in the aspects of the local chemical environment and the dispersion of the active sites.

Experimental

Sample Preparation

The procedure for preparing pyrolized mixtures of vitamin B12 (99%, Aldrich) among carbon black (Vulcan XC-72R, Cabot) has been detailed in ref [74]. Briefly, py-B12/C-500, py-B12/C-700, and py-B12/C-900 are used to represent the samples treated at 500, 700, and 900˚C respectively. For comparison purpose, vitamin B12 pyrolized

alone at 700˚C (py-B12-700), pristine vitamin B12, and pyrolized mixture of Co-corrole loaded on carbon black (py-Co-corrole/C-700)[77] were prepared. All the pyrolized samples were affixed to 1 cm x 1 cm silicon wafer pieces via double-sided copper tapes for ToF-SIMS measurements. Pristine vitamin B12 sample was prepared by electrospraying the dissolved vitamin B12 solution (1 mg/mL in 1:1 MeOH/H_2O) onto a silicon wafer piece.

Results and Discussion

SIMS Investigation of Pyrolysis Effect on Vitamin B12

First, pristine vitamin B12 and py-B12-700 were investigated to examine the effect of pyrolysis on vitamin B12. Figure V-1 shows the mass spectrum of pristine vitamin B12 compared to that of py-B12-700. The appearance of abundant carbon clusters (C_n^-, C_nH^-, and $C_nH_2^-$) in the spectrum of py-B12-700 indicates the vitamin B12 underwent carbonation once heat-treated. A visual confirmation is the change in powder color from maroon to black. The $C_nH_2^-$ clusters are solely present in the spectrum of py-B12-700, while mainly C_n^- and C_nH^- appear in the carbon black spectrum (data not shown). The presence of $C_nH_2^-$ reflects the amorphous structure of the pyrolized vitamin B12 as opposed to the graphite structure of the carbon black.[78] Moreover, in the vitamin B12 spectra a change is observed when comparing the ratio of the secondary ion yield of PO_3^- to that of PO_2^- (Table V-1). The secondary ion yield of PO_3^-, for example, is defined as follows:

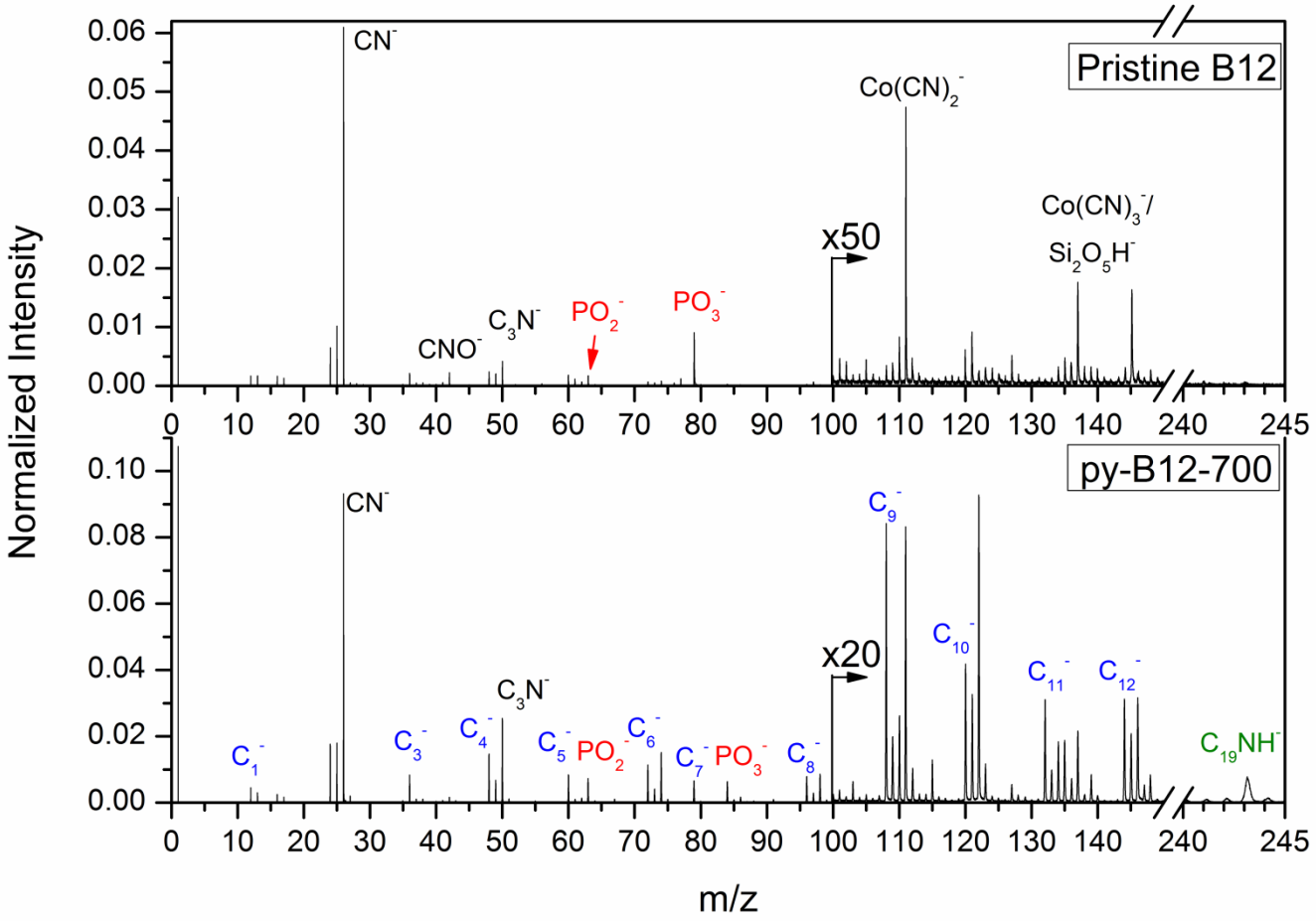

Figure V–1. Negative SI mass spectra of pristine vitamin B12 (top) and py-B12-700 (bottom) impacted with 520 keV Au_{400}^{4+} projectiles.

Table V-1. Ratios of SI yield of PO_3^- to SI yield of PO_2^-.

	Pristine B12	**Py-B12-700**	**Py-B12/C-500**	**Py-B12/C-700**	**Py-B12/C-900**
$Y_{PO_3^-}/Y_{PO_2^-}$	7.0	1.0	1.4	1.2	1.2

Table V-2. Calculated degree of dispersion (D) of the active sites.

	Py-B12/C-500	**Py-B12/C-700**	**Py-B12/C-900**
D	19%	26%	31%

$$Y_{PO_3^-} = \frac{I_{PO_3^-}}{N_{total}} \quad \text{Eq. V-1}$$

where $I_{PO_3^-}$ is the number of the detected PO_3^- in the conventional mass spectrum and N_{total} is the total number of events. The ratio drops approximately 6-fold as vitamin B12 is pyrolized regardless of the temperature and the presence of the carbon black. The decrease in $Y_{PO_3^-}$ is due to the fragmentation associated with P-O bond cleavage due to pyrolysis.

Additionally, a prominent peak at m/z 243 is observed in the spectrum of py-B12-700 but also in those of py-B12/C-700, py-B12/C-900, and py-Co-corrole/C-700 (data not shown). This peak is assigned to $C_{19}NH^-$ considering both vitamin B12 and Co-corrole share a similar 19-carbon macrocyclic structure (Figure V-2**)**. Its presence suggests that pyrolysis results in detachment between the carbon ring and the central Co-N_x moiety, supporting evidence is the absence of m/z 243 in the spectrum of pristine vitamin B12.

SIMS Investigation of Pyrolysis Temperature Effect on Vitamin B12 in the Presence of Carbon Black

In addition to py-B12/C-700, py-B12/C-500 and py-B12/C-900 were analyzed and their mass spectra are compared as shown in Figure V-3 in order to provide an overview regarding the effect of pyrolysis temperature on the catalyst. The effect of high pyrolsis temperature on fragmentation is illustrated with the significant drop in the spectral

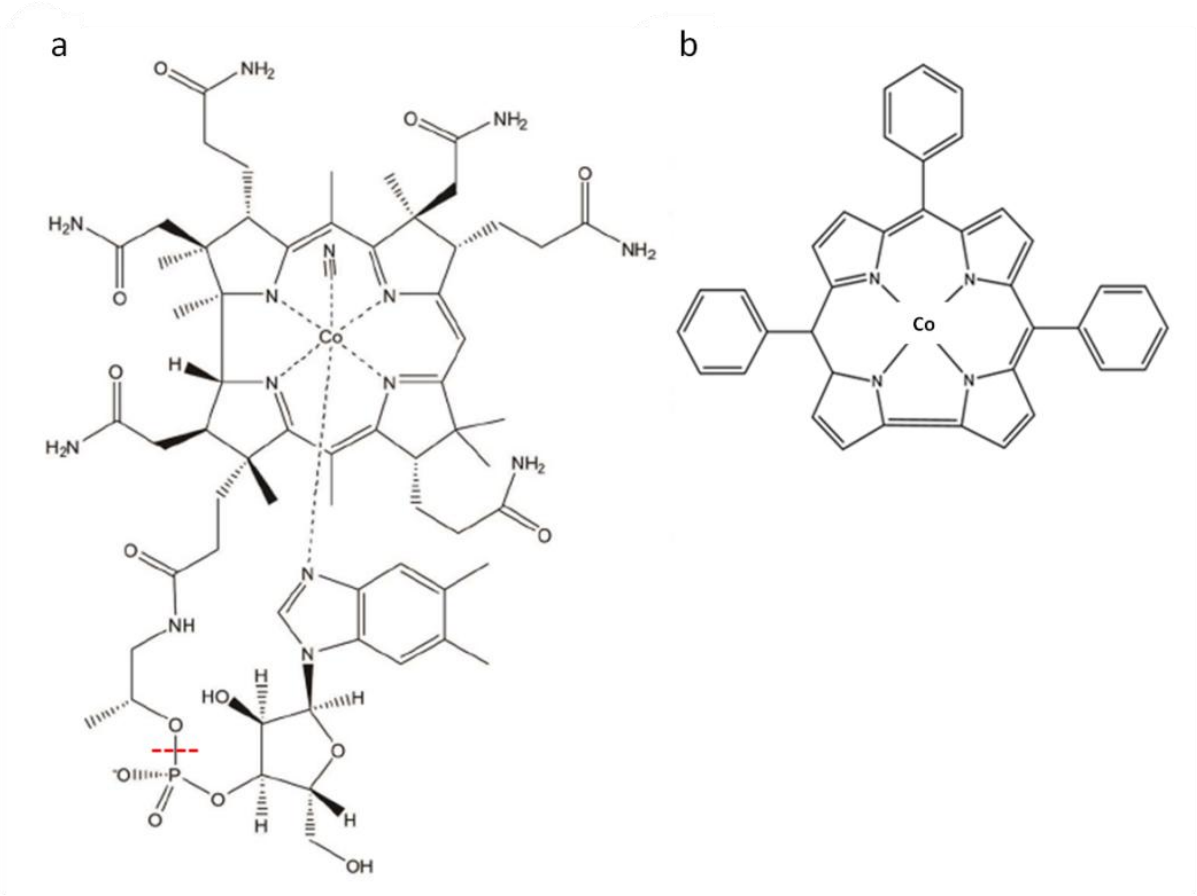

Figure V–2. Structure of (a) vitamin B12 and (b) Co-corrole.

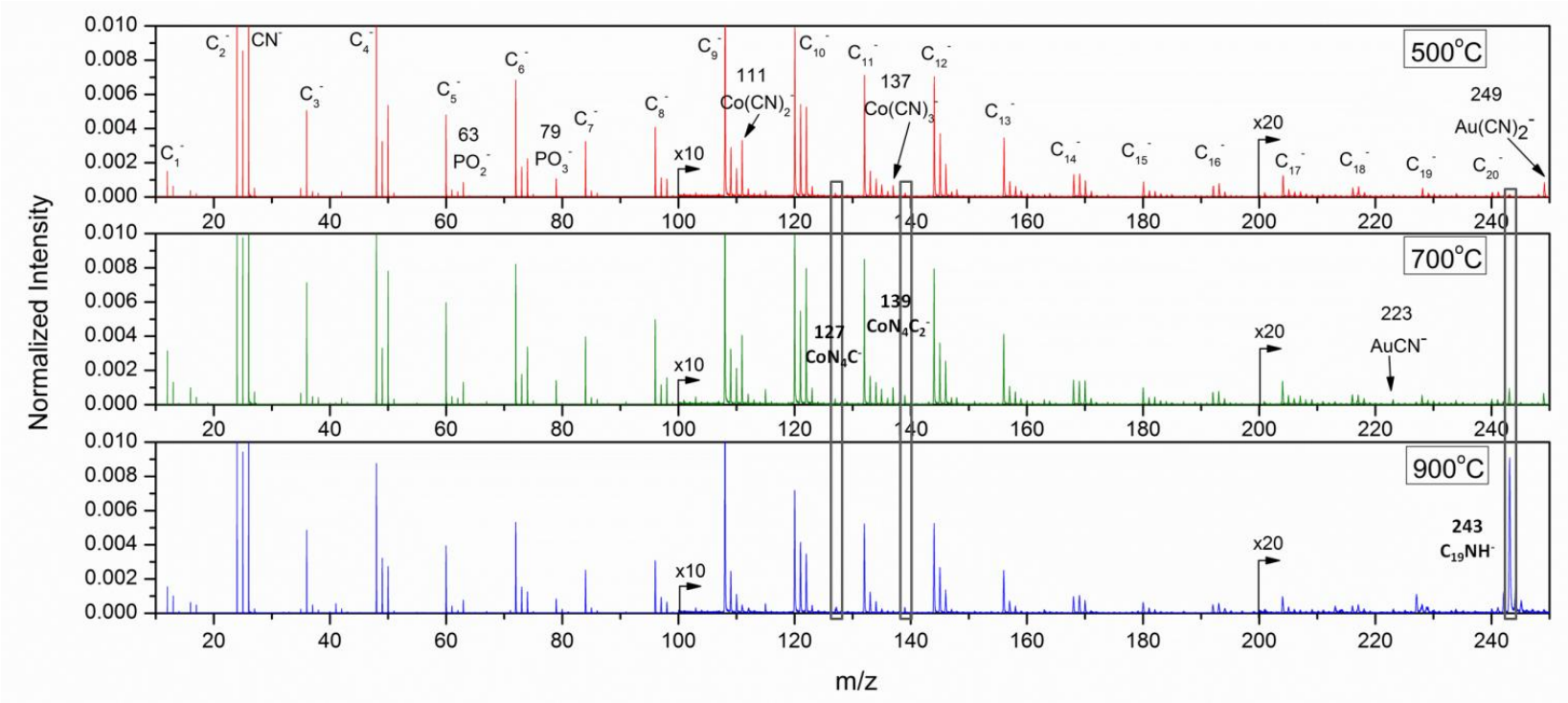

Figure V–3. Negative SI mass spectra of py-B12/C-500 (top), py-B12/C-700 (middle) and py-B12/C-900 (bottom) impacted with 520 keV Au_{400}^{4+} projectiles.

abundance of CN^- particularly in the case of py-B12/C-900. Figure V-4 shows that the secondary ion yield of CN^- for py-B12/C-900 is approximately half that of py-B12/C-500 or py-B12/C-700. It has been reported that catalyst molecules decompose into smaller fragments at pyrolysis temperature above 700˚C.[79] The resulting small fragments desorb readily from the carbon support during pyrolysis at 900˚C, leading to the lower secondary ion yield of CN^-. As a consequence, the yield of gold adduct which involves the combination of CN fragments and gold atoms ablated from the projectiles[61], e.g. $Au(CN)_2^-$ at m/z 249, is suppressed due to the deficiency in CN fragments.

A similar trend to that of the gold adduct is observed for ions at m/z 111 and 137 which are the cobalt adducts $Co(CN)_2^-$ and $Co(CN)_3^-$ respectively. However, these two ions are not considered quantitatively representative of the active sites since their abundance is determined by that of CN fragments instead of the population of the active sites.

In a previous spectroscopic study, a four-coordinated structure of cobalt for pyrolized vitamin B12 was reported and considered responsible for the catalytic activity.[74] In our mass spectral data, fragments containing Co-N_4 moiety are observed for all the samples pyrolyzed at the three different temperatures, including CoN_4C^- and $CoN_4C_2^-$ at m/z 127 and 139 respectively. Moreover, the trend of the secondary ion yields of these fragments coincides with the trend of the ORR performance of the cathodes composed of the pyrolized carbon black supported-vitamin B12 in the order $Y^{700^o}_{CoN_4C_x^-} > Y^{900^o}_{CoN_4C_x^-} > Y^{500^o}_{CoN_4C_x^-}$. Our results confirm that Co-N_4 is the four-coordinated

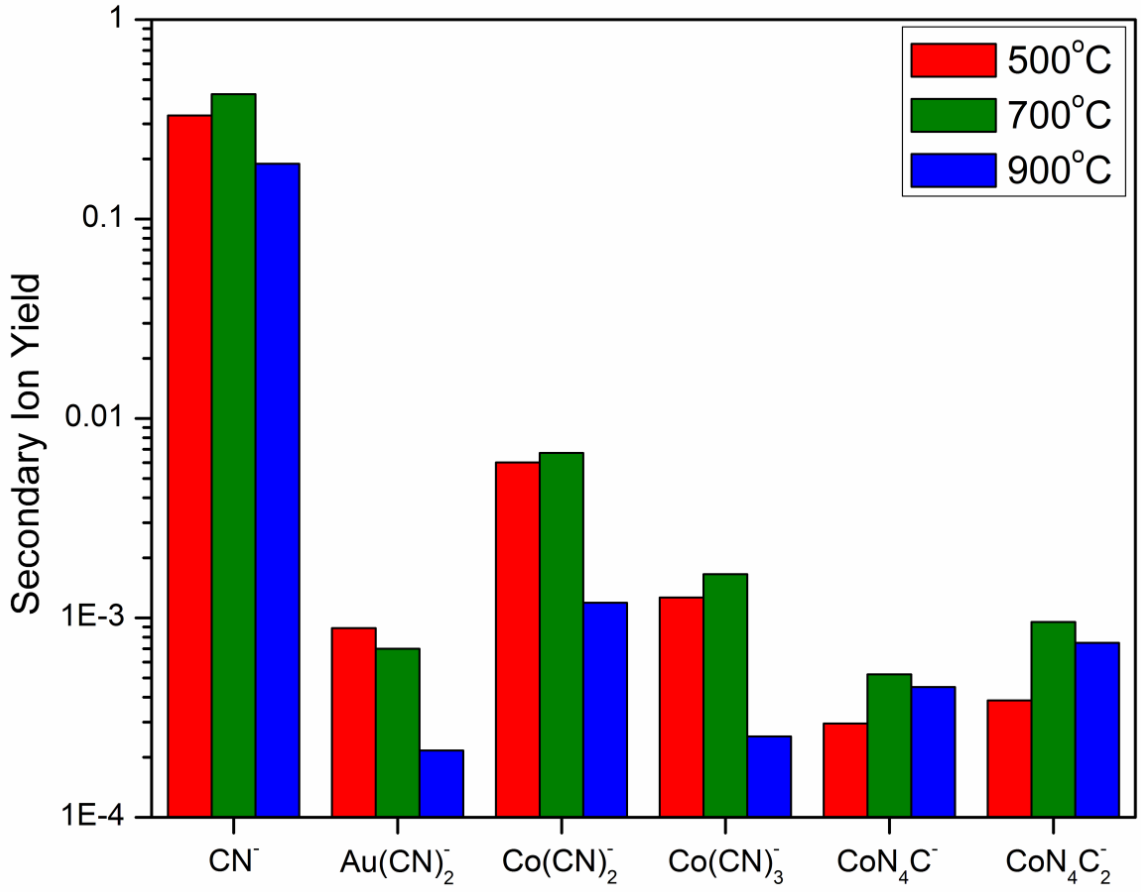

Figure V–4. Secondary ion yields of CN^-, $Au(CN)_2^-$ and cobalt-related ions for samples pyrolized at 500 (red), 700 (green) and 900°C (blue).

moiety retained among the carbon black after pyrolysis and critical to the ORR catalytic activity.

The optimal abundance of the Co-N_4 fragments and hence the optimal ORR performance observed for py-B12/C-700 is illustrated in Figure V-5 with a proposed schematic of the evolution of the active site's formation as a function of pyrolysis temperature. The vitamin B12 molecules are assumed to deposit on the surface of the carbon black as patches of aggregates while mixed with the carbon black, which is nanoparticle-like with diameter of ~30 nm.[80] The aggregates spread out with the increasing temperature so that more vitamin B12 molecules are in contact with the surface of the carbon black to form the active sites shown as the regions in yellow. As noted earlier, $C_{19}NH^-$ appears in the mass spectra for vitamin B12 pyrolized with carbon black at and above 700˚C. Figure V-3 presents the change in spectral abundance of $C_{19}NH^-$ from negligible, moderate to dominant in the spectra corresponding to py-B12/C-500, py-B12/C-700 and py-B12/C-900. It is suggested that the formation of the active sites results from the immobilization of the Co-N_4 moiety via bonding between the macrocyclic carbon ring and the carbon black at 500˚C while the macrocyclic structure remains relatively intact.[81] The marcocylic ring begins to detach from the Co-N_4 moiety at 700˚C, leaving the Co-N_4 moiety bonded itself to the carbon black. However, the active sites can undergo further decomposition when heated at 900˚C, leading to the lower $Y^{900^o}_{CoN_4C_x^-}$ and thus poorer ORR performance.

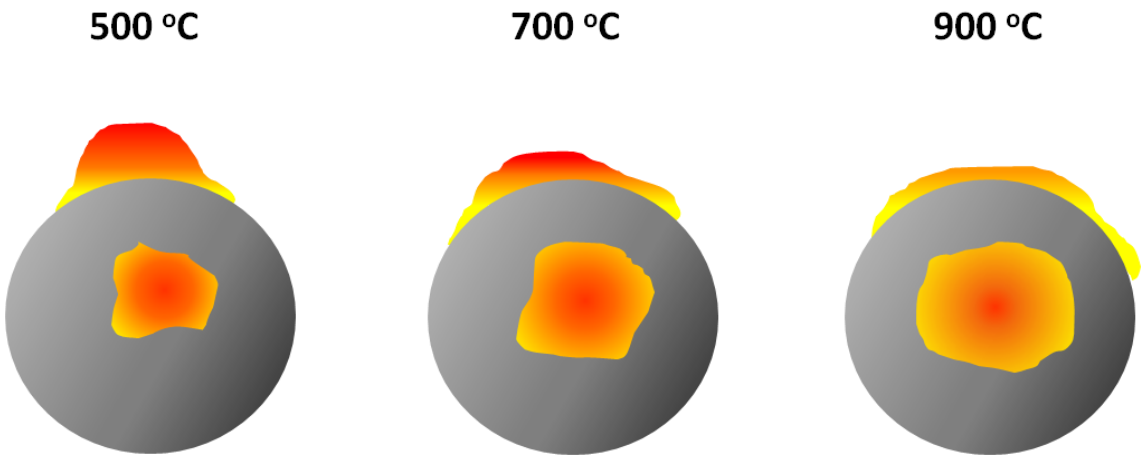

Figure V–5. Schematic illustration of the proposed evolution of the active site's formation as a function of pyrolysis temperature.

Quantitative Analysis of Dispersion of the Active Sites

The spreading of the active site can be confirmed by quantifying its distribution among the carbon black as a function of the pyrolysis temperature. SIMS operating in the event-by-event bombardment/detection mode can determine the factional coverage[33,82] and homogeneity[45,83,84] of a specimen. We apply here this methodology to compute the degree of dispersion of the active sites among the carbon black, one of the important parameters governing the performance of the fuel cell. The degree of dispersion, D, is defined as follows:

$$D = \frac{K_{cobalt}}{K_{carbon}} \quad \text{Eq. V-2}$$

where K_{cobalt} and K_{carbon} are the fractional coverages of the catalyst and carbon support respectively.

The calculation of the fractional coverage necessitates two ions, e.g. A and B, characteristic of a specimen of interest assuming the two ions are emitted independently. This relationship can be expressed by[56]:

$$Y_{A,B} = Y_A \cdot Y_B \quad \text{Eq. V-3}$$

where $Y_{A,B}$ is the coincidental SI yield of simultaneously detected ions A and B. Y_A and Y_B are the secondary ion yields of detected ions A and B respectively.

Eq. V-3 can be rewritten as follows:

$$\frac{I_{A,B}}{N_{eff}} = \frac{I_A}{N_{eff}} \cdot \frac{I_B}{N_{eff}} \quad \text{Eq. V-4}$$

where $I_{A,B}$ is the detected number of co-emitted A and B in the coincidental mass spectrum, I_A is the number of A in the conventional mass spectrum while I_B is the number of B. N_{eff} is the number of effective impacts for emissions of A and B.

The fractional coverage (K) of the specimen, defined as the ratio of the number of effective impacts (N_{eff}) to the total number of impacts (N_{total}), can thus be obtained by rearranging Eq. V-4:

$$K = \frac{N_{eff}}{N_{total}} = \frac{I_A \cdot I_B}{I_{A,B} \cdot N_{total}} \quad \text{Eq. V-5}$$

Table V-2 outlines the degree of dispersion of the active sites for py-B12/C-500, py-B12/C-700 and py-B12/C-900, where $K_{catalyst}$ and K_{carbon} are computed with CoN_4C^-, $CoN_4C_2^-$ and C_7^-, C_8^- respectively. The results show the active sites' degree of dispersion increases by approximately 5% for every increment of 200˚C. Given that the catalysts were mixed throughout the carbon black homogeneously when the three samples were prepared, the observed increase in dispersion supports the suggestion that increasing pyrolysis temperature facilitates the spreading of the vitamin B12 aggregates to form the active sites on the carbon black.

Coincidental Mass Spectral Study on Local Molecular Environment of the Active Sites

Compiling the mass spectra selected from the projectile impacts on the active sites offers a snapshot of the local molecular environment of the active sites. The coincidental mass spectra of py-B12/C-500, py-B12/C700 and py-B12/C-900 can thus help understand the fate of the vitamin B12 molecules as a function of pyrolysis temperature. Figure V-6 presents the three samples' coincidental mass spectra composed of secondary

ions co-emitted with $Co(CN)_2^-$ (m/z 111), denoted as "co-111" mass spectra for brevity. All the coincidental mass spectra are presented in the format where the ion intensities are normalized to their corresponding numbers of the selected events. They represent the local molecular environment of the active sites within a nanovolume of ~10^3 nm^3. The co-111 mass spectrum of py-B12/C-500 resembles that of py-B12/C-700 in terms of the abundance of CN^- and $C_nH_2^-$, while these fragments are less distinct for py-B12/C-900. The reduction of $C_nH_2^-$ suggests the change in morphology of the pyrolyzed product of vitamin B12 from amorphous to graphite-like structure due to the high pyrolysis temperature (900˚C). In addition, some fragments relevant to the ribose moiety are identified since their abundance is enhanced in the co-111 mass spectrum of py-B12/C-500 as compared to the corresponding conventional mass spectrum (Figure V-3), including ions at m/z 122, 148, 164, 185, 201 and 207. Their appearance in the coincidental mass spectrum indicates the ribose moiety is preserved and locates within the active sites at low pyrolysis temperature. However, the ribose fragments are less prominent in the co-111 mass spectrum of py-B12/C-700 and even negligible for py-B12/C-900.

It is noteworthy that, in the conventional mass spectra, the secondary ion yields of PO_2^- and PO_3^- vary as a function of pyrolysis temperature in the order $Y_{PO_x^-}^{700^o} > Y_{PO_x^-}^{500^o} > Y_{PO_x^-}^{900^o}$ as opposed to the order ${}^{C}Y_{PO_x^-}^{500^o} > {}^{C}Y_{PO_x^-}^{700^o} > {}^{C}Y_{PO_x^-}^{900^o}$ observed in the co-111 mass spectra, where ${}^{C}Y_{PO_x^-}$ is the yield computed by dividing the number of detected PO_x^- in the coincidental mass spectrum by the number of the selected events. The

decreasing PO_x^- as well as the ribose fragments in the co-111 mass spectra of py-B12/C-700 and py-B12/C-900 suggest the PO_x-ribose moiety dissociates partially from the active sites during pyrolysis at 700˚C, the trend is significant at 900˚C. The latter can be further supported by the coincidental mass spectrum composed of secondary ions co-emitted with PO_3^-, denoted as "co-79" mass spectrum (Figure V-7). Unlike py-B12/C-500 and py-B12/C-700, whose co-79 mass spectra resemble their co-111 mass spectra, the co-79 mass spectrum of py-B12/C-900 differs from its co-111 mass spectrum. The relative abundance of CN^- vs. PO_2^- is significantly different between the two spectra. The PO_x-ribose fragments are present only in the co-79 mass spectrum. These differences indicate the ribose moiety and the active site possess a different local chemical environment for py-B12/C-900, implying that the ribose moiety co-localizes within the active sites at low pyrolysis temperature whereas they dissociate from each other at high pyrolysis temperature. The dissociation concurs with the P-O bond cleavage as discussed previously, with the cleavage likely occurring at the position labeled in Figure V-2. We attribute the dissociation to desorption/adsorption of the disconnected PO_x-ribose moiety during pyrolysis whereas the Co-N_4 moiety is anchored on the surface of the carbon black. Interestingly, the two ions at m/z 138 and 154 are enhanced in the co-79 mass spectrum of py-B12/C-900 solely and assigned $CoPO_3^-$ and $CoPO_4^-$ respectively. The cobalt adducts formed with PO_x fragments arise from

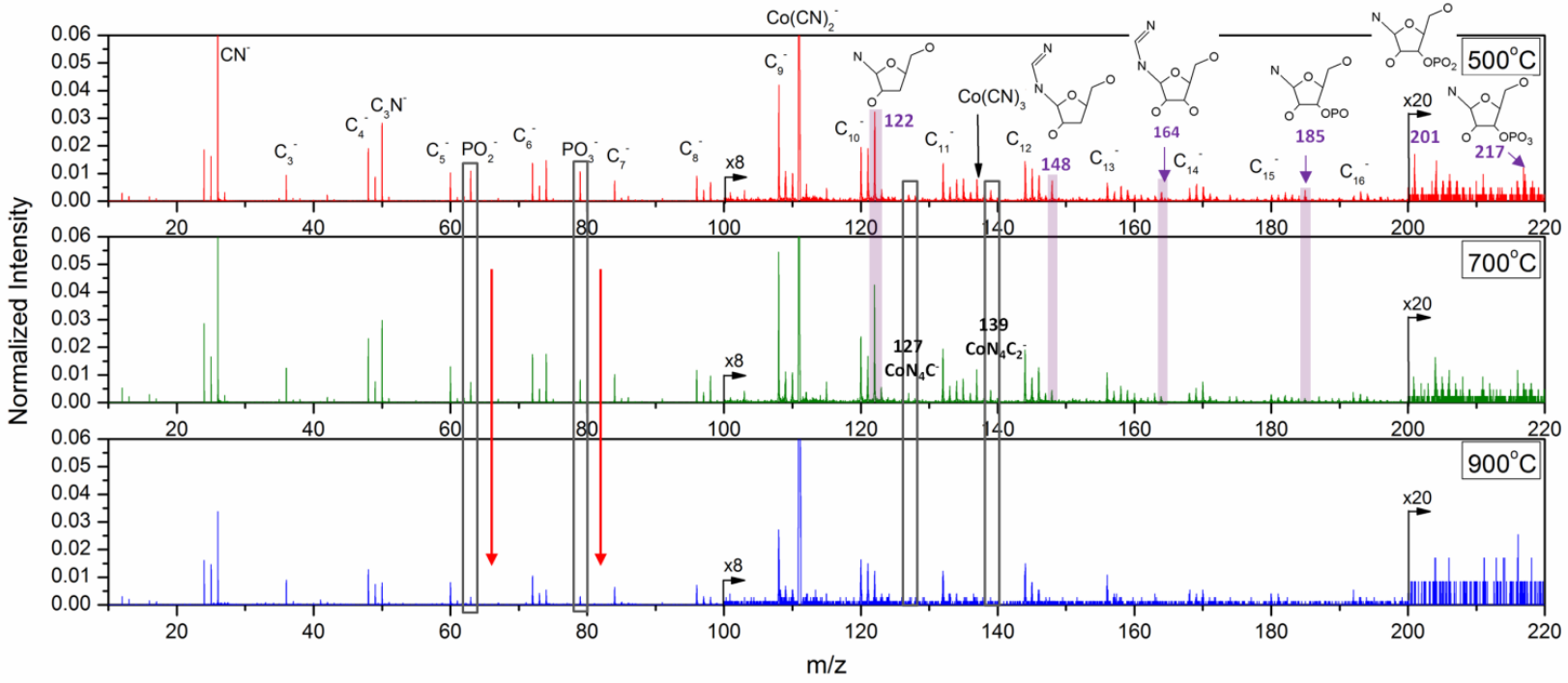

Figure V–6. Coincidental mass spectra of co-emitted ions with $Co(CN)_2^-$ (m/z 111) for samples pyrolized at 500 (top), 700 (middle) and 900°C (bottom).

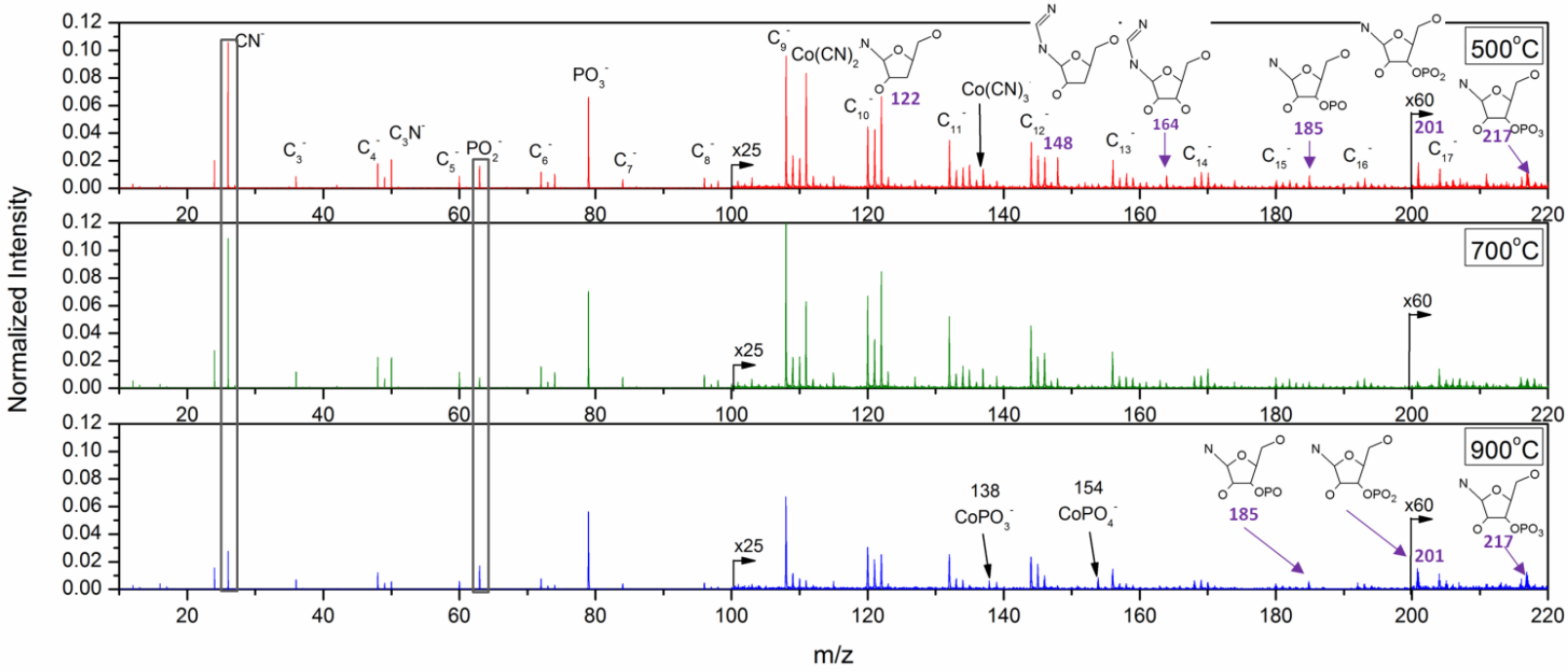

Figure V–7. Coincidental mass spectra of co-emitted ions with PO_3^- (m/z 79) for samples pyrolized at 500 (top), 700 (middle) and 900°C (bottom).

projectile impacts on the regions where the extent of the dissociation between the PO_x-ribose and Co-N_4 moieties is smaller than the interaction volume of the Au_{400} impact (~10 nm in diameter) and where the local abundance of PO_x fragments outweighs that of CN fragments.

Conclusion

This study demonstrates the capability of the 520 keV Au_{400} SIMS in the event-by-event bombardment/detection mode to probe the fate of the pyrolized catalyst dispersed among the carbon support. The observation of $CoN_4C_x^-$ coincides with the previous XAS results, confirming that the Co-N_4 moiety is the structure responsible for the active sites. The local molecular environment of the active sites within ~10 nm can be obtained from the associated coincidental mass spectra. The PO_x-ribose moiety is found to dissociate from the active sites as a consequence of high pyrolysis temperature. The concept of fractional coverage derived from the coincidental methodology can be further applied to quantify the active site's degree of dispersion, providing additional information on homogeneity useful for material characterization.

CHAPTER VI

NEW SIMS APPROACH FOR SMALL NANOPARTICLE CHARACTERIZATION

Introduction

Nanoparticles have garnered great attention due to their inherently novel properties resulting from a high surface-area-to-volume ratio,[85,86,87] which is inversely proportional to the radius for spherical particles. Given the high surface-area-to-volume ratio, their properties, e.g. solubility, toxicity, optical, electrical, and catalytic characteristics, can be altered by modifying their surfaces.[88,89,90] Small nanoparticles, referred here to those smaller than 10 nm in diameter, are of special interest because at those sizes pronounced changes in chemical reactivity can occur.[91,92] Therefore, compositional characterization is essential to understanding the properties of native or engineered nanoparticles. Several surface analytical techniques have been applied in nanoparticle characterization.[2,7] Secondary ion mass spectrometry (SIMS) is one of the few suitable for molecular analysis. Small nanoparticles impose challenges for their characterization, including a finite amount of material available for analysis and a sampling volume larger than the object at least in one dimension. The former can cause low sensitivity and the latter can lead to inaccurate analysis and possibly erroneous interpretation on the properties due to interference from the particle's environment. Indeed, the study discussed in Chapter IV led to the first observation of size-dependent SI yields of NP-related ions (Au_n^-). Their emission was also accompanied by substrate-related ions. Herein, we aim to advance the

molecular characterization capability of SIMS for small nanoparticles (≦10 nm). The directions for advancement are two-fold: 1) to exploit the key feature of massive projectiles, specifically Au_{400}^{4+} at hypervelocity, for production of multiple secondary ions,[28] and 2) to examine the objects in the (conventional) backward and forward *transmission* modes simultaneously to gather a maximum of information. The emission of multiple secondary ions makes it practical to operate in the event-by-event bombardment/detection mode, as described in Chapter II. The former can also enhance the sensitivity for objects of finite materials. Moreover, the small nanoparticles will likely shatter upon bombardment and the secondary ions will emit preferably in the forward direction by virtue of momentum transfer. Molecular dynamics (MD) simulations have predicted enhancement in forward emission.[93] An experiment with carbon foils has shown enhanced and mass-shifted SI emission.[76] Therefore, the transmission mode, termed here "transmission-SIMS", should be advantageous for small nanoparticles. The prerequisite associated with this approach is utilization of a substrate thin enough for projectile to penetrate and transfer energy to the objects deposited on it. Graphene sheets of few layers meet the requirement as the support for the small nanoparticles considering their atomic thickness unlikely to skew the compositional signature of the nanoparticles. This chapter will present the feasibility of this approach for small nanoparticle analysis, which was tested with 5 nm dodecanethiol-capped AuNPs deposited on graphene sheets supported by TEM copper grids. Such supporting substrates also allow one to conduct TEM, SEM, and SIMS examinations with the same sample.

Experimental

Sample Preparation

Amorphous carbon foils of 1.1 and 2.0 μg/cm^2 (Arizona Carbon Foil Company, Tucson, AZ) were mounted on 81% transmission nickel grids (Precision Eforming, Cortland, NY) using the method described elsewhere.[76] The corresponding thickness was measured as 5 and 10 nm respectively by the supplier using Rutherford Backscattering. Graphene sheets-covered TEM grids were purchased from two suppliers. Graphene sheets of 1, 2, and 3-5 layers deposited on lacey carbon/300 mesh Cu grids were received from Ted Pella Inc. (Redding, CA) and denoted as 1L-, 2L-, and 3-5L-graphene respectively. Graphene sheets of 1-6 layers deposited on 2000 mesh Cu girds were obtained from Graphene Supermarket (Calverton, NY) and denoted as 1-6L-graphene.

The 5 nm dodecanethiol-capped AuNPs were purchased from Nanoprobes Inc. (Yaphank, NY). The stock was dissolved in hexane to a concentration of 8 mg/mL when received. The AuNPs solution was further diluted to 0.8 mg/mL and 10 μL of the diluted solution was drop-casted onto the 1-6L-graphene for electron microscopic and mass spectral investigations.

Instrumentation

The mass spectral investigation of the graphene samples was conducted in the second analysis chamber which consists of two linear ToF legs in a diagonal arrangement (Figure VI-1). By moving the sample dock in the first analysis chamber out of the beamline, the projectiles emitted from the Pegase platform can reach the second

chamber by passing through a transfer tube between the chambers. A high voltage Einzel lens is mounted in the tube, refocusing the beam through an aperture (Ø 5 mm) set at the entrance of the second chamber.

A photograph of the experimental setup inside the chamber is presented in Figure VI-2. The configuration can be varied by rotating the chamber to obtain any incident angle of the projectile beam with respect to the normal of the target surface. An incident angle of 30˚ was adopted while the two ToF legs aligned with the target surface's normal for the experiments performed in this chapter. The sample holder consists of a pair of stainless steel plates with an aperture of 3 mm in diameter on each. The graphene samples were sandwiched and affixed concentrically with the apertures. The sample holder is mounted on a positioner in a horizontal direction and biased (±10 kV). Two grounded extraction Ni grids (90% transmission, Precision Eforming, Cortland. NY) are placed 12.6 mm away from both sides of the sample. The arrangement of the signal detection systems is the same for both sides. The stop detector is positioned 60 cm away from the target and consists of a pair of MCPs in chevron assembly followed by an eight-anode detector. A grounded grid is placed in front of the MCPs to define the field-free drift region for the secondary ions. The start detector consisting of chevron-assembled MCPs and a single anode is branched out above the beam axis of ~30˚. An external electromagnet is used to deflect the ejected electrons or protons to the start detector, triggering the ToF measurements for negative or positive ion analysis respectively. The trajectory of the secondary ions can be adjusted with a set of vertical/horizontal deflectors placed behind the extraction grid. For the presentation and

discussion of the results, the SIs ejected back in the direction of the incoming projectiles are designated as “reflection” emission and those ejected in the opposite direction (where the projectiles exit the samples) as ”transmission” emission.

Data Acquisition

The start and stop signals on each side can be transmitted to their respective CFDs and TDCs, creating conventional mass spectra independently of each side as described in Chapter II. For the experiments presented in this chapter, however, the post-CFD start signals from both sides were fed into a coincidence module (465 triple 4-fold logic unit, Teledyne LeCroy, Chestnut Ridge, NY). Upon recognition as synchronized by the module, the two signals were selected to generate an output to start the TDCs for both sides, termed “synchronized start” in this dissertation. (Figure VI-3) This selection permitted the transmission and reflection mass spectra were collected from an accumulation of events originating from identical projectile impacts on the sample.

SEM Examination

Scanning electron microscope (SEM, Jeol-7500 Cold Field Emission) operating in secondary electron mode with higher accelerating voltage (5.0 kV) and working distance (8.0 mm) was used to examine the quality of the graphene samples prior to the mass spectral investigation. Lower energy electron beam (1.0 kV) with shorter working distance (3.0 nm) was selected to visualize the holes resulting from the Au_{400} bombardments on the graphene sheets.

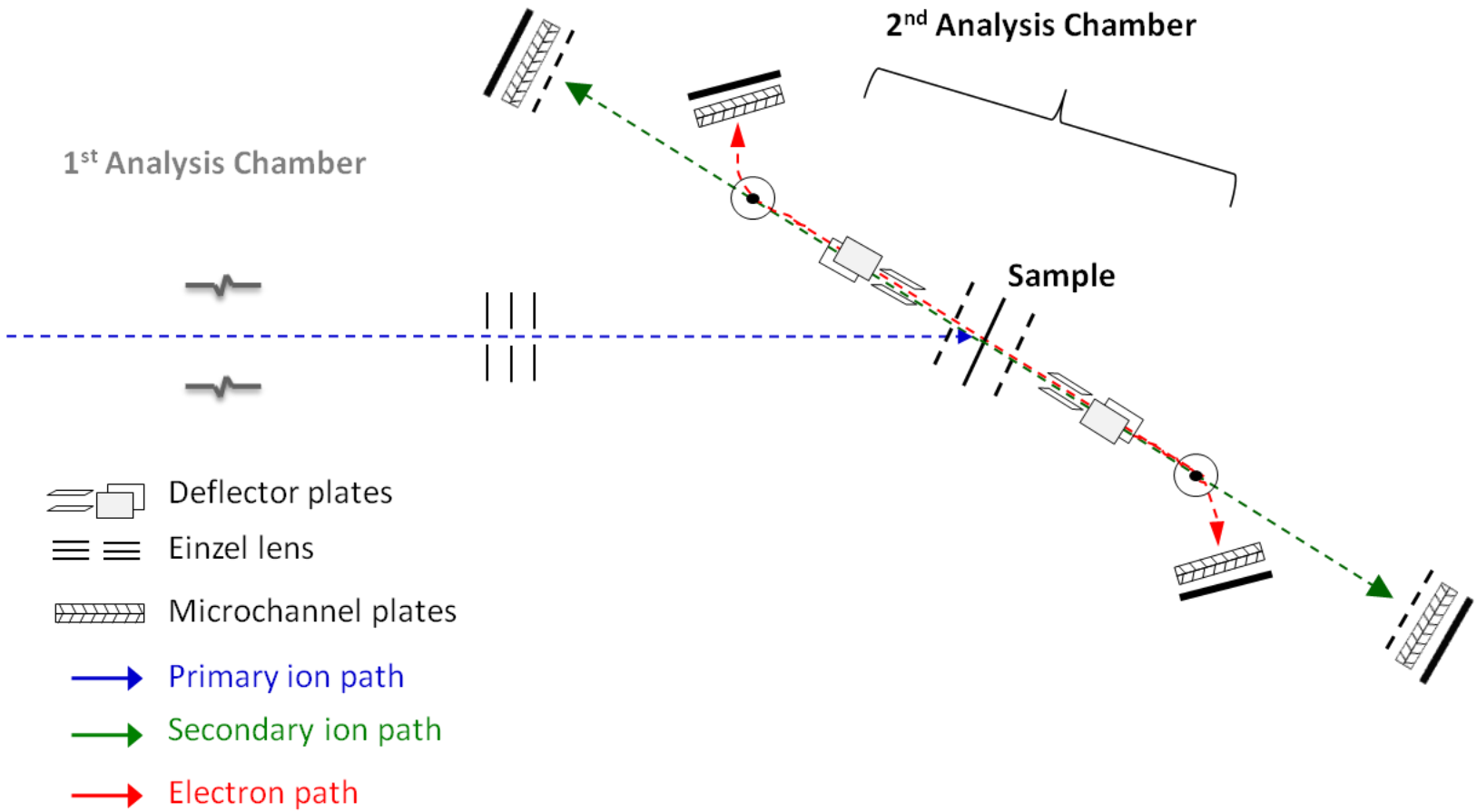

Figure VI–1. Schematic overview of the 2nd analysis chamber coupled to the custom Au-LMIS ToF-SIMS instrument.

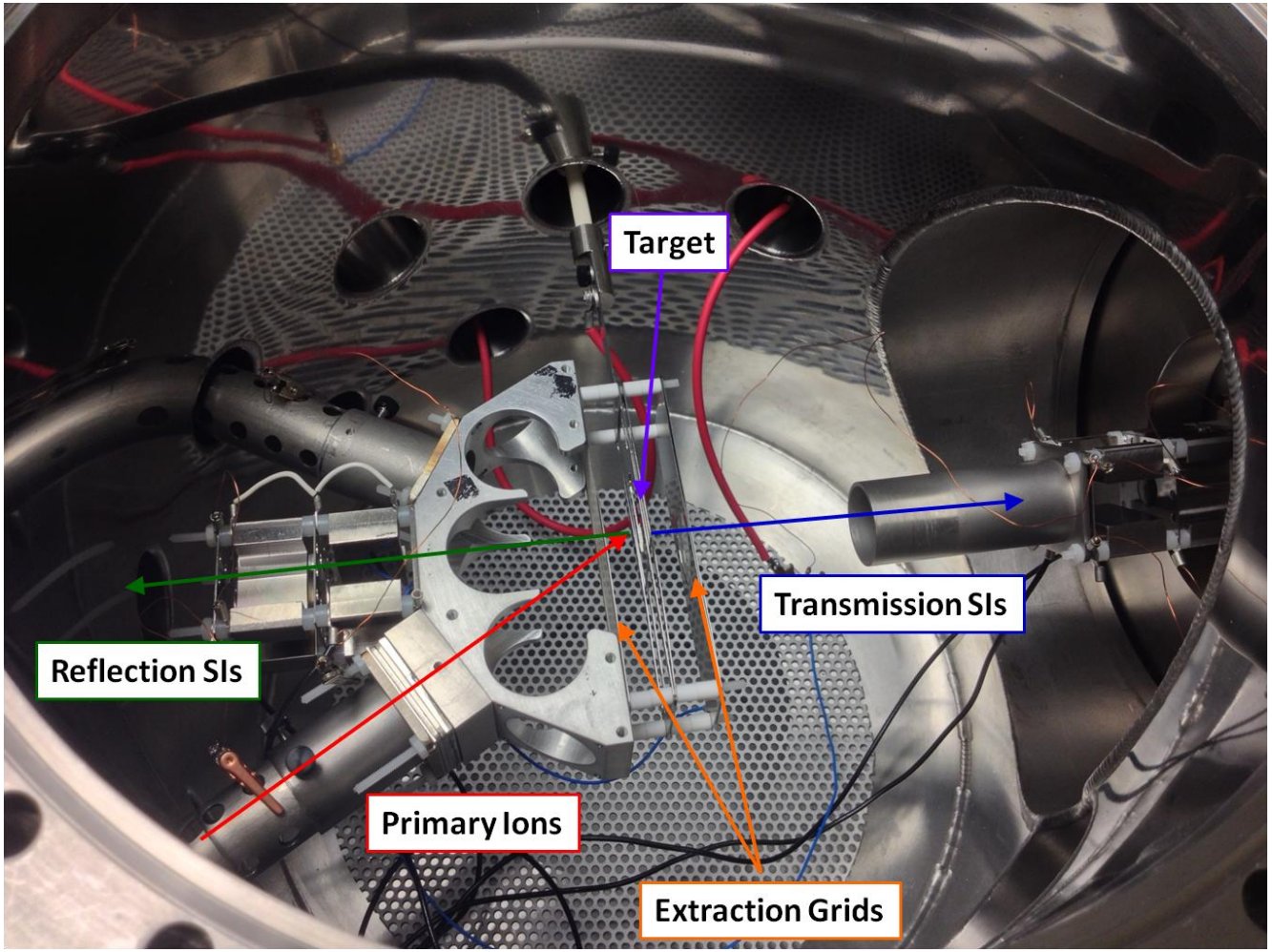

Figure VI–2. Photograph of the experimental setup inside the 2nd analysis chamber.

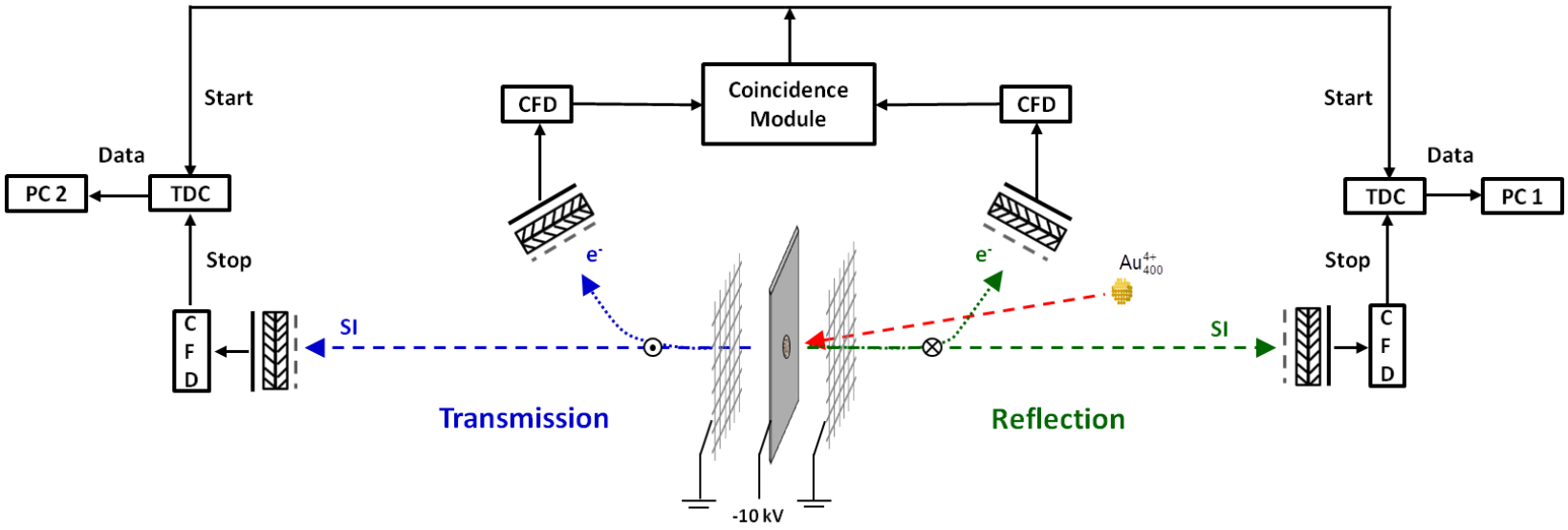

Figure VI–3. Pictorial depiction of the synchronized electron start for registering simultaneously bi-directional ejecta.

TEM Examination

The 1L-, 2L-, and 3-5L-graphene sheets were examined with transmission electron microscope (TEM, FEI Tecnai G^2 F20 FE-TEM) after the mass spectral investigation. The images of the impacted regions were obtained with 120 or 200 keV electrons incident normal to the graphene surface.

Results and Discussion

Investigation of Graphene Substrate

We first investigated the graphene sheets alone in order to identify mass spectral signals characteristic of the graphene sheets and to understand the effect of thickness on the ion emission. The samples were also post-examined with electron microscopes to provide verification of projectile impacts on the atomically thin film.

SEM results

According to the supplier (Ted Pella), the graphene sheets were prepared by chemical vapor deposition of graphene of a give number of layers onto copper foils. The graphene was next released by etching the foil and subsequently transferred onto a lacey carbon-covered 300 mesh Cu TEM grid. Therefore, the coverage of the graphene sheets among the grid depends on the quality of the lacy carbon network which supports the graphene. The scanning electron micrograph in Figure VI-4a shows an overview of the 1L-graphene sample, where the single sheet of graphene is visible under SEM as the region shown in light grey whereas the darker window corresponds to the region which is covered by neither the lacey carbon and thus nor graphene. In general, the usable area is approximately 75%. Moreover, there are particles of few hundred nm in diameter

present on the graphene sheets (Figure VI-4c,d). They are the copper/copper chloride particles which are the side products during the manufacturing process.

After the mass spectral investigation, the graphene was post-examined with SEM. SEM operating in lower accelerating voltage and shorter working distance enabled us to visualize holes resulting from individual Au_{400} projectile impacts. Figure VI-5a shows a region containing a patch where the network structure of the lacey carbon was not formed completely on the 1L-graphene. The presence of black dots suggests the peripheral of the patch is thin enough for the Au_{400} projectiles to penetrate. The holes are also visible on the free-standing graphene sheet with a diameter of approximately 10 nm (Figure VI-5b). The accurate assessment on the hole size, however, necessitates measurements with a higher spatial resolution, e.g. transmission electron microscope (TEM). All the observations mentioned above also hold for the 2L- and 3-5L-graphene samples.

TEM results with hole distribution

An area bombarded by Au_{400} projectiles is shown in Figure VI-6 where the hollow and circular features represent the impact-resulting holes, whereas a hole with a larger dimension (labeled as ★) is considered due to a defect in manufacturing process. The black dots are the copper/copper chloride particles of 2-3 nm in diameter, which are too small to be detected with SEM. In addition to the circular holes, a petal-like feature is also observed surrounding most of the holes. To verify whether this feature is hollow or not, the energy of the electron beam must be reduced to an energy below that required to kick out carbon atoms from the graphene lattice (140 keV).[94] Figure VI-7 presents a

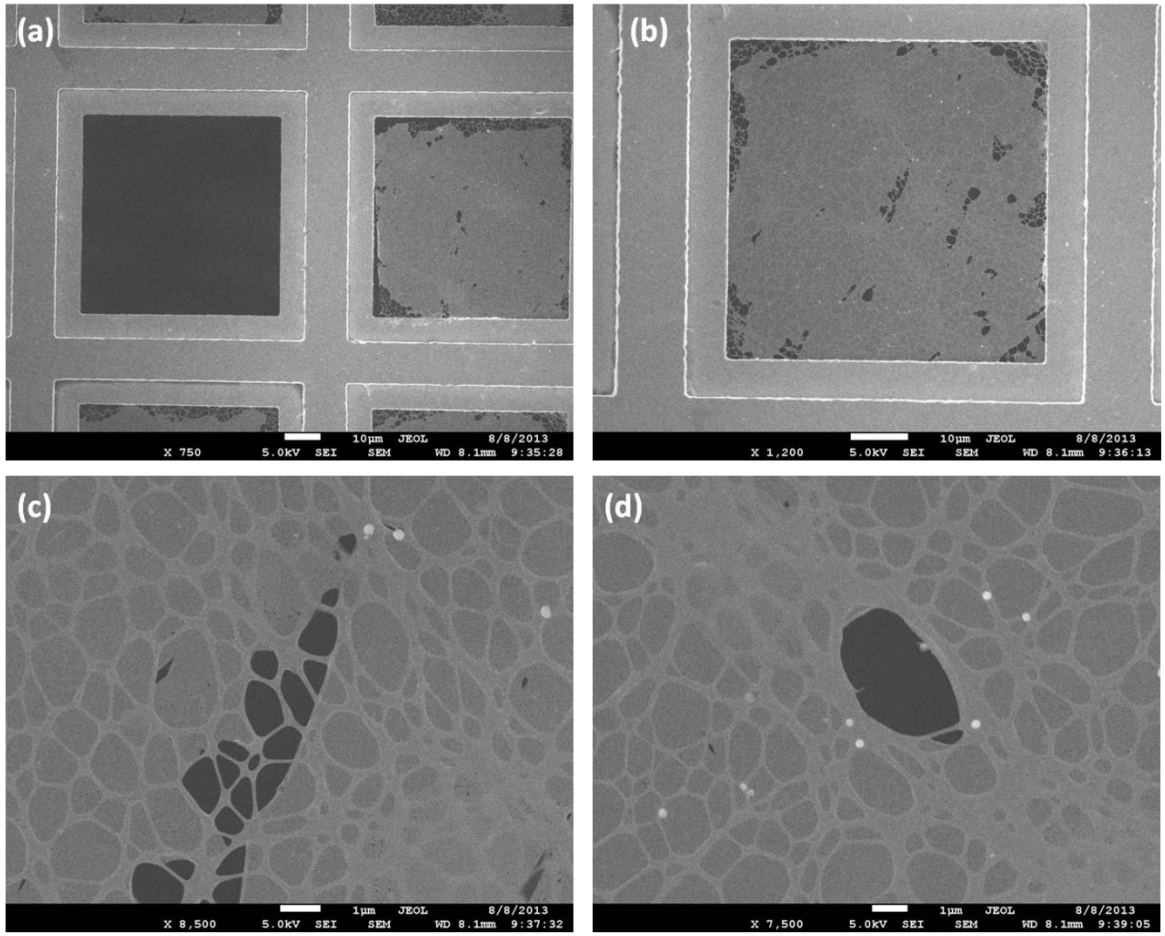

Figure VI–4. SEM micrographs of 1L-graphene prior to Au_{400}-SIMS investigation (working distance= 8.1 mm, accelerating voltage= 5.0 kV). Scale bar: 10 µm for (a), (b) and 1µm for (c), (d).

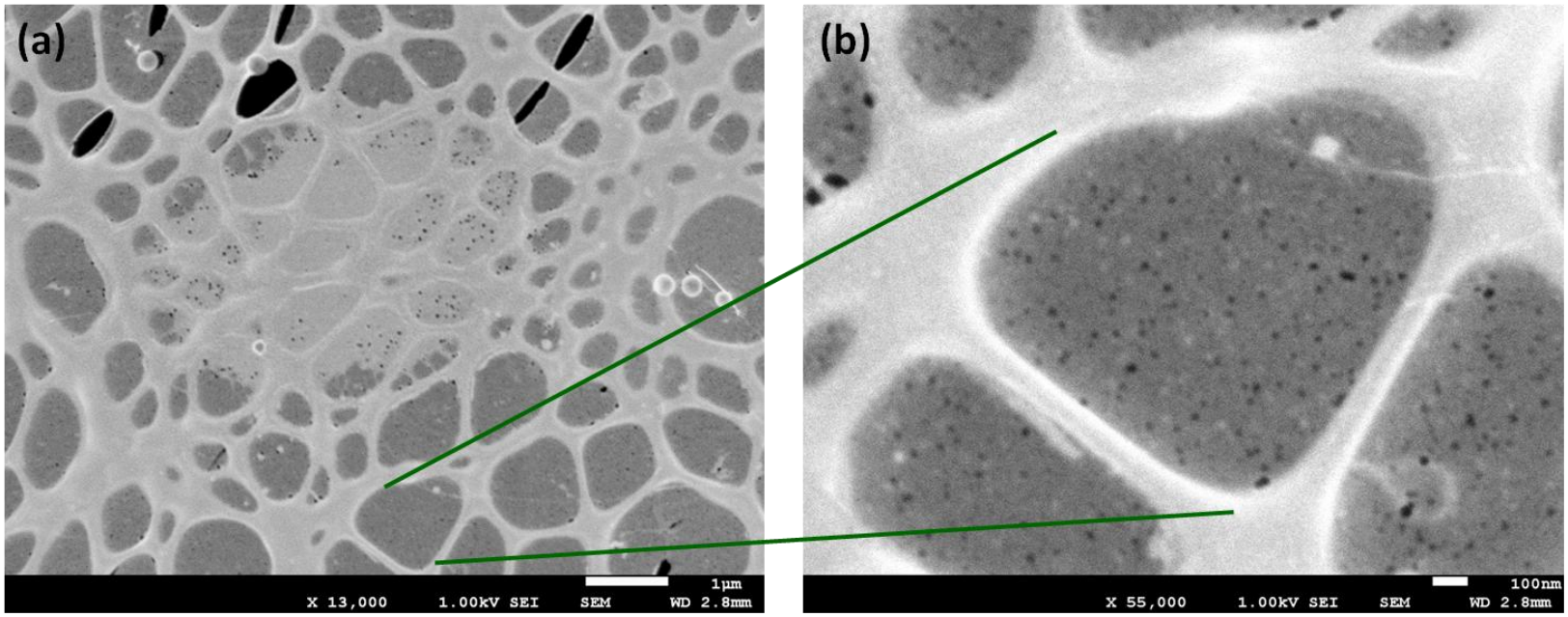

Figure VI–5. SEM micrographs of 1L-graphene bombarded by 520 keV Au_{400}^{4+} impacts (working distance= 2.8 mm, accelerating voltage= 1.0 kV). Scale bar: 1 µm for (a) and 100 nm for (b).

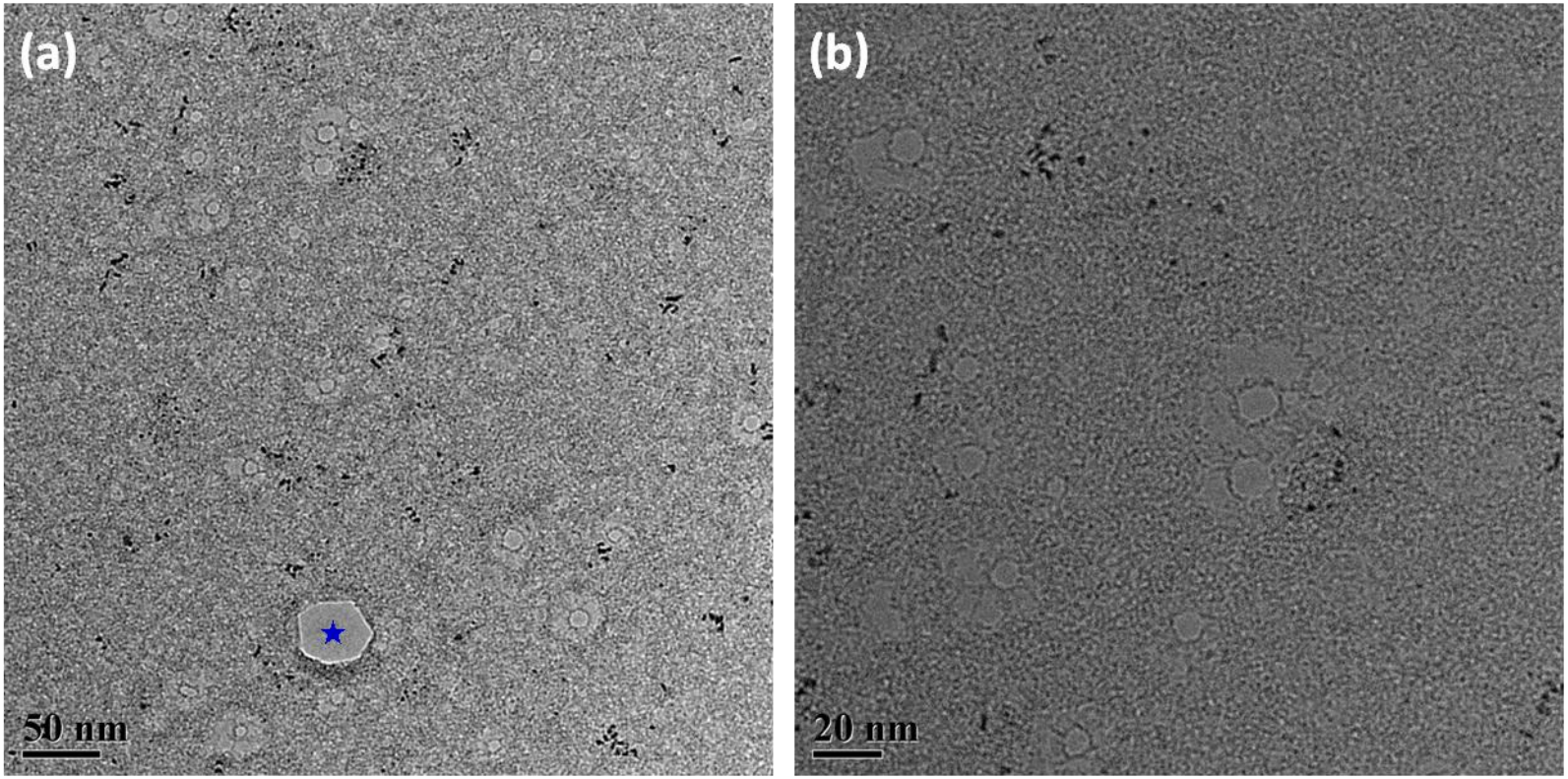

Figure VI–6. TEM micrographs of 1L-graphene bombarded by 520 keV Au_{400}^{4+} impacts (electron beam energy= 200 keV).

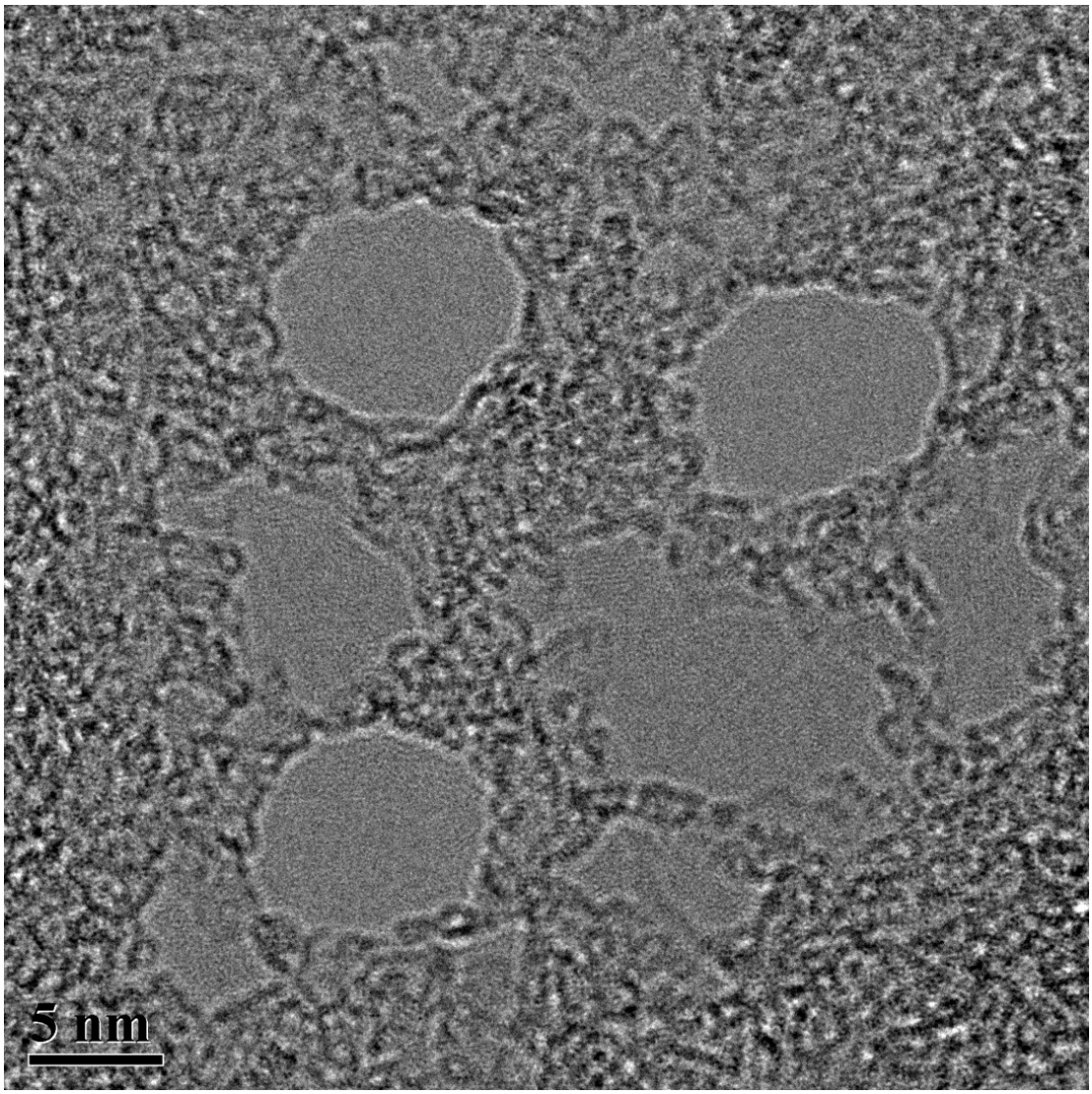

Figure VI–7. TEM micrographs of the 1L-graphene bombarded by 520 keV Au_{400}^{4+} impacts (electron beam energy= 120 keV).

close-up of the features associated with holes irradiated by a 120 keV electron beam. A lattice structure is observed within the petal-like region while clear of structure within the holes. The mechanism responsible for this feature is unknown.

With the TEM images, the statistics on hole size were obtained by measuring the diameters from an ensemble of several tens of holes, given in Figure VI-8. For comparison purposes, the average diameter of the holes on a 5-nm carbon foil target from a previous study[76] is also included. The results show that the average diameters are 9.0±1.8, 9.2±2.1, 7.5±1.6, and 15.4±2.9 nm for 1L-, 2L-, 3-5L-graphene, and 5-nm carbon foil respectively.

Mass spectral analysis

Effect of Supporting Materials

The rationale for applying the synchronized start is to ensure that the data collected on both sides originate from the same projectile impacts. The main advantage of this operational condition is that the recording of the events where projectiles impact on the supporting materials (e.g. lacey carbon and grid) is minimized due to the fact that the supporting materials are too thick for the projectile impacts to produce secondary species in the transmission direction. The preceding statement can be supported by comparing the extent of correlation between the transmission and reflection electrons with a lacey carbon-covered Cu gird to that with one covered by graphene. The extent of correlation was tested in the negative ion mode by feeding the post-CFD reflection start signals into one of the stop inputs of the TDC used for the transmission side through a delay cable while time-registering the transmission ejecta from the remaining 7 inputs triggered by

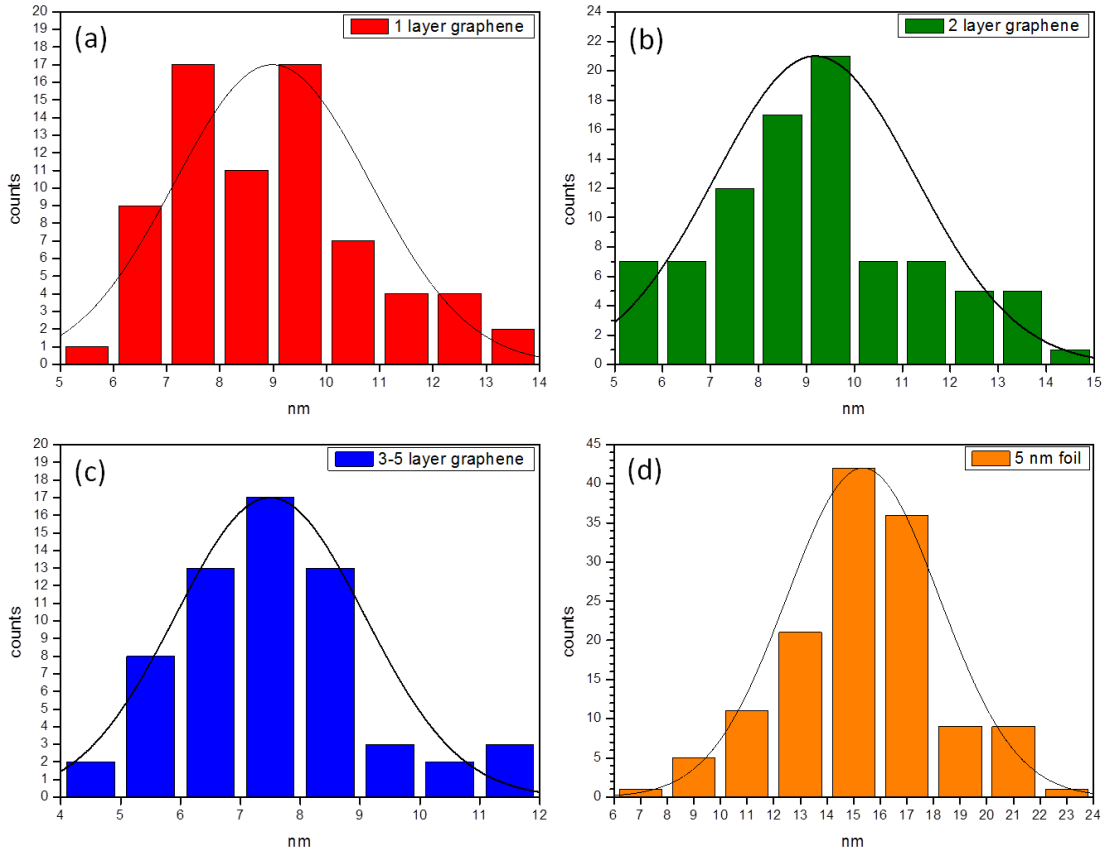

Figure VI–8. Size distribution of Au_{400}^{4+} impact-resulting holes examined with TEM. (a) 1L-graphene, (b) 2L-graphene, (c) 3-5L graphene, and (d) 5 nm carbon foil.

transmission electron starts. The yield of the reflection electron signal appearing in the transmission mass spectrum represents the extent of the correlation. Table VI-1 shows the results for the 1L-, 3-5L-graphene samples and the lacey carbon-covered grid. The correlation for the lacey carbon is lower by one order of magnitude than the graphene samples, indicating that the success rate to register simultaneous bi-directional emission from the lacey carbon support is only one tenth of that of a graphene sample. That is, the contribution of the lacey carbon-related signals to the graphene sample's mass spectral data obtained by synchronized starts amounts for ~9% assuming that the possibility of the projectiles impacting on the graphene and the lacey carbon is equal. These signals can result from the impacts on the peripherals of the lacey carbon patches (Figure VI-5) or the impacts which graze the edge of the lacey carbon strips.

Negative Ion Analysis

Figure VI-9 is a representative transmission mass spectrum of a graphene sample examined in negative ion mode. The samples were placed with the plane covered by graphene facing the transmission side. The spectrum is featured by a series of carbon clusters ranging from C_1^- to C_{14}^- with relatively lower abundance of C_nH^- and $C_nH_2^-$. Additionally, ions characteristic of the side products from the manufacture of the graphene (copper/copper chloride particles) are present at m/z 35, 37, 133, 135, 137 and 139 for Cl^- and $CuCl_2^-$. In contrast, a broader carbon cluster distribution with a maximum at C_{20}^- is observed in the transmission mass spectrum of the lacey carbon support (data not shown). The disappearance of the larger carbon clusters ($C_nH_x^-$, n>14)

in the graphene spectrum confirms the low spectral contribution from the lacey carbon support.

The SI yields of C_n^- computed from the graphene sheets and the lacey carbon are plotted as a function of cluster size in Figure VI-10. The data obtained from the 5 and 10 nm carbon foils are also included for comparison. Generally speaking, for n<10, the yields of C_n^- follow an odd-even oscillation where the yields of the even-numbered clusters are higher than those of the neighboring odd-numbered clusters, except for C_1^- and C_2^- in the foil case. The oscillation lies in an inherently higher electron affinity pertaining to the even-number clusters with n<10 which adopt a linear chain-like structure.[95] The absence or low abundance of light secondary ions (e.g. H^-, C_1^-, CH^-, CH_2^- and C_2^-) observed in the transmission mass spectra of the carbon foils has been reported and explained in ref [76]. Moreover, the graphene sheets exhibit a distinct cluster distribution where the yields decrease as the cluster size increases with a maximum at C_2^-, which is higher than C_{12}^- by two orders of magnitude. This distribution is different from that for the case of the carbon foils where the yields of clusters (n>2) are comparable within an order of magnitude. The yields of large cluster (n>9) are greater than those of graphene by one order of magnitude. The decreasing emission of the large clusters in the case of graphene is attributed to the finite amount of carbon atoms available for sputtering and SI production. The lacey carbon is an intermediate case where most of the data points fall between those of the other two cases.

Table VI-1. Extent of correlation in percentage between transmission and reflection electrons.

Sample	1L-graphene	3-5L-graphene	Lacey Carbon
%	23.3	23.5	2.3

Table VI-2. Fractional coverage of 5 nm dodecanethiol-coated AuNPs deposited on graphene. Entries 1 and 2 were computed from an ion pair comprising Au^- and one sulfur-containing ion and a pair comprising two sulfur-containing ions, respectively.

Entry	(Au^-, SH^-)	(Au^-, C_2S^-)	(Au^-, C_2SH^-)
1	14%	14%	16%
	(S^-, SH^-)	(S^-, C_2S^-)	(S^-, C_2SH^-)
2	14%	15%	14%

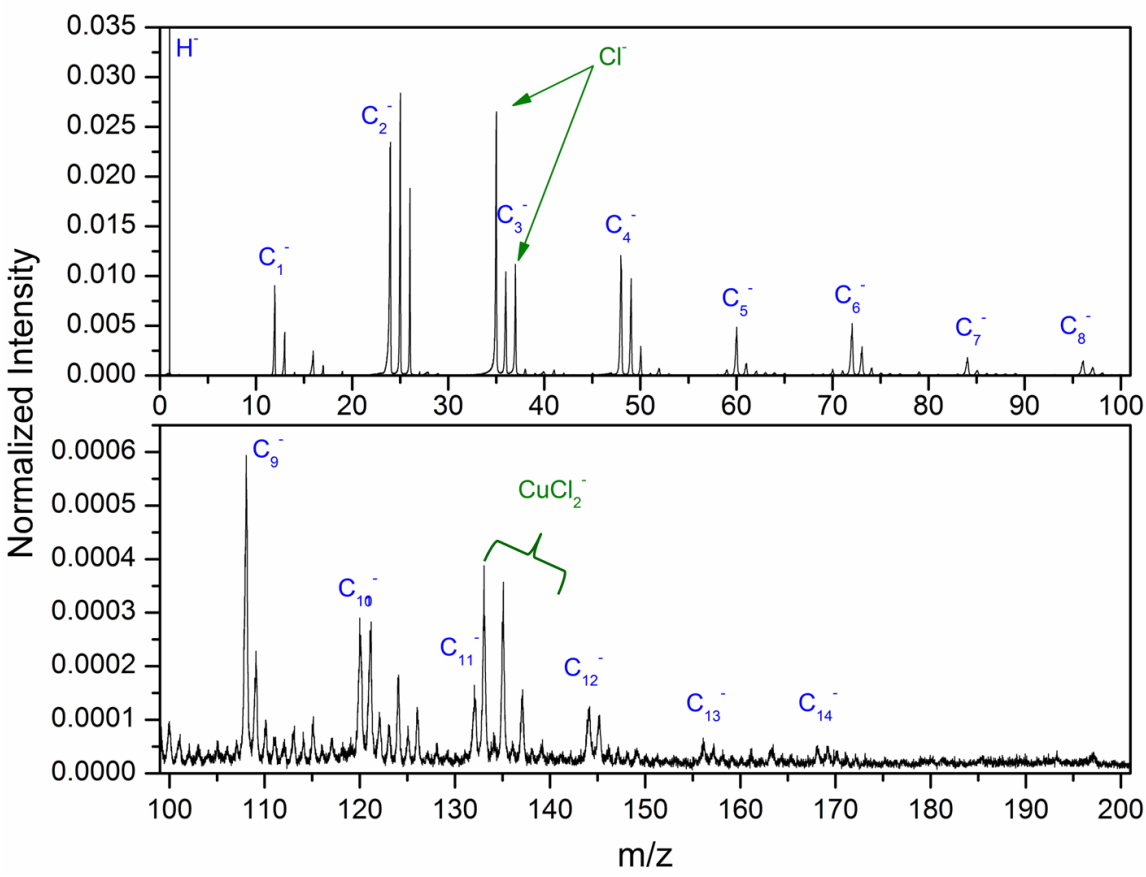

Figure VI–9. Transmission mass spectrum of 1L-graphene investigated with 520 keV Au_{400}-SIMS in negative ion mode. Peak intensities are normalized to the total number of events.

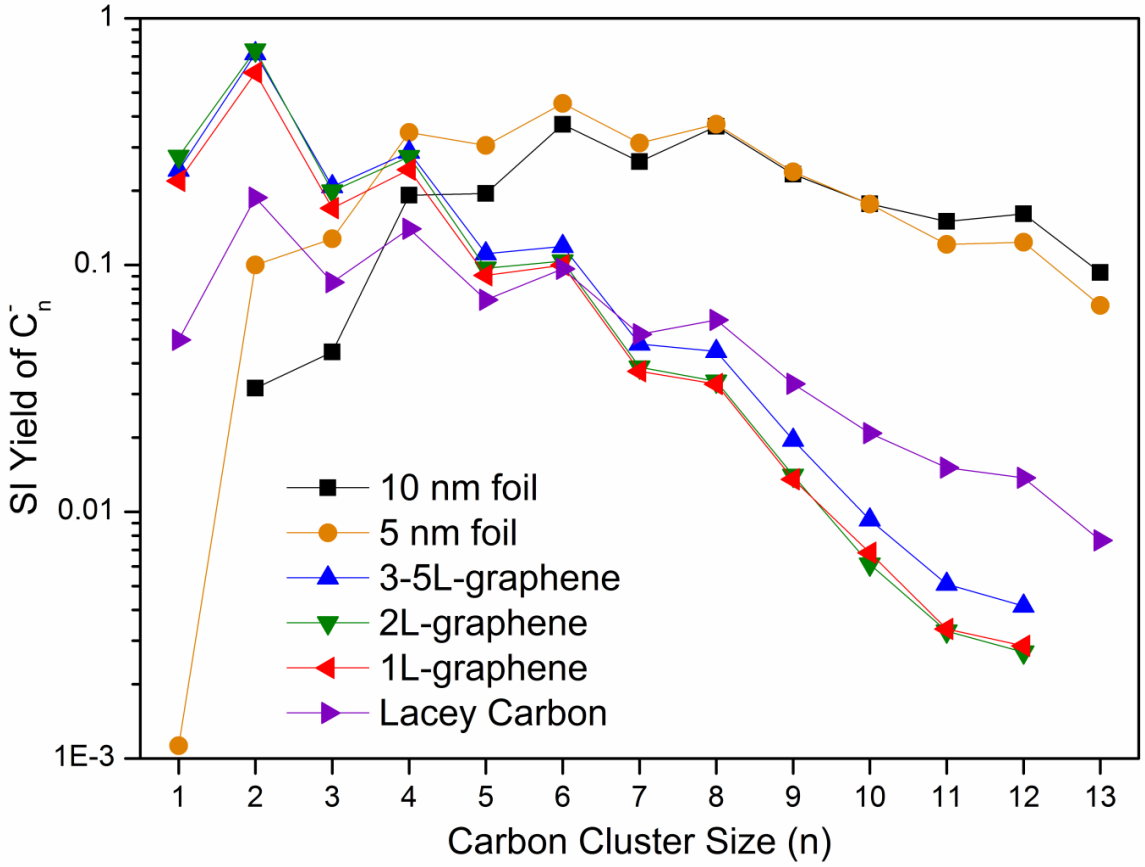

Figure VI–10. Secondary ion yields of C_n^- obtained from the transmission mass spectra of graphene, carbon foil, and lacey carbon samples.

The results for the hydrocarbon clusters, i.e. C_nH^- and $C_nH_2^-$, are presented in Figures VI-11a and VI-11b. The hydrocarbon clusters follow a trend similar to that of their C_n^- counterparts in the case of graphene where the yields decrease as n increases. For the carbon foils, the yields for clusters of the same parity are comparable whereas a larger fluctuation between the neighboring clusters is observed as compared to the C_n^- counterparts. Additionally, the odd-even oscillation still holds for larger clusters ($n \geqq 10$). The data points corresponding to C_3H^- and $C_{11}H_2^-$ are excluded in the case of graphene due to the isobaric interference with $^{37}Cl^-$ and $^{63}Cu^{35}Cl_2^-$ respectively from the copper chloride particles.

For the three graphene samples, the difference in yields of a given carbon cluster (C_n^-, C_nH^- and $C_nH_2^-$) is considered negligible, especially between the 1L- and 2L-graphene. The yields are not linearly proportional to the number of layers. For most clusters, the yields from the 3-5L-graphene are above those from the 1L-graphene by less than 20%.

Positive Ion Analysis

In addition to negative ions, positive ions emitted on the transmission side from the 440 keV Au_{400}^{4+} impacts on the carbon foils and the graphene sheets were also examined. Figure VI-12 presents the transmission mass spectra of the 10 and 5 nm carbon foils using the H^+ detected on the reflection side as the start signal for each time-of-flight event. For the 10 nm carbon foil, only two distinct peaks are present in the spectrum, corresponding to Na^+ and K^+. This implies that the 11.5 nm distance (corrected for 30^o

incidence) is beyond the range of the 440 keV Au_{400}^{4+} projectile. The projectile or its fragment comes to rest before reaching the exit of the film. The energy dissipated at the end of the projectile range is insufficient for excitation/ionization for materials at the exit site; however, it is sufficient for desorption of easily ionized species, e.g. Na^+ and K^+, from surface adsorbates. In the case of the 5 nm carbon foil, abundant carbon and hydrocarbon clusters are observed in the transmission mass spectrum, suggesting the 440 keV Au_{400}^{4+} has a range greater than 5.8 nm. We conclude that the transmission positive ion analysis of free-standing thin substrates with thicknesses of few nm is feasible.

The transmission mass spectrum (reflection H^+ start) of the 1L-graphene impacted by 440 keV Au_{400}^{4+} is shown in Figure VI-13a. In addition to the carbon clusters and alkaline ions, Cu^+ is present in the spectrum and contributed to the copper/copper chloride particles or grazing impacts on the Cu TEM grid. Moreover, an abundant emission of H^+, H_2^+, H_3^+ and C^+ is also observed for all the graphene samples. Their production in the conventional reflection direction has been reported in the studies using keV and MeV multicharged atomic projectiles[96] and MeV Au_{400} projectile[97] on molecular targets and is considered as the consequence of a strong electronic excitation process. The observation of H_n^+ and C^+ indicates an intense electronic excitation of graphene induced by the passage of the Au_{400}^{4+} projectile. In contrast, H_n^+ and C^+ were not detected in the transmission mass spectrum of the 5 nm carbon foil. This difference and the observation where the impact-resulting holes (~9 nm) are larger than the cross-

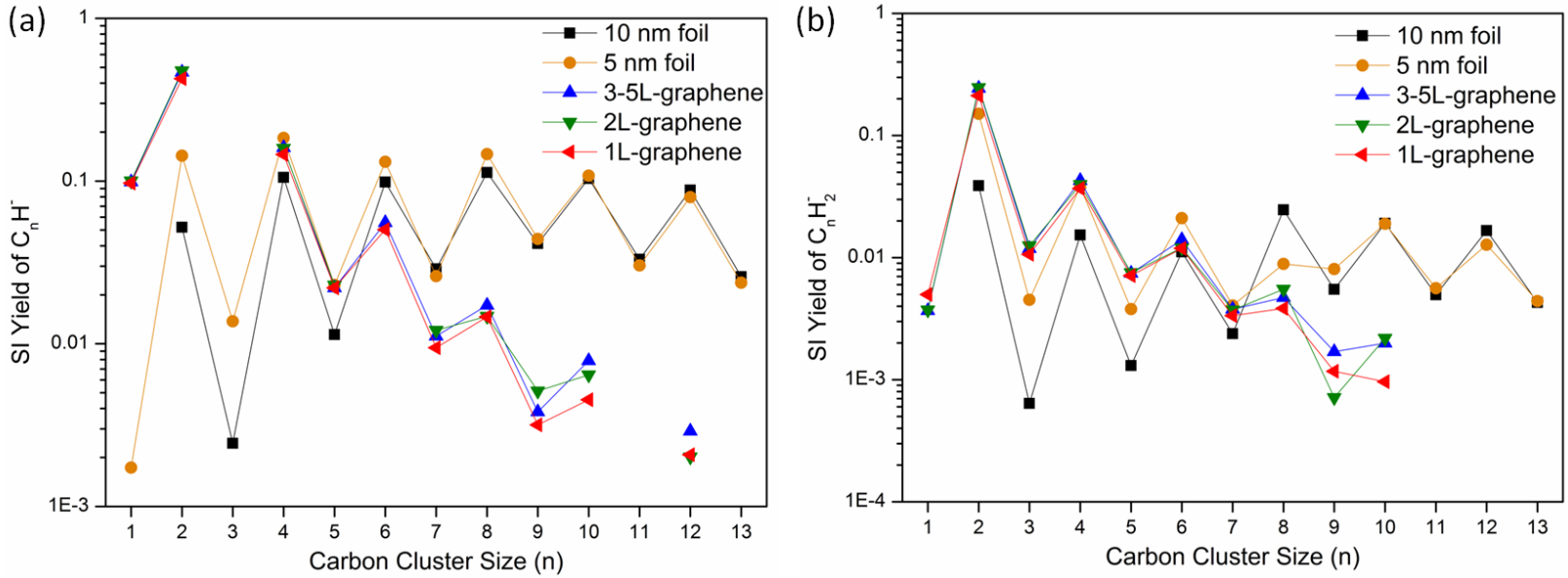

Figure VI–11. Secondary ion yields of (a) C_nH^- and (b) $C_nH_2^-$ obtained from the transmission mass spectra of graphene, and carbon foil samples.

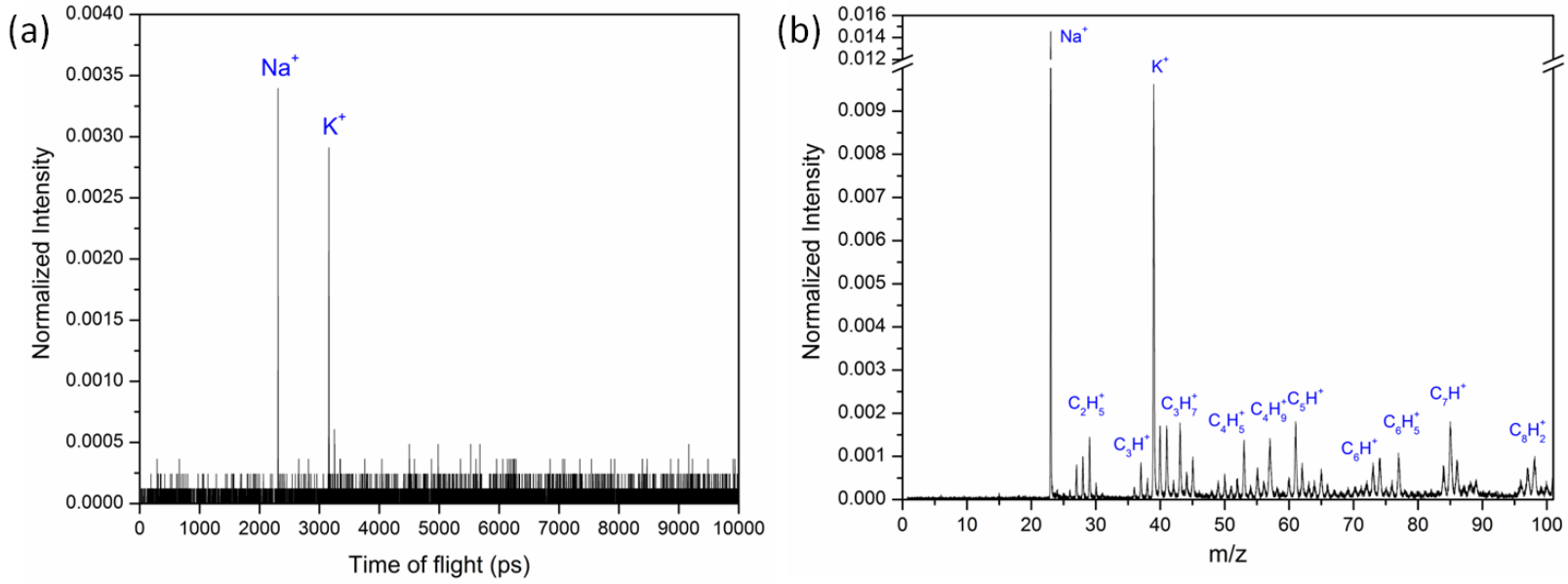

Figure VI–12. Transmission mass spectra of (a) 10 nm and (b) 5 nm carbon foil investigated with 440 keV Au_{400}-SIMS in positive ion mode. Events were registered using H^+ detected on the reflection side as the start signal. Peak intensities are normalized to the total number of events.

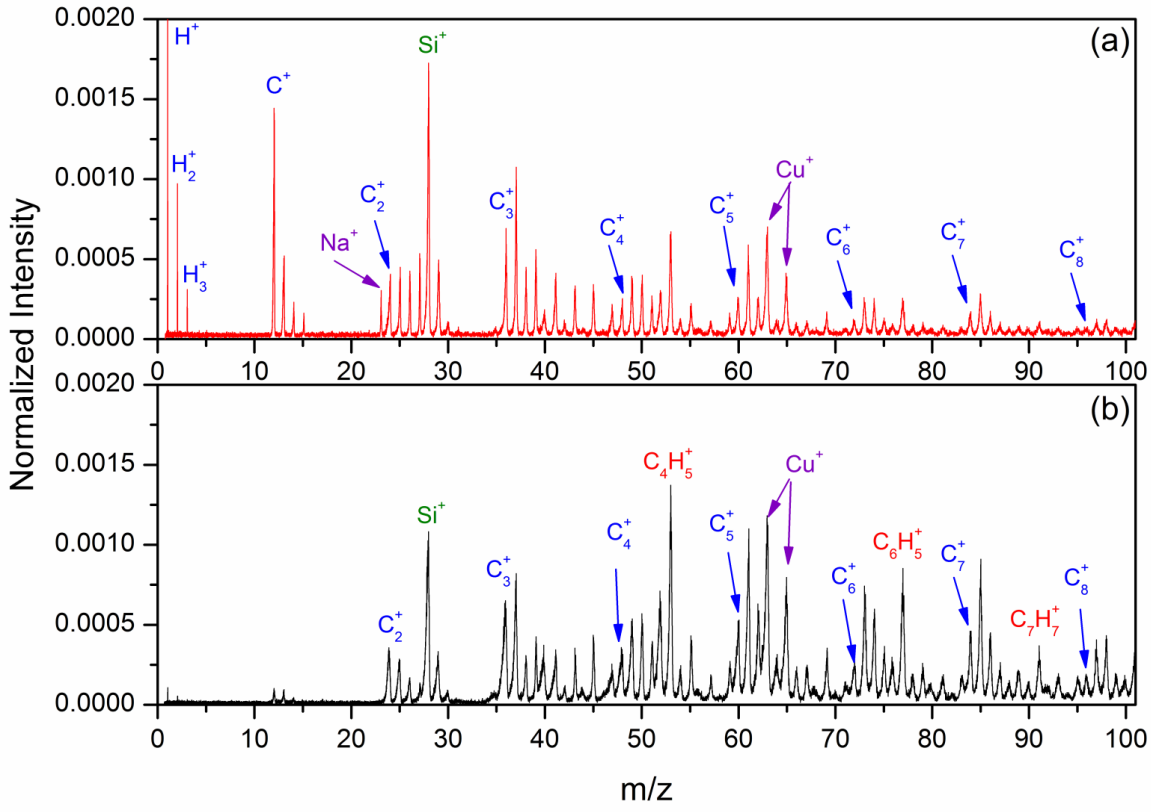

Figure VI–13. Transmission mass spectra of 1L-graphene investigated with 440 keV Au_{400}-SIMS in positive ion mode. Events were registered using H^+ detected on the (a) reflection or (b) transmission side as the start signal. Peak intensities are normalized to the total number of events.

section of the projectiles (~1.5 nm) imply an energy dissipation process unique to 2D materials.

As noted above, the abundant emission of H^+ in the transmission direction from graphene allows one to collect positive ion mass spectra using the transmission H^+ as the start signal for each time-of-flight event. The advantage of utilizing the transmission H^+ start is the improved mass resolution and the ability to detect heavier ions due to the better correlation of the simultaneously ejected secondary ions with their associated H^+ starts (Figure VI-13b). However, the tradeoff is a loss of ions below 20 amu due to the magnetic field applied to deflect H^+ to the start detector. The H^+ correlated yields of C_n^+ are plotted for each graphene sample in Figure VI-14. An odd-even oscillation is observed where the yields of the odd-numbered clusters are higher than those of the neighboring even-numbered clusters. Moreover, a magic numbered cluster, C_{11}^+, is evident with a relatively higher yield due to the stability associated with its structure.[98] This trend is similar to the result reported in a study where a C_{84} film was examined in the conventional reflection mode by highly charged projectiles.[98]

Effect of Projectile Size

In addition to Au_{400}^{4+}, the graphene samples were also investigated with small cluster projectiles, e.g. Au_3^+ and Au_9^+, of the same accelerating potential (130 kV) in the negative ion mode. Their respective mass spectra are presented in Figure VI-15 for comparison. Unlike Au_{400}^{4+}, only atomic or light cluster ions are present in the spectra

obtained from Au_3^+ and Au_9^+ projectile impacts. The yields of ejected C_n^- are lower by one and two orders of magnitude for Au_3^+ and Au_9^+ impacts respectively as compared to those from Au_{400}^{4+} impacts (Figure VI-16). Moreover, the odd-even oscillation is no longer prominent for Au_3^+.

The distinction between the small clusters and Au_{400}^{4+} lies in the difference in the projectile-matter interaction, which governs the excitation/ionization and desorption processes. The low velocity of 520 keV Au_{400}^{4+} (35.6 km/s) translates into an interaction time with the graphene of ~10^{-14} s. The latter is ~5.8 and 3.3 times longer than those for 130 keV Au_3^+ and Au_9^+ respectively. The transient passage of Au_3^+ and Au_9^+ with speeds above hypervelocity merely generates desorption of atomic and light clusters ions from the graphene sheet or adsorbates despite their inherent cluster effect. Moreover, no holes are observed on the graphene bombarded by Au_3^+ and Au_9^+ with TEM examination (data not shown), supporting the unique interaction pertaining to the Au_{400}^{4+} projectile.

Characterization of Small Nanoparticles on Graphene

The results discussed in the previous section indicate that the yields of characteristic ions, i.e. C_n^-, C_nH^- and $C_nH_2^-$, are practically the same for 1 to 5 graphene layers. Thus differences in the number of layers will be negligible with respect to the secondary ion emission from the nanoparticles. However, the graphene sheets supplied by Ted Pella Inc. had the copper/copper chloride particles left from the

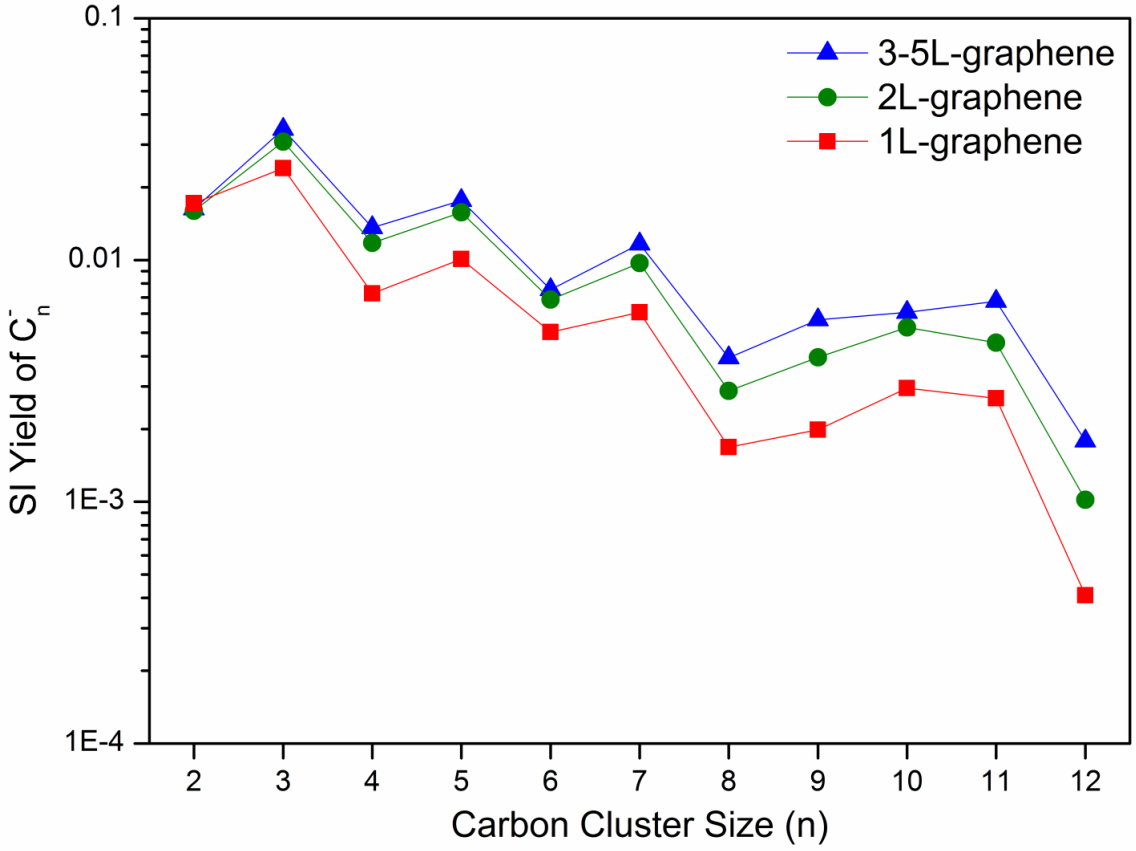

Figure VI–14. Secondary ion yields of C_n^+ obtained from the transmission mass spectra of the graphene samples. The data were acquired using H^+ detected on the transmission side as the start signal.

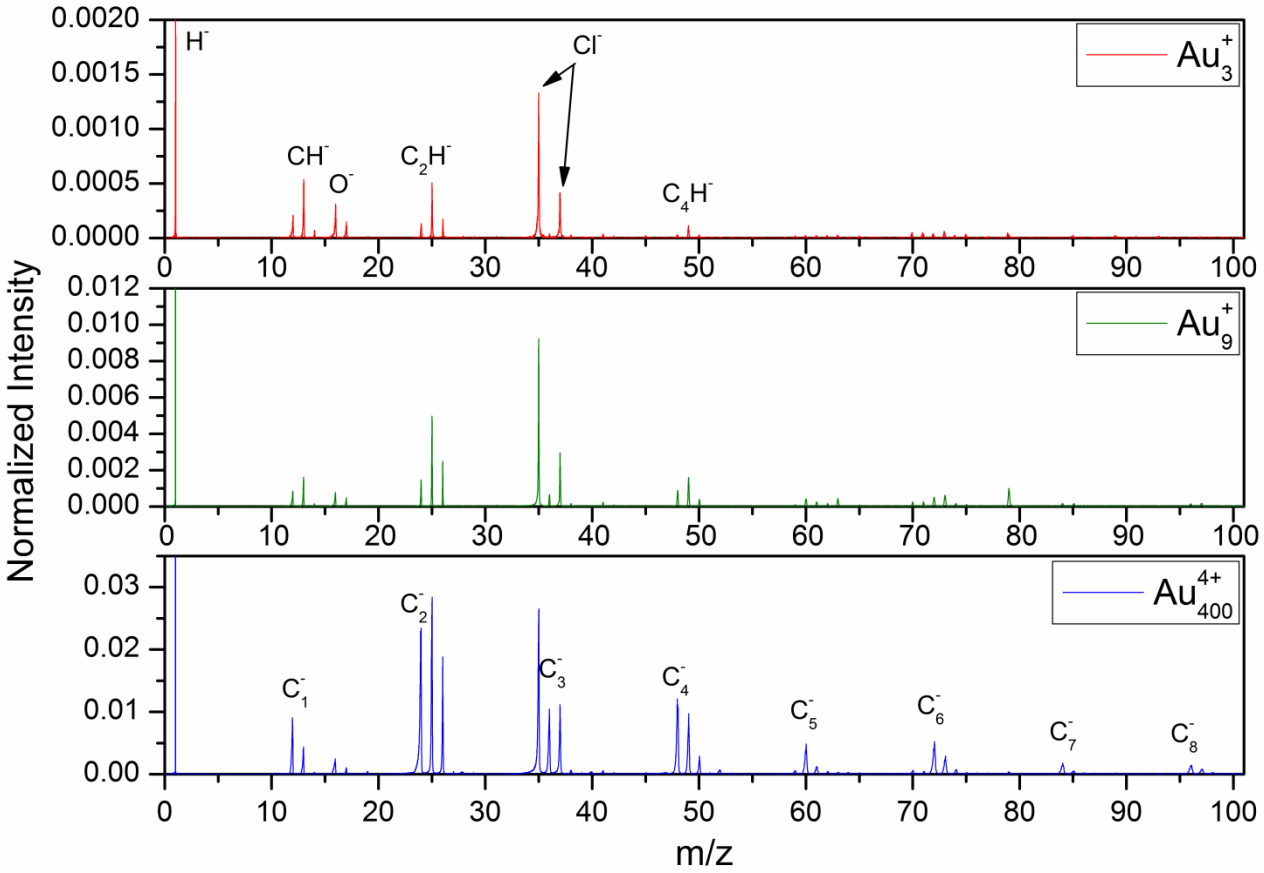

Figure VI–15. Negative ion transmission mass spectra of 1L-graphene investigated by 130 qkeV Au-LIMS SIMS with (a) Au_{400}^{4+}, (b) Au_9^+, and (c) Au_3^+ as the projectiles.

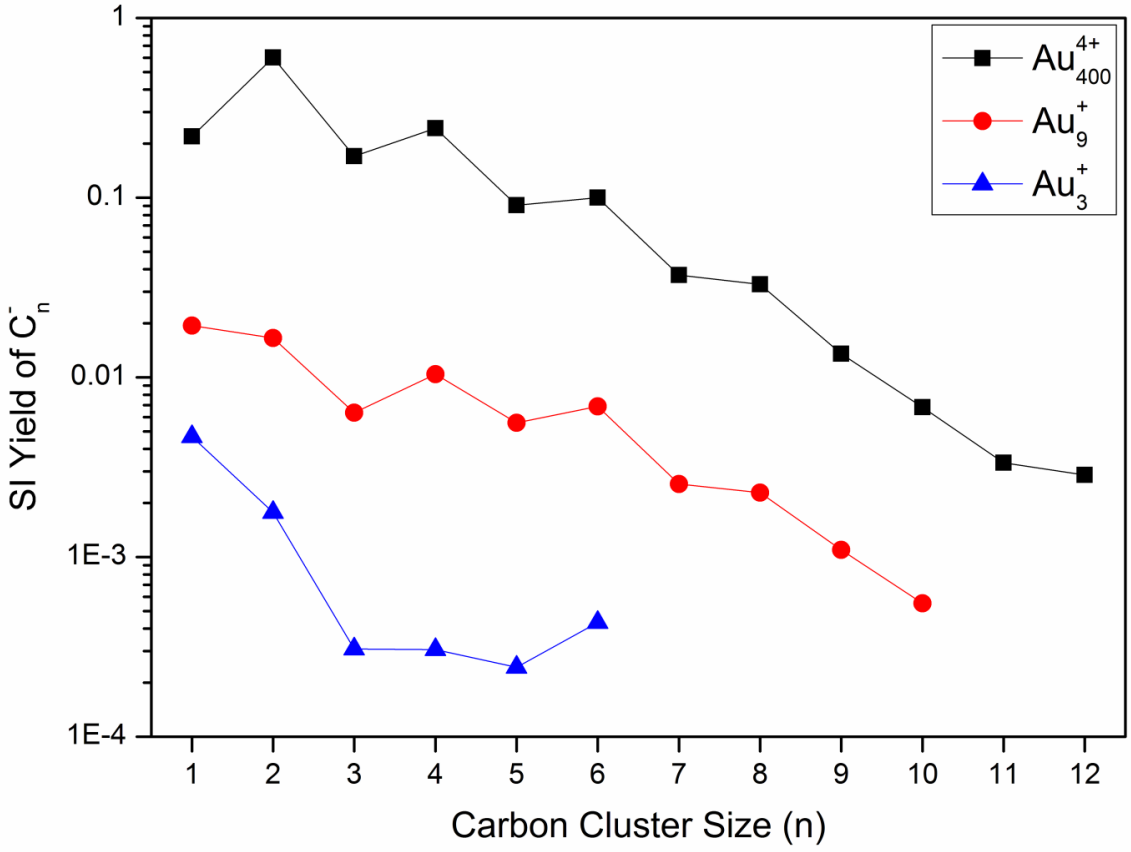

Figure VI–16. Secondary ion yields of C_n^- obtained from the transmission mass spectra of 1L-graphene examined with 520 keV Au_{400}^{4+}, 130 keV Au_9^+, and 130 keV Au_3^+ projectiles.

manufacturing process which contributed to the mass spectrum. As a consequence, we preferred graphene sheets grown on nickel foils supplied by Graphene Supermarket. No side products from the etching step in their manufacture process were observed on the graphene sheets by electron microscope and SIMS.

Figure VI-17 presents the TEM micrographs of the 5 nm dodecanethiol-capped AuNPs deposited onto the 1-6L graphene prepared for the investigation with transmission-SIMS. The images show that the AuNPs distributed themselves partially as a monolayer and partially as individually dispersed particles. With the given concentration/aliquot applied, no multiple layers were formed. The latter would be too thick for secondary ion emission in the transmission direction.

The transmission mass spectrum of the nanoparticles deposited on the 1-6L graphene is presented in Figure VI-18 and compared to that of the graphene support alone. In the m/z range of 10-200, the spectrum of the sample shares a similar pattern to that of the graphene support where the bare carbon and hydrocarbon clusters are dominant. However, a distinct peak is exclusively present at m/z 197 in the spectrum of the sample without any isobaric interference from the support and assigned as Au^-. Its presence indicates the 520 keV Au_{400}^{4+} projectile is capable of imparting its energy into the nanoparticles which are atomized/fragmented. The peak at m/z 197 features a fronting tail, suggesting that the projectile also transferred its momentum to the secondary ions emitted from the nanoparticle via the collision. In addition to Au^-, other ions characteristic of the nanoparticles are present in a higher m/z range (Figure VI-18b), including AuS^-, Au_2^-, Au_3^- and gold adducts involving the combination with fragments

from the dodecanethiol coating or the graphene support, e.g. $Au(C_2H_2)_2^-$ and $Au_2C_2H^-$. In contrast, none of the above gold-related ions except for the atomic recoil (i.e. Au^-) were detected in the mass spectrum simultaneously collected on the reflection side (Figure VI-19). The yield of Au^- on the reflection side is one order magnitude lower than that on the transmission side. The trend is in line with other observations showing that the secondary ions emit preferably in the transmission direction.

Since the data obtained on the transmission side are more informative, we use these for identifying co-emissions. The coincidence mass spectrum composed of events containing Au^- is plotted in Figure VI-20 and compared to the sample's total mass spectrum. Ions with enhanced abundance in the coincidence mass spectrum must originate from components co-localized with the AuNPs. In addition to the ions from the nanoparticles (e.g. Au_2^-, Au_3^-), characteristic ions of the thiol functional group of the capping molecules stand out, including S^-, SH^-, C_2S^-, C_2SH^- and C_4SH^- at m/z 32, 33, 56, 57, and 80 respectively. Moreover, C_nH^- clusters (n=2,4,6,8) are also enhanced, reflected by the higher ratios for the relative abundance of C_nH^- to C_n^- as compared to those in the total mass spectrum. The C_nH^- clusters originate from the saturated carbon chains of the dodecanethiol molecules, which is clearly distinguished from the unsaturated structure of graphene. These results indicate that combining the use of the graphene sheets of few layers as the substrate and the coincidence methodology is able to eliminate the ambiguity in the origin of C_nH^- despite the carbon-based substrate,

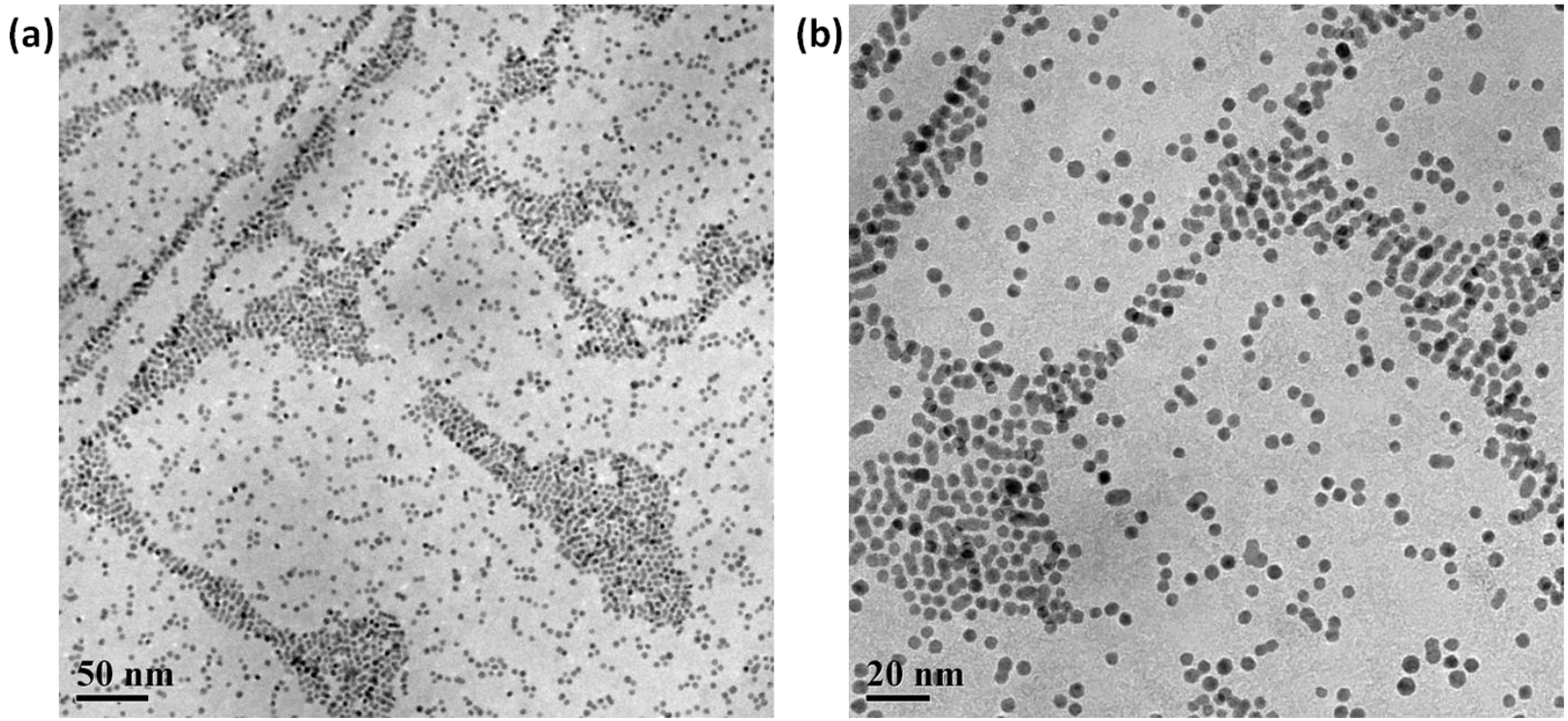

Figure VI–17. TEM micrographs of 5 nm dodecanethiol-coated AuNPs on 1-6L-graphene support (electron beam energy = 200 keV).

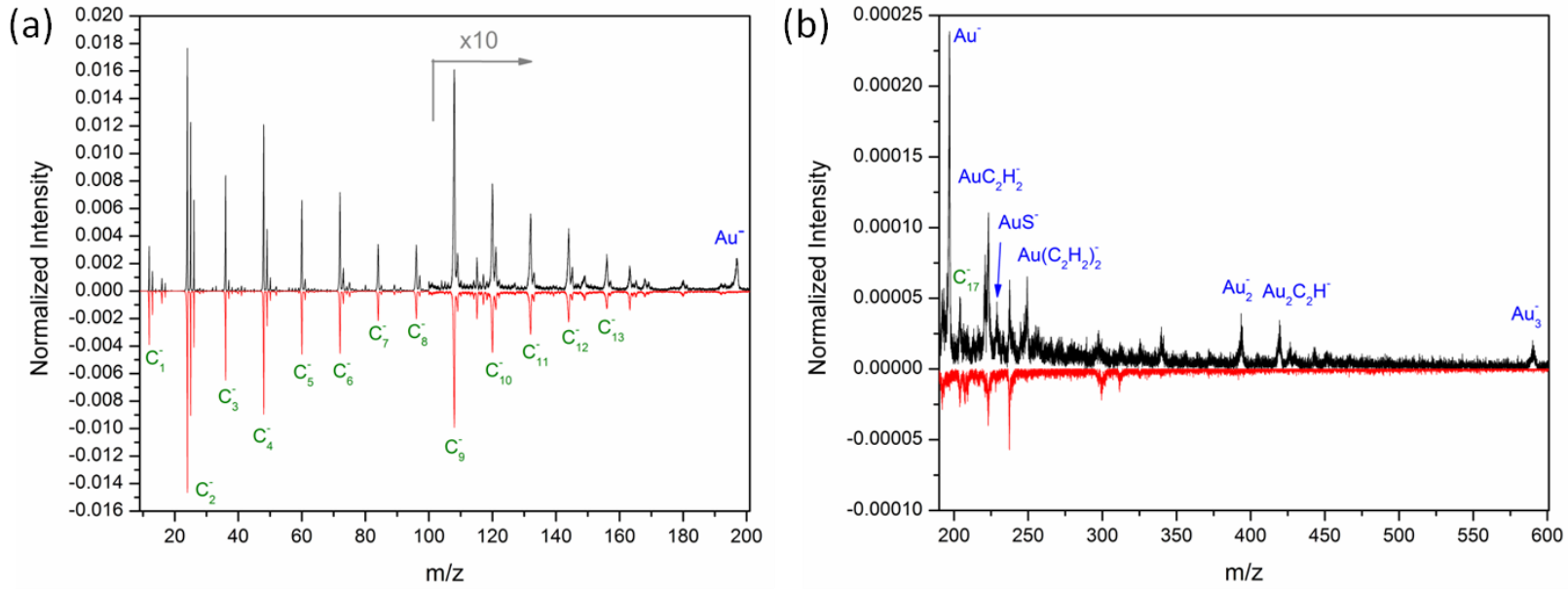

Figure VI–18. Negative ion transmission mass spectra of 5 nm dodecanethiol-coated AuNPs on 1-6L-graphene (top) and 1-6L graphene (bottom). m/z range: (a) 10-200 and (b) 190-600.

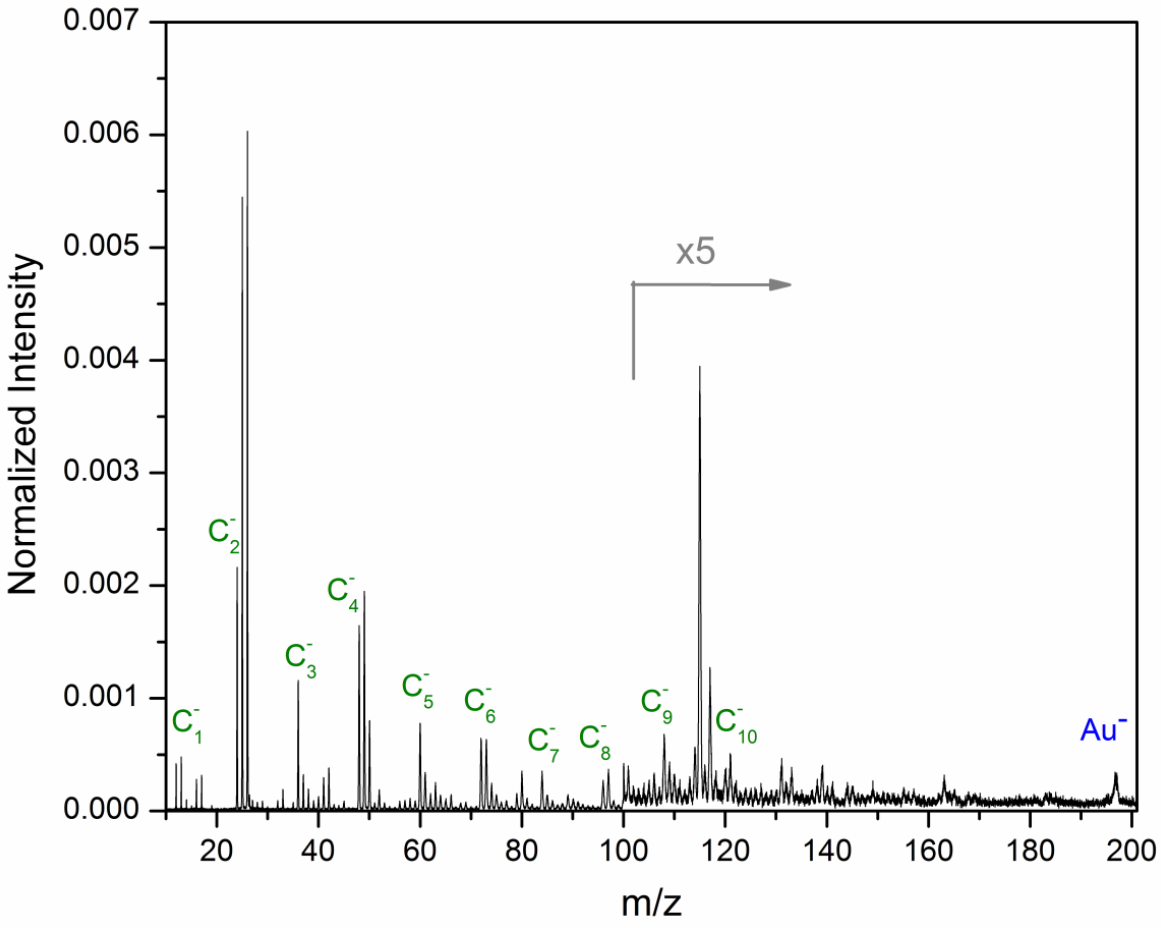

Figure VI–19. Negative ion reflection mass spectrum of 5 nm dodecanethiol-coated AuNPs on 1-6L-graphene support.

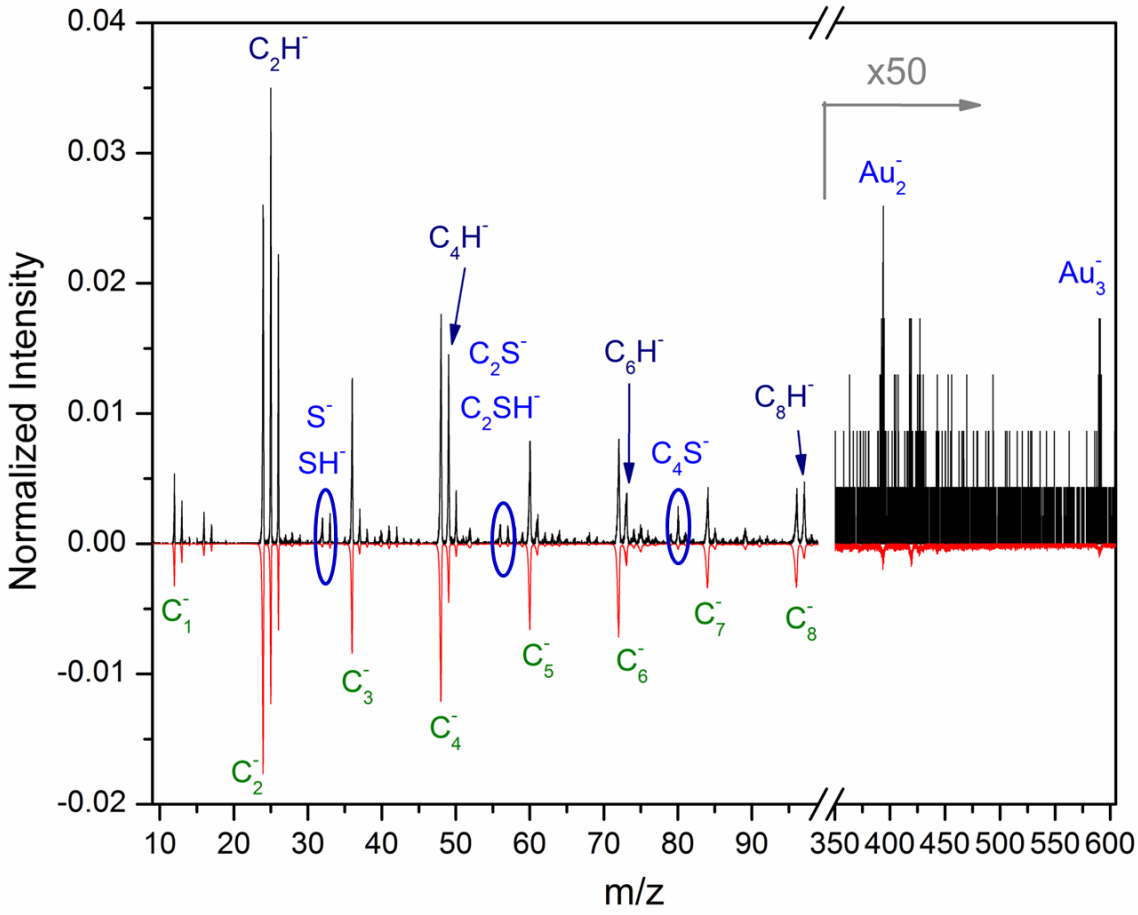

Figure VI–20. Total and coincidence mass spectra of 5 nm dodecanethiol-coated AuNPs. Top: negative ion transmission mass spectrum consisting of secondary ions co-emitted with Au^- from 5 nm dodecanethiol-coated AuNPs on 1-6L-graphene. Peak intensities are normalized to the number of the selected events. Bottom: negative ion transmission mass spectrum consisting of total events collected from the sample.

enabling the identification of organic surface modifiers capped on the small nanoparticles with transmission-SIMS.

The fractional coverage derived from the coincidence methodology (Chapter II) can also be obtained from the data collected in the transmission mode. The coverage computed from a pair of ejecta comprising Au^- and one sulfur-containing ion or a pair of two different sulfur-containing ions is given in Table VI-2. The data show that the difference in the results calculated from the two pairs is ≤10 %, again supporting that the dodecanethiol molecules are predominantly associated with the gold nanoparticles.

Conclusion

In this study, we present a new SIMS approach for small nanoparticle (≦10 nm) characterization with the custom-built instrument comprising two ToF detection systems. Simultaneously bi-directional ejecta from objects bombarded by individual Au_{400}^{4+} impacts can be collected and analyzed. Graphene sheets of 1-6 layers were used as the substrate for the test sample, i.e. the 5 nm dodecanethiol-capped AuNPs. The results show that SIs characteristic of the gold nanoparticles were detected preferably in the transmission direction. The coincidence methodology enables to extract molecular information on the capping molecules. In the present case, as they are saturated they can be readily distinguished from the graphene substrate. These findings show that transmission-SIMS operating in the event-by-event mode is a tool suitable for the molecular characterization of small surface-modified nanoparticles. The estimate for a limit of detection (LOD) in the transmission mode is ~3 fg.

CHAPTER VII

CONCLUSIONS

The key rationale for SIMS with massive projectiles is their ability to generate emission of multiple SIs at the level of a single impact. Thus bombardment by one projectile at a time becomes practical. This approach in turn offers several distinct features for nanoscale analysis. The volume analyzed per impact is nanometric, ~10-15 nm in diameter and a few nm ($\leqq$10 nm) in depth. The co-emitted ejecta originate from co-localized species. Moreover, a methodology derived from the event-by-event bombardment/detection mode enables the quantification of the factional coverage of a given analyte on a surface. The aim of this study was to take advantage of these features for the advancement of nano-analysis. The findings of our study and recommendation for future work are summarized below.

Analysis of Individual Nano-Objects

The objects tested were spatially dispersed and probed one-by-one, avoiding concerns such as ensemble averaging and interferences from the object's environment. As a model of biological nano-objects, we chose bacteriophages. Sample preparation focused on key requirements: physical dispersion and preservation of specimen integrity during analysis. The results showed that the mass spectrum specific to the bacteriophage could be extracted by applying the coincidence/anticoincidence selection. This methodology enhances the accuracy of SI identification and the quality of analytical information for nano-objects.

In the study of individual gold nanoparticles (AuNPs), we found that the SI yields of NP-related ions are dependent on the particle size. Enhancement in their emission from nanoparticles of a given size was also observed in comparison to a bulk surface for a given projectile. The findings of size- and projectile-dependent SI emission point out the necessity of accurate data interpretation when dealing with nano-scaled objects. Moreover, we could identify different types of impacts on nanoparticles based on different co-emission events for NPs $\geqq$ 10 nm, whereas the distinction was blurred for those smaller than 10 nm.

Nano-Domain Analysis

In the examination of the pyrolized mixtures of vitamin B12 and carbon black, we verified the structure of the catalytically active site with the observation of $CoN_4C_x^-$. The Co-N_4 moiety is in agreement with the results obtained by XAS. The co-emission events revealed the chemical environment of the active site in a nano-domain as a function of its activity. Moreover, we could quantify the degree of dispersion of the active site among the carbon black, a measure providing a direction for future device optimization.

SIMS for Ultra Small Nanoparticle Characterization

We present here the methodology of transmission-SIMS. The approach was validated with 5 nm dodecanethiol-capped AuNPs deposited on a few sheets of free-standing graphene. The results showed the emission of NP-related ions is preferred in the transmission direction, implying a better sensitivity as opposed to the conventional reflection direction. Additionally, the coincidence methodology allowed one to extract

the information of the capping molecules and also to determine the surface coverage of the 5 nm AuNPs.

Future Work

Evaluation of NP-Mediated SI Emission

The investigation of individual nanoparticles could be extended to explore whether the SI emission of an analyte, either immobilized on or encapsulated in a nanoparticle, behaves differently compared to a bulk-like counterpart. Kim et al. reported an enhancement in ion emission from peptides adsorbed on 3 nm AuNPs with atomic projectiles.[99,100] Studies can be pursued concerning whether the enhancement could be observed with cluster projectiles (Au_{400}, C_{60}). Test cases could be self-assembled monolayer (SAM) of thiol containing molecules on AuNPs or biomolecule-conjugated AuNPs.

Optimization of Transmission-SIMS

More investigation is required to understand the transmission mode from both the application and fundamental points of view. On the substrate itself, we found that the holes on the graphene sheets (~9 nm) resulting from individual Au_{400} impacts are larger than the cross-section of the projectile (~1.5 nm) by close to an order of magnitude, implying an efficient energy deposition into the graphene sheets via the transient interaction. It is important to understand the energy deposition mechanism and also the fate of the projectile after traversing graphene. The thickness effect of the substrate on the SI emission from the nanoparticles should also be examined. With the test samples where the 5 nm dodecanethiol-capped AuNPs are deposited onto 1L-graphene, 5 nm-,

and 10 nm carbon foils, the yields of the ions characteristic of the AuNPs and capping molecules can be compared as a function of thickness. In addition, the angle of incident for optimal SI emission must be determined.

Investigation of individual nanoparticles is technically feasible in the transmission mode. The key step is to immobilize individual nanoparticles onto the graphene substrate. Like the AuNPs studied in Chapter IV, the graphene sheets could be functionalized with a positively charged layer by silanization[101] such that the nanoparticles can be immobilized electrostatically. By testing samples with individual AuNPs of different sizes, the size limit of NPs suitable for the transmission mode could be determined.

Examination of Electron/Photon Emission from Individual Nanoparticles

It has been shown that the emission of electrons is also affected by the dimension and the chemical composition of the specimen.[37,39] Further, photon emission was observed from massive cluster impacts on bulk samples.[34,35] Nothing is known about such emission from nanoprojectile-NP impacts. Studies should focus on the effects of size and composition on the emission of electrons and possibly photons from massive cluster impacts on individual AuNPs in the range of 2-50 nm.

Analysis of Complex Nano-Objects

Another direction for further research concerns the analysis of complex nano-objects. For those larger than the projectile's desorption volume, e.g. α-ZrP nanoplatelet[102], Au_{400} or C_{60} can be applied in the conventional reflection mode to examine the chemical modification on the surface of the ZrP nanoplatelet. The

coincidence methodology can help verify if the modifier molecules localize on the surface and quantify the degree of coating of the modifier over the nanoplatelet's surface.

For ultra-small molecular assemblies of dimensions smaller than the projectile's desorption volume, the challenge is to devise optimal condition for analysis. Future research should focus on means to maximize ionization probabilities. Should ultra-small objects be deposited on a thick substrate promoting ionization (silver, nitrocellulose…) or one graphene combined with an array of detectors in a quasi-spherical arrangement?

REFERENCES

(1) Whitesides, G. M. *Small* **2005**, *1*, 172.

(2) Baer, D. R.; Engelhard, M. H.; Johnson, G. E.; Laskin, J.; Lai, J. F.; Mueller, K.; Munusamy, P.; Thevuthasan, S.; Wang, H. F.; Washton, N.; Elder, A.; Baisch, B. L.; Karakoti, A.; Kuchibhatla, S. V. N. T.; Moon, D. *J. Vac. Sci.Technol. A* **2013**, *31*, 050820.

(3) Richman, E. K.; Hutchison, J. E. *ACS Nano* **2009**, *3*, 2441.

(4) Gunnarsson, A.; Kollmer, F.; Sohn, S.; Höök, F.; Sjövall, P. *Anal. Chem.* **2010**, *82*, 2426.

(5) Senoner, M.; Unger, W. E. S. *J. Ana.l Atomic Spectrom.* **2012**, *27*, 1050.

(6) Lai, S. C. S.; Dudin, P. V.; Macpherson, J. V.; Unwin, P. R. *J. Am. Chem. Soc.* **2011**, *133*, 10744.

(7) Baer, D. R.; Gaspar, D. J.; Nachimuthu, P.; Techane, S. D.; Castner, D. G. *Anal. Bioanal. Chem.* **2010**, *396*, 983.

(8) Fletcher, J. S.; Lockyer, N. P.; Vickerman, J. C. *Surf. Interface Anal.* **2006**, *38*, 1393.

(9) Benninghoven, A. *Phys Status Solidi* **1969**, *34*, K169.

(10) Winograd, N. *Anal. Chem.* **2005**, *77*, 142 A.

(11) Grønlund, F.; Moore, W. J. *J. Chem. Phys.* **1960**, *32*, 1540.

(12) Rol, P. K.; Fluit, J. M.; Kistemaker, J. *Physica* **1960**, *26*, 1000.

(13) Wucher, A. *Appl. Surf. Sci.* **2006**, *252*, 6482.

(14) Appelhans, A. D.; Delmore, J. E. *Analytical Chemistry* **1989**, *61*, 1087.

(15) Blain, M. G.; Della-Negra, S.; Joret, H.; Le Beyec, Y.; Schweikert, E. A. *Phys. Rev. Lett.* **1989**, *63*, 1625.

(16) Benguerba, M.; Brunelle, A.; Della-Negra, S.; Depauw, J.; Joret, H.; Le Beyec, Y.; Blain, M. G.; Schweikert, E. A.; Assayag, G. B.; Sudraud, P. *Nucl. Instrum. Meth.B* **1991**, *62*, 8.

(17) Bouneau, S.; Brunelle, A.; Della-Negra, S.; Depauw, J.; Jacquet, D.; Le Beyec, Y.; Pautrat, M.; Fallavier, M.; Poizat, J. C.; Andersen, H. H. *Phys. Rev. B* **2002**, *65*, 144106.

(18) VanStipdonk, M. J.; Harris, R. D.; Schweikert, E. A. *Rapid Commun. Mass Sp.* **1996**, *10*, 1987.

(19) Wong, S. C. C.; Hill, R.; Blenkinsopp, P.; Lockyer, N. P.; Weibel, D. E.; Vickerman, J. C. *Appl. Surf. Sci.* **2003**, *203*, 219.

(20) Weibel, D.; Wong, S.; Lockyer, N.; Blenkinsopp, P.; Hill, R.; Vickerman, J. C. *Anal. Chem.* **2003**, *75*, 1754.

(21) Shen, K.; Mao, D.; Garrison, B. J.; Wucher, A.; Winograd, N. *Anal. Chem.* **2013**, *85*, 10565.

(22) Lu, C.; Wucher, A.; Winograd, N. *Anal. Chem.* **2010**, *83*, 351.

(23) Zheng, L. L.; Wucher, A.; Winograd, N. *Anal. Chem.* **2008**, *80*, 7363.

(24) Fletcher, J. S.; Lockyer, N. P.; Vaidyanathan, S.; Vickerman, J. C. *Anal. Chem.* **2007**, *79*, 2199.

(25) Tempez, A.; Schultz, J. A.; Della-Negra, S.; Depauw, J.; Jacquet, D.; Novikov, A.; Lebeyec, Y.; Pautrat, M.; Caroff, M.; Ugarov, M.; Bensaoula, H.; Gonin, M.; Fuhrer, K.; Woods, A. *Rapid Commun. Mass Sp.* **2004**, *18*, 371.

(26) Bouneau, S.; Della-Negra, S.; Depauw, J.; Jacquet, D.; Le Beyec, Y.; Mouffron, J. P.; Novikov, A.; Pautrat, M. *Nucl. Instrum. Meth. B* **2004**, *225*, 579.

(27) Della-Negra, S.; Arianer, J.; Depauw, J.; Verkhoturov, S. V.; Schweikert, E. A. *Surf. Interface Anal.* **2011**, *43*, 66.

(28) DeBord, J. D.; Fernandez-Lima, F. A.; Verkhoturov, S. V.; Schweikert, E. A.; Della-Negra, S. *Surf. Interface Anal.* **2013**, *45*, 134. (Reprinted permission date: July 14 2014)

(29) DeBord, J. D.; Verkhoturov, S. V.; Perez, L. M.; North, S. W.; Hall, M. B.; Schweikert, E. A. *J. Chem. Phys.* **2013**, *138*, 214301.

(30) Rickman, R. D.; Verkhoturov, S. V.; Hager, G. J.; Schweikert, E. A. *Int. J. Mass Spectrom.* **2005**, *245*, 48.

(31) Park, M. A.; Gibson, K. A.; Quinones, L.; Schweikert, E. A. *Science* **1990**, *248*, 988.

(32) Verkhoturov, S. V.; Schweikert, E. A.; Rizkalla, N. M. *Langmuir* **2002**, *18*, 8836.

(33) Chen, L. J.; Seo, J. H.; Eller, M. J.; Verkhoturov, S. V.; Shah, S. S.; Revzin, A.; Schweikert, E. A. *Anal. Chem.* **2011**, *83*, 7173.

(34) Fernandez-Lima, F. A.; Eller, M. J.; Verkhoturov, S. V.; Della-Negra, S.; Schweikert, E. A. *J. Phys. Chem. Lett.* **2010**, *1*, 3510.

(35) Fernandez-Lima, F. A.; Pinnick, V. T.; Della-Negra, S.; Schweikert, E. A. *Surf. Interface. Anal.* **2011**, *43*, 53.

(36) Eller, M. J.; Verkhoturov, S. V.; Della-Negra, S.; Schweikert, E. A. *Rev. Sci. Instrum.* **2013**, *84*.

(37) Verkhoturov, S. V.; Eller, M. J.; Rickman, R. D.; Della-Negra, S.; Schweikert, E. A. *J. Phys. Chem. C* **2010**, *114*, 5637.

(38) Pinnick, V.; Rajagopalachary, S.; Verkhoturov, S. V.; Kaledin, L.; Schweikert, E. A. *Anal. Chem.* **2008**, *80*, 9052.

(39) Eller, M. J.; Verkhoturov, S. V.; Della-Negra, S.; Schweikert, E. A. *J. Phys. Chem. C* **2010**, *114*, 17191.

(40) Zimmermann, S.; Urbassek, H. M. *Int. J. Mass Spectrom.* **2008**, *272*, 91.

(41) Järvi, T. T.; Pakarinen, J. A.; Kuronen, A.; Nordlund, K. *EPL* **2008**, *82*, 26002.

(42) Yang, L.; Seah, M. P.; Anstis, E. H.; Gilmore, I. S.; Lee, J. L. S. *J. Phys. Chem. C* **2012**, *116*, 9311.

(43) Pinnick, V. T.; Verkhoturov, S. V.; Kaledin, L.; Bisrat, Y.; Schweikert, E. A. *Anal. Chem.* **2009**, *81*, 7527.

(44) Chen, L. J.; Shah, S. S.; Silangcruz, J.; Eller, M. J.; Verkhoturov, S. V.; Revzin, A.; Schweikert, E. A. *Int. J. Mass Spectrom.* **2011**, *303*, 97.

(45) Rajagopalachary, S.; Verkhoturov, S. V.; Schweikert, E. A. *Nano Lett.* **2008**, *8*, 1076.

(46) DeBord, J. D. Ph.D. Dissertation. Texas A&M University, College Station, Texas, **2013**.

(47) Taylor, G. *Proceedings of the Royal Society of London. Series A. Mathematical and Physical Sciences* **1964**, *280*, 383.

(48) Eller, M. J. Ph.D. Dissertation. Texas A&M University, College Station, Texas, **2013**.

(49) Brunelle, A.; Dellanegra, S.; Depauw, J.; Joret, H.; Lebeyec, Y. *Rapid Commun. Mass Sp.* **1991**, *5*, 40.

(50) Rickman, R. D.; Verkhoturov, S. V.; Hager, G. J.; Schweikert, E. A.; Bennett, J. A. *Int. J. Mass Spectrom.* **2005**, *241*, 57.

(51) Rickman, R. D. Ph.D. Dissertation. Texas A&M University, College Station, Texas, **2004**.

(52) Chen, L.-J. Ph.D. Dissertation. Texas A&M University, College Station, Texas, **2012**.

(53) Rajagopalachary, S. R. Ph.D. Dissertation. Texas A&M University, College Station, Texas, **2010**.

(54) Li, Z.; Verkhoturov, S. V.; Schweikert, E. A. *Anal. Chem.* **2006**, *78*, 7410.

(55) Li, Z.; Verkhoturov, S. V.; Locklear, J. E.; Schweikert, E. A. *Int. J. Mass Spectrom.* **2008**, *269*, 112.

(56) Liang, C.-K.; Verkhoturov, S. V.; Chen, L.-J.; Schweikert, E. A. *Int. J. Mass Spectrom.* **2013**, *334*, 43.

(57) Daniels, R. H.; Dikler, S.; Li, E.; Stacey, C. *J. Asso. Lab. Auto.* **2008**, *13*, 314.

(58) Go, E. P.; Apon, J. V.; Luo, G.; Saghatelian, A.; Daniels, R. H.; Sahi, V.; Dubrow, R.; Cravatt, B. F.; Vertes, A.; Siuzdak, G. *Anal. Chem.* **2005**, *77*, 1641.

(59) Golmohammadi, R.; Fridborg, K.; Bundule, M.; Valegård, K.; Liljas, L. *Structure* **1996**, *4*, 543.

(60) Stopar, D.; Spruijt, R. B.; Wolfs, C. J. A. M.; Hemminga, M. A. *BBA-Biomembranes* **2003**, *1611*, 5.

(61) Guillermier, C.; Negra, S. D.; Rickman, R. D.; Hager, G. J.; Schweikert, E. A. *Int. J. Mass Spectrom.* **2007**, *263*, 298.

(62) Muramoto, S.; Brison, J.; Castner, D. G. *Anal. Chem.* **2011**, *84*, 365.

(63) Li, X.-B.; Wang, H.-Y.; Yang, X.-D.; Zhu, Z.-H.; Tang, Y.-J. *J. Chem. Phys.* **2007**, *126*.

(64) Rickman, R. D.; Verkhoturov, S. V.; Parilis, E. S.; Schweikert, E. A. *Phys. Rev. Lett.* **2004**, *92*.

(65) Riordan, J. An Introduction to Combinatorial Analysis, John Wiley & Sons Inc., New York, London, **1958**, pp.90.

(66) Cumberland, S. L.; Strouse, G. F. *Langmuir* **2001**, *18*, 269.

(67) Qi, W. H.; Wang, M. P. *J. Mater. Sci. Lett.* **2002**, *21*, 1743.

(68) Restrepo, O. A.; Prabhakaran, A.; Delcorte, A. *Nucl. Instrum. Meth. B* **2011**, *269*, 1595.

(69) Kaplan, A.; Manor, Y.; Bekkerman, A.; Tsipinyuk, B.; Kolodney, E. *J. Chem. Phys.* **2004**, *120*, 1572.

(70) Yu, M. L. in: Behrisch, R.; Wittmaack, K. (Eds.), Sputtering by Particle Bombardment III, Springer-Verlag, Berlin, **1991**, pp.91.

(71) Verkhoturov, S. V.; Eller, M. J.; Della-Negra, S.; Rickman, R. D.; Locklear, J. E.; Schweikert, E. A. *Surf. Interface Anal.* **2011**, *43*, 49.

(72) Chen, Z.; Higgins, D.; Yu, A.; Zhang, L.; Zhang, J. *Energy Environ. Sci.* **2011**, *4*, 3167.

(73) Bezerra, C. W. B.; Zhang, L.; Lee, K.; Liu, H.; Marques, A. L. B.; Marques, E. P.; Wang, H.; Zhang, J. *Electrochim. Acta* **2008**, *53*, 4937.

(74) Chang, S.-T.; Wang, C.-H.; Du, H.-Y.; Hsu, H.-C.; Kang, C.-M.; Chen, C.-C.; Wu, J. C. S.; Yen, S.-C.; Huang, W.-F.; Chen, L.-C.; Lin, M. C.; Chen, K.-H. *Energy Enviro. Sci.* **2012**, *5*, 5305.

(75) Bezerra, C. W. B.; Zhang, L.; Liu, H.; Lee, K.; Marques, A. L. B.; Marques, E. P.; Wang, H.; Zhang, J. *J. Power Sources* **2007**, *173*, 891.

(76) DeBord, J. D.; Della-Negra, S.; Fernandez-Lima, F. A.; Verkhoturov, S. V.; Schweikert, E. A. *J. Phys. Chem. C* **2012**, *116*, 8138.

(77) Huang, H.-C.; Shown, I.; Chang, S.-T.; Hsu, H.-C.; Du, H.-Y.; Kuo, M.-C.; Wong, K.-T.; Wang, S.-F.; Wang, C.-H.; Chen, L.-C.; Chen, K.-H. *Adv. Func. Mater.* **2012**, *22*, 3500.

(78) Biscoe, J.; Warren, B. E. *J. Appl. Phys.* **1942**, *13*, 364.

(79) Weng, L. T.; Bertrand, P.; Lalande, G.; Guay, D.; Dodelet, J. P. *Appl. Surf. Sci.* **1995**, *84*, 9.

(80) Dignardbailey, L.; Trudeau, M. L.; Joly, A.; Schulz, R.; Lalande, G.; Guay, D.; Dodelet, J. P. *J. Mater. Res.* **1994**, *9*, 3203.

(81) Bouwkamp-Wijnoltz, A. L.; Visscher, W.; van Veen, J. A. R.; Boellaard, E.; van der Kraan, A. M.; Tang, S. C. *J. Phys. Chem. B* **2002**, *106*, 12993.

(82) Rajagopalachary, S.; Verkhoturov, S. V.; Schweikert, E. A. *Anal. Chem.* **2009**, *81*, 1089.

(83) Rajagopalachary, S.; Verkhoturov, S. V.; Schweikert, E. A. *Surf. Interface Anal.* **2011**, *43*, 547.

(84) Pinnick, V.; Verkhoturov, S. V.; Kaledin, L.; Schweikert, E. A. *Surf. Interface Ana.l* **2011**, *43*, 551.

(85) McBride, J. R.; Dukes, A. D.; Schreuder, M. A.; Rosenthal, S. J. *Chem. Phys. Lett.* **2010**, *498*, 1.

(86) Harrell, S. M.; McBride, J. R.; Rosenthal, S. J. *Chem. Mater.* **2013**, *25*, 1199.

(87) Kim, B. H.; Lee, N.; Kim, H.; An, K.; Park, Y. I.; Choi, Y.; Shin, K.; Lee, Y.; Kwon, S. G.; Na, H. B.; Park, J. G.; Ahn, T. Y.; Kim, Y. W.; Moon, W. K.; Choi, S. H.; Hyeon, T. *J. Am. Chem. Soc.* **2011**, *133*, 12624.

(88) Grainger, D. W.; Castner, D. G. *Adv. Mater.* **2008**, *20*, 867.

(89) Kim, S. T.; Saha, K.; Kim, C.; Rotello, V. M. *Acc. Chem. Res.* **2013**, *46*, 681.

(90) Zhou, J.; Ralston, J.; Sedev, R.; Beattie, D. A. *J. Coll. Interface Sci.* **2009**, *331*, 251.

(91) Wiesner, M. R.; Lowry, G. V.; Casman, E.; Bertsch, P. M.; Matson, C. W.; Di Giulio, R. T.; Liu, J.; Hochella, M. F. *ACS Nano* **2011**, *5*, 8466.

(92) Pennycook, T. J.; McBride, J. R.; Rosenthal, S. J.; Pennycook, S. J.; Pantelides, S. T. *Nano Lett.* **2012**, *12*, 3038.

(93) Yamaguchi, Y.; Gspann, J. *Phys. Rev. B* **2002**, *66*.

(94) Egerton, R. F.; Li, P.; Malac, M. *Micron.* **2004**, *35*, 399.

(95) Gnaser, H. *Nucl. Instrum. Meth. B* **1999**, *149*, 38.

(96) Della-Negra, S.; Depauw, J.; Joret, H.; Le Beyec, Y.; Schweikert, E. A. *Phys. Rev. Lett.* **1988**, *60*, 948.

(97) Della-Negra, S.; Depauw, J.; Guillermier, C.; Schweikert, E. A. *Surf. Interface Anal.* **2011**, *43*, 62.

(98) Schlatholter, T.; Newman, M. W.; Niedermayr, T. R.; Machicoane, G. A.; McDonald, J. W.; Schenkel, T.; Hoekstra, R.; Hamza, A. V. *Eur. Phys. J. D* **2000**, *12*, 323.

(99) Kim, Y. P.; Oh, E.; Hong, M. Y.; Lee, D.; Han, M. K.; Shon, H. K.; Moon, D. W.; Kim, H. S.; Lee, T. G. *Anal. Chem.* **2006**, *78*, 1913.

(100) Kim, Y. P.; Lee, T. G. *Anal.Chem.* **2012**, *84*, 4784.

(101) Georgakilas, V.; Otyepka, M.; Bourlinos, A. B.; Chandra, V.; Kim, N.; Kemp, K. C.; Hobza, P.; Zboril, R.; Kim, K. S. *Chem. Rev.* **2012**, *112*, 6156.

(102) Diaz, A.; Mosby, B. M.; Bakhmutov, V. I.; Marti, A. A.; Batteas, J. D.; Clearfield, A. *Chem. Mate.r* **2013**, *25*, 723.